The Astrophysical Journal, 951:33 (33pp), 2023 July 1 https://doi.org/10.3847/1538-4357/acc94f

A 7 Day Multiwavelength Flare Campaign on AU Mic. I. High-time-resolution Light Curves and the Thermal Empirical Neupert Effect

Isaiah I. Tristan[1,2,3], Yuta Notsu[1,2,3,4], Adam F. Kowalski[1,2,3], Alexander Brown[5], John P. Wisniewski[6], Rachel A. Osten[7], Eliot H. Vrijmoet[8,9], Graeme L. White[10], Brad D. Carter[10], Carol A. Grady[11], Todd J. Henry[9], Rodrigo H. Hinojosa[12], Jamie R. Lomax[13], James E. Neff[14], Leonardo A. Paredes[9,15], and Jack Soutter[10]
[1] Department of Astrophysical and Planetary Sciences, University of Colorado Boulder, 2000 Colorado Avenue, CO 80305, USA; Isaiah.Tristan@colorado.edu
[2] Laboratory for Atmospheric and Space Physics, University of Colorado Boulder, 3665 Discovery Drive, Boulder, CO 80303, USA
[3] National Solar Observatory, University of Colorado Boulder, 3665 Discovery Drive, Boulder, CO 80303, USA
[4] Department of Earth and Planetary Sciences, Tokyo Institute of Technology, 2-12-1 Ookayama, Meguro-ku, Tokyo 152-8551, Japan
[5] Center for Astrophysics and Space Astronomy, University of Colorado Boulder, 389 UCB, CO 80309, USA
[6] Department of Physics and Astronomy, George Mason University, 4400 University Drive, MS 3F3, Fairfax, VA 22030, USA
[7] Space Telescope Science Institute, Baltimore, MD 21218, USA
[8] Department of Physics and Astronomy, Georgia State University, Atlanta, GA 30303, USA
[9] RECONS Institute, Chambersburg, PA 17201, USA
[10] Computational Engineering and Science Research Centre, University of Southern Queensland, Toowoomba 4350, Australia
[11] Eureka Scientific, 2452 Delmer, Suite 100, Oakland, CA 94602-3017, USA
[12] Cerro Tololo Inter-American Observatory, CTIO/AURA Inc., La Serena, Chile
[13] Department of Physics, United States Naval Academy, 572c Holloway RD, Annapolis, MD 21402, USA
[14] Division of Astronomical Sciences, National Science Foundation, Alexandria, VA 22314, USA
[15] Department of Physics and Astronomy, Georgia State University, Atlanta, GA 30302, USA
Received 2022 November 28; revised 2023 March 28; accepted 2023 March 29; published 2023 June 29

Abstract

We present light curves and flares from a 7 day, multiwavelength observational campaign of AU Mic, a young and active dM1e star with exoplanets and a debris disk. We report on 73 unique flares between the X-ray to optical data. We use high-time-resolution near-UV (NUV) photometry and soft X-ray (SXR) data from the X-ray Multi-Mirror Mission to study the empirical Neupert effect, which correlates the gradual and impulsive phase flaring emissions. We find that 65% (30 of 46) flares do not follow the Neupert effect, which is 3 times more excursions than seen in solar flares, and propose a four-part Neupert effect classification (Neupert, quasi-Neupert, non-Neupert types I and II) to explain the multiwavelength responses. While the SXR emission generally lags behind the NUV as expected from the chromospheric evaporation flare models, the Neupert effect is more prevalent in larger, more impulsive flares. Preliminary flaring rate analysis with X-ray and *U*-band data suggests that previously estimated energy ratios hold for a collection of flares observed over the same time period, but not necessarily for an individual, multiwavelength flare. These results imply that one model cannot explain all stellar flares and care should be taken when extrapolating between wavelength regimes. Future work will expand wavelength coverage using radio data to constrain the nonthermal empirical and theoretical Neupert effects to better refine models and bridge the gap between stellar and solar flare physics.

Unified Astronomy Thesaurus concepts: Red dwarf flare stars (1367); Stellar activity (1580); Stellar flares (1603); Optical flares (1166); Stellar x-ray flares (1637); Planet hosting stars (1242)

Supporting material: machine-readable table

1. Introduction

M dwarfs will be high-priority targets in the search for habitable exoplanet systems, as they are the most common stars in the solar neighborhood (Henry et al. 2006) and their higher planet-to-star contrast relative to more luminous stars allows for easier transit detection. Stellar activity like flares and coronal mass ejections may affect the habitability of exoplanets through increased high-energy photon and particle fluxes (Linsky 2019; Airapetian et al. 2020). As examples, stellar ultraviolet (UV) spectra help ascertain the effects on exoplanet atmospheric chemistry and escape rates (see Section E-Q2d of Loyd et al. 2018; Decadal 2020), and X-rays can influence protoplanetary disk chemistry (Osten et al. 2013; Osten & Wolk 2015; Notsu et al. 2021) and lead to enhanced near-UV (NUV) radiation rates at the ground level through fluorescence (Smith et al. 2004).

The response at optical wavelengths has historically been the best-observed phenomenon in stellar flares, thanks to many decades of ground-based monitoring in the *UBVR* bandpasses (Lacy et al. 1976; Pettersen et al. 1984; Hilton 2011) and recent long-baseline, high-precision ancillary white-light data provided by Kepler, K2, and the Transiting Exoplanet Survey Satellite (TESS; Hawley et al. 2014; Davenport 2016; Notsu et al. 2019; Howard 2022; Mendoza et al. 2022). Large observational campaigns spanning the X-ray, UV, optical, and radio have unfortunately been few and far between (Osten et al. 2005, 2006). Empirical multiwavelength relationships for the full range of flare amplitudes, energies, and light-curve morphologies (e.g., gradual versus impulsive) are severely lacking, and simple slab model extrapolations (i.e., modeling flaring emission from a plasma region with static properties) from the optical are largely unjustified (Kowalski et al. 2019).

It is widely accepted that similar physical processes of magnetic reconnection, particle acceleration, and plasma heating operate in both solar and stellar flares (Shibata & Magara 2011; Shibata & Takasao 2016). The multiwavelength relationship that justifies these similarities is known as the Neupert effect, which was first observed in solar flares as the correspondence between the derivative of thermal, soft X-rays (SXRs; $E \lesssim 15$ keV) and the instantaneous nonthermal gyrosynchrotron centimeter-wave flux (Neupert 1968). The empirical Neupert effect (ENE) has been widely studied in solar flares using the cumulative time integral of the impulsive phase, power-law hard X-rays (HXRs; $E \gtrsim 25$ keV) and the SXRs emitted from plasma at $T \gtrsim 15$ MK (Dennis & Zarro 1993; McTiernan et al. 1999; Veronig et al. 2002, 2005; Qiu et al. 2013; Namekata et al. 2017), and certain timings between the two responses. The Neupert effect has also been studied in several stellar flares in M dwarfs and RS CVns (Hawley et al. 1995; Güdel et al. 1996, 2002; Osten & Wolk 2015; Stelzer et al. 2022). Note that while gyrosynchrotron emission is best detected through radio observations (see Osten et al. 2005; MacGregor et al. 2018), the broadband optical or NUV continuum response is often used as a proxy in stellar studies, as radio or HXR responses can be too faint to easily detect (Osten et al. 2007). For reference, the thermal ENE uses a proxy, while the nonthermal ENE uses radio/microwave data, and they both measure the same quantities.

Likewise, the theoretical Neupert effect (TNE) explains the multiwavelength temporal behaviors in terms of chromospheric evaporation and condensation in response to impulsive nonthermal electron beam heating (Antonucci et al. 1982, 1984). The pioneering radiative-hydrodynamic models of Allred et al. (2005; built upon Livshits et al. 1981; McClymont & Canfield 1984; Fisher et al. 1985a, 1985b; Cargill et al. 1995; Lee et al. 1995; Abbett & Hawley 1999) established this standard flare paradigm. After nonthermal particles gyrate in the magnetic fields, producing gyrosynchrotron radiation, they precipitate into the chromosphere, producing HXRs. The beam heating is accompanied by increased chromospheric radiation in the optical and NUV just below the upper chromospheric layers that explosively heat to tens of million kelvins, ablate into the corona, and eventually fill the magnetic loops and shine luminously in SXRs. These ideas have been extended to stellar flares using modern radiative-hydrodynamic simulations with larger beam fluxes than inferred on the Sun (Allred et al. 2006; Kowalski et al. 2015).

About 20% of solar flares (Dennis & Zarro 1993) and numerous stellar flare observations clearly do not exhibit the Neupert effect, or the ENE only approximately explains the wavelength-dependent time delays. Notable examples are the late impulsive peak in HXRs during a solar flare (Warmuth et al. 2009) and a giant radio flare from EV Lac with a very impulsive *U*-band light curve but no temporally consistent response in the SXRs (Osten et al. 2005). In other event comparisons, the energy partition in the impulsive and gradual phase radiation has been found to vary by nearly an order of magnitude (Osten & Wolk 2015; Osten et al. 2016). X-ray and UV flux correlations have been found in stellar flares, with power-law relationships between their energies with exponents between 1 and 2 (Mitra-Kraev et al. 2005). Veronig et al. (2002) suggests that flares with relatively more X-ray luminosity are powered by direct heating of the corona with relatively weaker nonthermal particle heating present; this has also been discussed in relation to energy budget comparisons in solar flares (Warmuth & Mann 2016a, 2016b). At the high-energy regime, however, large stellar flares are shown to be X-ray-weak compared to their solar counterparts (Güdel et al. 1996), supporting higher electron beam flux models. Veronig et al. (2005) discusses several simplifications in standard models, including assumptions of a static beam low cutoff energy, loop geometry, and heterogeneity of the flare source, all of which may lead to variations in the TNE when critically analyzed at high time resolution. There are also alternative heating sources in the flaring environment, like thermal conduction, where heat is transmitted through the loop after magnetic reconnection (see Yokoyama & Shibata 2001 and references within), which could affect the observed ENE and TNE responses.

To better understand the energy partition and multiwavelength timing in stellar flares, we have executed a large observational campaign on a young flare star, AU Mic, over 7 days with a combination of ground- and space-based observatories. These observations were designed to challenge our understanding of chromospheric evaporation and condensation in novel ways by constraining the empirical differences in the impulsive and gradual phase radiation from flare to flare. Known for its large average flare energies, AU Mic is an ideal target since white light is not produced in any great amount by direct heating of the corona and subsequent thermal conductive fluxes into the upper chromosphere (Kowalski et al. 2017; Namekata et al. 2020). Thus, this data set is intended to push our knowledge of the ENE and TNE into regimes that reveal new physical processes in stellar atmospheric heating by nonthermal particles, which in turn would allow far more realistic inputs into models of atmospheric photochemistry around M dwarfs.

This paper is the first in a series. Here, we present the data reduction, light curves, and analysis of the ENE from the flare campaign on AU Mic in 2018 October. This paper is organized as follows. In Section 2, we describe our target, the observations of AU Mic, and the data reduction and absolute flux calibration. In Section 3, we present light curves and showcase the flares identified. In Section, 4, we outline the methods used and share results. In Section 5, we discuss our findings in the context of the ENE and provide insight into necessary future work. In Section 6, we summarize and conclude this work.

2. The 7 Day AU Mic Flare-monitoring Campaign

2.1. The Target: AU Mic

The target of our flare-monitoring observations is the M1 star AU Mic, a nearby pre-main-sequence star located at a distance of 9.72 pc (Gaia Collaboration et al. 2016, 2018). It is part of the β Pictoris moving group, with an age of 23 ± 3 Myr (Mamajek & Bell 2014). In a Hertzsprung–Russell diagram constructed from Gaia Data Release 2 (DR2) data (Gaia Collaboration et al. 2016, 2018), AU Mic is above the main sequence and is consistent with a PARSEC (Bressan et al. 2012) color–magnitude 23 Myr isochrone, suggesting that it is still contracting.[16] Selected stellar properties of AU Mic are summarized in Table 1.

[16] Assuming a typical radius for an M1 main-sequence star of $0.49R_{\rm Sun}$ (Reid et al. 2004), we calculate the radius of AU Mic to be $\sim 0.7R_{\rm Sun}$ from the Gaia DR2 *G*-band magnitude. The AAS abstract from White et al. (2019) reports an interferometric radius of $0.75R_{\rm Sun}$, which Plavchan et al. (2020) corroborates.

Table 1
Stellar Properties of AU Mic

Spectral Type	R (1, 2) ($R_\odot$)	M (2) ($M_\odot$)	Dist. (3) (pc)	Age (4) (Myr)	Rot. Period (2) (day)	Projected Radial Vel. (1, 2) (km s^{-1})
dM1e	0.75 ± 0.03	0.5 ± 0.03	9.72	23 ± 3	4.863 ± 0.01	8.7 ± 0.2

Note. (1) White et al. (2019), (2) Plavchan et al. (2020), (3) Gaia Collaboration et al. (2018), (4) Mamajek & Bell (2014).

Table 2
Observation Log: Summary

Instrument	Band (Å)	Start Date	End Date	Monitoring Time (hr)	Cadence (s)	Exposure (s)
XMM-Newton/EPIC-pn/X-ray	1.03-62	2018-10-10	2018-10-17	130.04	10	10
Swift/XRT/X-ray	1.24-62	2018-10-12	2018-10-14	4.35	5	5
XMM-Newton/RGS/X-ray	5–35	2018-10-10	2018-10-17	130.83	∼35	∼35
Swift/UVOT/*W2*	1600–3480	2018-10-12	2018-10-14	4.35	5	5
XMM-Newton/OM/*UVW2*	1790–2890	2018-10-10	2018-10-17	108.74	10	10
LCOGT/1 m/*U* band	3030–4170	2018-10-10	2018-10-29	74.15	46	4
LCOGT/0.4 m/*V* band	4780–6350	2018-10-10	2018-10-29	79.84	25	2
SMARTS/2KCCD/*V* band	4780–6350	2018-10-10	2018-10-17	26.69	47	15
SMARTS/CHIRON/Hα	4500–8900	2018-10-10	2018-10-25	61.21	65	60

Note. Summary of all observations used in this analysis. A detailed log of all observation windows is given in Appendix D. Note that while CHIRON observes over a broad wavelength range, the analysis in this paper is focused on the Hα line, 6562.8 Å.

AU Mic has been a frequent target of Hubble Space Telescope (HST) observations due to its IR excess ($L_{\rm IR}/L_\star = 0.44$; Schneider et al. 2014), lack of mid-IR thermal excess (Chen et al. 2005), and resolved edge-on debris disk with outward-moving features (Kalas et al. 2004; Krist et al. 2005; Boccaletti et al. 2015; Wisniewski et al. 2019; Grady et al. 2020). Flares from AU Mic may promote stellar wind pressure, contributing to the extended debris disk (Augereau & Beust 2006). AU Mic also has a confirmed planetary system consisting of one Neptune-sized planet, which has an orbital period of 8.46 days and is situated at a distance of 0.07 au (Plavchan et al. 2020), and one slightly smaller planet with a period of 18.86 days (Martioli et al. 2021; Gilbert et al. 2022). The space weather conditions surrounding AU Mic may make the possibility of planetary atmospheres unlikely, however (Alvarado-Gómez et al. 2022; Cohen et al. 2022; Klein et al. 2022).

AU Mic is a member of a relatively rare subclass of early-type M stars (West et al. 2008) that are magnetically active with Hα in emission and a variable *V*-band magnitude (Torres & Ferraz Mello 1973; Rodono et al. 1986; Hebb et al. 2007) outside of obvious flare events. It is the most X-ray-luminous star within 10 pc with a quiescent X-ray (0.05–3.5 keV) luminosity of $10^{29.7}$ erg s^{-1} (Pallavicini et al. 1990; Leto et al. 2000). Recent studies have also shown that AU Mic's surface-averaged magnetic field is much larger than the Sun's, and its dipole fields exhibit asymmetric components (Kochukhov & Reiners 2020) that may be misaligned with the rotation axis (Wisniewski et al. 2019), thus having an influence on the disk morphology (Wisniewski et al. 2019).

AU Mic has been a source of energetic flares in the X-ray, UV, optical, and radio wavelength regimes (Robinson et al. 1993; Cully et al. 1994; Robinson et al. 2001; Redfield et al. 2002; Mitra-Kraev et al. 2005; Hebb et al. 2007; MacGregor et al. 2020; Feinstein et al. 2022). In the optical and NUV, which directly probe the enigmatic white-light continuum radiation, the flares from early-type (M0–M1) M-dwarf stars have rarely been studied with any time resolution or complementary multiwavelength information, unlike for flares from mid- and late-type M dwarfs (e.g., Hawley et al. 1995; Osten et al. 2005; Fuhrmeister et al. 2008, 2011; Kowalski et al. 2019; MacGregor et al. 2021). This is due to their lower contrast against the photospheric background (e.g., Kowalski et al. 2009), allowing only the largest events to rise above the typical noise floor. Since the largest events are also the rarest (Lacy et al. 1976; Gilbert et al. 2022), long monitoring times are required to guarantee a sample of flares that can be characterized in detail. AU Mic is one of the best early-type M-dwarf targets for such a next-generation flare campaign: it is a single star with a known age; it is the stellar source at the heart of an intriguing exoplanetary and debris disk system; and its dynamo mechanism falls in the partially convective regime, facilitating interesting comparisons to high-energy solar flares.

2.2. Observations and Initial Data Reduction

We observed AU Mic over 7 days spanning 2018 October 10–2018 October 17 with the X-ray Multi-Mirror Mission (XMM-Newton; Jansen et al. 2001), the Jansky Very Large Array (JVLA), the Neil Gehrels Swift Observatory (Swift), the Las Cumbres Observatory Global Telescope network (LCOGT; Brown et al. 2013), the Astrophysical Research Consortiums 3.5 m telescope at the Apache Point Observatory (APO), the Australia Telescope Compact Array (ATCA), and the Small and Moderate Aperture Research Telescope System (SMARTS; Subasavage et al. 2010) 0.9 and 1.5 m telescopes at the Cerro Tololo Inter-American Observatory (CTIO). The observations used in this paper are summarized in Table 2. JVLA, APO, and ATCA data will be reduced and analyzed in future studies. Together, these form the most wavelength-comprehensive, high-time-resolution simultaneous observations of AU Mic to date.

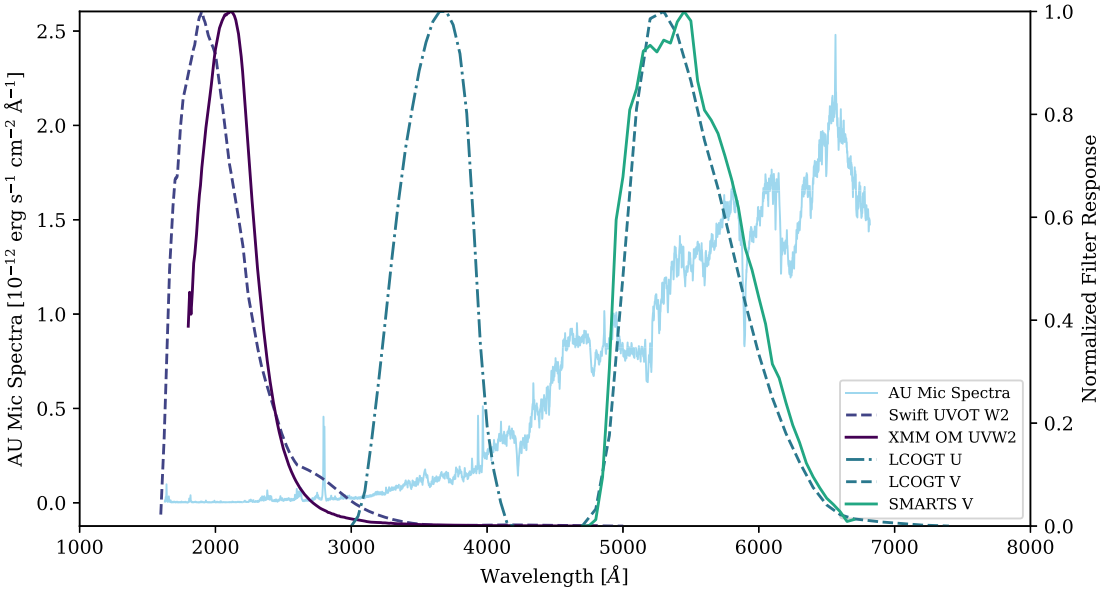

Figure 1. Effective area or filter transmission curves (photon weighting) for the broadband filters used in this study plotted against the quiescent HST/FOS spectrum of AU Mic. All filter responses are normalized from 0 to 1.

2.2.1. *XMM-Newton European Photon Imaging Camera X-Ray Photometry*

The XMM-Newton observations were conducted in four visits (Obs-IDs: 0822740301, 0822740401, 0822740501, and 0822740601), which spanned 2018 October 10 13:13:59.760 to 2018 October 12 01:42:19.177 UTC (131.29 ks), 2018 October 12 13:06:33.808 to 2018 October 14 01:36:22.232 UTC (131.40 ks), 2018 October 14 12:21:18.787 to 2018 October 16 00:04:00.273 UTC (71.75 ks), and 2018 October 16 23:39:21.362 to 2018 October 17 18:17:33.004 UTC (67.10 ks). X-ray photometry was obtained over a bandpass of $E \approx 0.2$–12 keV using the European Photon Imaging Camera (EPIC-pn; Strüder et al. 2001) medium filter and 10 s time binning. During the least active times (00:00:00.0–07:12:00.0 UTC, 2018 October 11), the X-ray flux averaged 15.3 ± 1.6 counts per second (cps). Data from the MOS 1 and 2 detectors were simultaneously captured and will be used for future analysis.

2.2.2. *Swift XRT X-Ray Photometry*

Swift provided complementary X-ray and NUV coverage during gaps between the XMM-Newton visits. Swift XRT X-ray ($E \approx 0.2$–10 keV; Burrows et al. 2005) photon-counting data were taken in two large windows, from 03:26:20.0 to 10:04:50.0 UTC (8.28 ks) on 2018 October 12 and 03:03:16.0 to 09:53:51.0 UTC (7.38 ks) on 2018 October 14. We used AstroImageJ (Collins et al. 2017) to determine a circular aperture and background annulus. On 2018 October 12, an aperture of 37.″71 and annulus between 66.″00 and 99.″00 were used (reported pixel:arcsec conversion of 6.89:16.24), while on 2018 October 14 an aperture of 32.″98 and annulus between 58.″88 and 89.″50 were used (reported pixel:arcsec of 5.29:12.46). A light curve was then extracted using XSELECT[17] (Nasa High Energy Astrophysics Science Archive Research Center, Heasarc 2014) and binned into 5 s intervals. No obvious flares were found in these data, and detailed analysis showed that no time intervals exceeded 2σ above the daily, average quiescent value.

2.2.3. *XMM-Newton Reflection Grating Spectrometer X-Ray Spectroscopy*

X-ray spectra were obtained using the Reflection Grating Spectrometer (RGS), which consists of two identical spectrographs, RGS1 and RGS2, in order to increase the signal-to-noise ratios. Data were collected over the energy range 0.33–2.5 keV (spectral resolving power ($E/\Delta E$) between 150 and 800) in its "Spectroscopy" mode with submode "HighEventRateWithSES" and observation mode "Pointed". Pipeline Processing System (PPS; version 17.56_20190403_1200) data are supplied, which use standard Science Analysis System (SAS; version xmmsas_20190401_1820-18.0.0) tasks to produce data products like light curves and average spectra (Gabriel et al. 2004). We use the PPS light curves for the four XMM-Newton observations, which have time bins of 30, 32, 36, and 27 s, per observation window.

2.2.4. *Swift Ultraviolet Optical Telescope* W2 *Photometry*

The Ultraviolet Optical Telescope (UVOT; Roming et al. 2005) was employed on Swift using the *W2* filter. Compared to the XMM-Newton *UVW2* filter (see Section 2.2.5), the Swift *W2* is wider but much bluer, with an effective wavelength that is shorter by about 200 Å (see Figure 1). AstroImageJ was also used to select the source aperture and background annulus. On the first day, the aperture radius was 5.″52 and the annulus radii were 11.″54 and 35.″13 (reported pixel:arcsec of 8.07:4.05). On the second day, 6.″02 and 10.″53–35.″11 (reported pixel:arcsec of 6.36:3.19) were used, respectively. Light curves with time bins of 5, 10, and 30 s were then extracted using XSELECT. Again, no obvious flares were found in the Swift data, and no data points exceeded 2σ above the mean. Two observation windows start with a decreasing rate trend, but there are no corresponding enhancements in the Swift XRT X-rays to suggest that these correspond to the tail ends of flares.

[17] http://heasarc.gsfc.nasa.gov/ftools

2.2.5. *XMM-Newton Optical Monitor* UVW2 *Photometry*

We obtained *UVW2* photometry with the XMM-Newton Optical Monitor (OM) in FAST mode using an onboard binning of 10 s. Count rates from the PPS TIMESR files were extracted and corrected from Terrestrial Time (TT) to UTC at the middle of the exposure. The *UVW2* filter is the bluest of the OM filters and was chosen to build upon the findings from a superflare in Osten et al. (2016) that shows unexpected results from model comparisons to the *V* band (see their Figure 8). A more detailed discussion will be presented in Paper II of this study (A. F. Kowalski et al. 2023, in preparation).

The *UVW2* band has an effective wavelength of 2120 Å (for white dwarf stars) and is very broad, with a low-level tail that extends to redder wavelengths at $\lambda \approx 3000$–7000 Å. This tail accounts for less than 1% of the total effective area (see Figure 1). In quiescence, the count rate of AU Mic is 1.8 cps, and ∼50% is expected to be due to this red-tail emission from wavelengths $\lambda > 4000$ Å. For hot stars, the contribution from $\lambda > 3000$ Å is on the order of 1% (Talavera 2011); this red emission is not a concerning source of systematic uncertainty in our analyses because flares are very blue. Robust model comparisons are readily achieved by synthesizing flux densities from the full wavelength coverage of the *UVW2* effective area curve.

Large coincidence losses occur when the photon arrival rate is greater than the frame rate of the OM (Fordham et al. 2000; Page et al. 2013). Coincidence loss corrections are applied to data with count rates less than 0.97 counts per frametime and are accurate to better than 2%. The largest count rate that occurs in flaring intervals is 105 counts s^{-1}, which corresponds to 0.53 counts per frametime of 5 ms.[18] FAST mode requires that a very small ($10'' \times 10''$) window around the star is employed for onboard windowing. The pointing variation of XMM-Newton among observations caused the star to fall on the edge of this window during the third observation, so there is no *UVW2* photometry from 2018 October 14 18:48:06.449 to 2018 October 15 10:35:09.418 UTC.

2.2.6. *Las Cumbres Observatory Global Telescope* U- *and* V-*band Photometry*

AU Mic was observed in the *U* and *V* bands by the LCOGT network between 2018 October 13 and 2018 October 29, thus extending the observational campaign past the end of the XMM-Newton observations. For both bands (see Figure 1), we used the reduced images from the automatic `BANZAI` pipeline, which masks bad pixels, applies an astrometric solution, and performs bias and dark subtraction. Light curves were extracted using the supplied Kron apertures, which were verified by comparing to standard IRAF procedures and AstroImageJ. Among the aperture photometry methods, the Kron aperture was found to exhibit the best signal-to-noise ratio during flares and quiescence.

Bessel *U*-band observations were obtained with the 1 m telescopes, with an exposure time of 4 s and a cadence of 46 s. Bessel *V*-band observations were obtained with the 0.4 m telescopes within the LCOGT network, with an exposure time and cadence of 2 s and 25 s, respectively. In the *U* band, the A9V star HD 197673 was used as a comparison star for the relative photometry. In the *V* band, both HD 197673 and an inactive field star, Gaia DR2 6793990654220996352, were used for the relative photometry.

2.2.7. *SMARTS* V-*band Photometry*

AU Mic was observed by the 0.9 m telescope at the Cerro Tololo Inter-American Observatory, operated by the Small and Moderate Aperture Telescope Research System (SMARTS) Consortium, between 2018 October 10 and 2018 October 17. SMARTS is operated by the REsearch Consortium On Nearby Stars, which aims to discover and characterize stars in the solar neighborhood (Henry et al. 2018; Vrijmoet et al. 2020). The exposure time was 15 s, and a cadence of 47 s was achieved using the V Tek #2 filter (CTIO/CTIO.5438-1026 on the SVO Filter Database) for these observations. The LCOGT *V* bandpass is slightly bluer than the CTIO/SMARTS 0.9 m *V* band, which is closer to the standard Bessel *V* filter transmission (Bessell & Murphy 2012). Aperture photometry of AU Mic and the background stars Gaia DR2 6794048928337372800 and Gaia DR2 6794044358492150912 was extracted using AstroImageJ. A large, 20 pixel aperture is chosen to collect all the flux from the defocused point-spread functions of AU Mic and a sum of nearby comparison stars. Defocusing results in ≈3 million counts per exposure from AU Mic and a standard deviation of 5 mmag during quiescent times. Notably, the *V*-band photometry from the CTIO/SMARTS 0.9 m is much higher precision in quiescence than the LCOGT *V* band.

2.2.8. *SMARTS CTIO High ResolutiON Spectrograph Optical Spectra*

We obtained optical spectra from the cross-dispersed, fiber-fed echelle CTIO High ResolutiON (CHIRON) spectrograph (Tokovinin et al. 2013) at the CTIO/SMARTS 1.5 m with 60 s integration times. The usable wavelength range and mean spectral resolving power of our CHIRON data are $\lambda = 4500$–8900 Å and $R = \lambda/\Delta\lambda \approx 25{,}000$, respectively. The data were wavelength calibrated using a ThAr lamp, resulting in a resolving power of $R \sim 28{,}000$ around Hα. In particular, we look at the fluctuations of the equivalent width of the Hα line during flaring events. These observations also extend past the 7 day duration of the XMM-Newton observations and will be analyzed in detail in Y. Notsu et al. 2023, in preparation.

2.3. *Absolute Flux and Energy Calibration of* UVW2, U, V, *and X-Ray Photometry*

Absolute flux calibration of the photometry is critical for addressing several of the goals of our observational campaign. In this section, we summarize our methods, which are described in detail in Appendix A. Note that all of the broadband filters used are shown against the AU Mic spectrum from the HST/Faint Object Spectrograph (FOS/RD gratings G190H/2300 Å, G270H/2650 Å, G400H/3600 Å, and G570H/4600 Å observed on 1991 September 11, as used in Augereau & Beust 2006, available on the MAST archive[19]) in Figure 1.

We calculated energies (fluences) using the equivalent duration (Gershberg 1972), defined as

$$\mathrm{ED} = \int \frac{I - I_q}{I_q}\, dt, \tag{1}$$

[18] See https://xmm-tools.cosmos.esa.int/external/xmm_user_support/documentation/uhb/omlimits.html; we confirmed with OM calibration scientist R. Riestra (2019, private communication) that the largest count rate is below the extreme coincidence-loss regime and constitute a clean observation.

[19] doi:10.17909/6pe3-yp69.

Table 3
Adopted and Synthetic Broadband Quiescent Fluxes and Luminosities of AU Mic

Bandpass T	$\langle f_{q,\lambda}\rangle_T$ Zero-point Method† (10^{-14} erg cm^{-2} s^{-1} Å^{-1})	$\langle f_{q,\lambda}\rangle_T$ HST Spectrum (10^{-14}) erg cm^{-2} s^{-1} Å^{-1}	$\Delta\lambda_{\rm FWHM}$ (Å)	$\lambda_{\rm mean}$ (Å)	$L_{q,T}$ (10^{28} erg s^{-1})
UVW2 (XMM OM)	1.03	1.14–1.18	475	2150	5.5
Bessel *U* (LCOGT)	12.2–14.0	13.5–14.1	700	3610	100
Bessel *V* (CTIO/SMARTS 0.9m)	110 – 133	122	850	5510	1200

Notes. Bandpass zero points are obtained from Willmer (2018) and the SAS. The values of $\Delta\lambda_{\rm FWHM}$ are adopted from Moffett (1974) to compare more directly to the study of Lacy et al. (1976) with similar *U* and *V* bandpasses. † Adopted quiescent fluxes of AU Mic; see text and Appendix A.

where I is the count rate (calibrated or relative) and q indicates quiescence. The ED is then multiplied by the bandpass (T) quiescent luminosity ($L_{q,T}$) to find the bandpass-integrated flare energy, $E_T = {\rm ED} \times L_{q,T}$.

Flux-calibrated light curves are thus obtained by knowledge of the quiescent fluxes. For known and well-characterized bandpasses, these can be determined using zero points (as summarized in Willmer 2018) and published apparent magnitudes at low levels of flare activity (*U*, *V*) or count-rate conversions (*UVW2*). We compare the zero-point method to numerical integration of the observed spectrum of AU Mic from HST/FOS over the bandpass, according to the equation

$$L_{q,T} = \langle f_{q,\lambda}\rangle_T \, \Delta\lambda_{\rm FWHM} \, 4\pi d^2 = \frac{\int T(\lambda) f_{q,\lambda}(\lambda)\, \lambda \, d\lambda}{\int T(\lambda)\, \lambda \, d\lambda} \Delta\lambda_{\rm FWHM} \, 4\pi d^2, \quad (2)$$

where $\langle f_{q,\lambda}\rangle_T$ is the system-weighted flux (Sirianni et al. 2005), $T(\lambda)$ is the total system response or effective area including the bandpass and atmosphere (if applicable), $f_{q,\lambda}(\lambda)$ is the quiescent HST/FOS spectrum at Earth in units of erg cm^{-2} s^{-1} Å^{-1}, $\Delta\lambda_{\rm FWHM}$ is the FWHM of the bandpass, and d is the distance to AU Mic. For the *U*, *V*, and *UVW2* bands, the systematic uncertainties of the flux calibration of the quiescent fluxes are ≈10%. The adopted quiescent fluxes, $\langle f_{q,\lambda}\rangle_T$, are thus $1.0 \pm 0.1 \times 10^{-14}$ erg cm^{-2} s^{-1} Å^{-1} (*UVW2*), $1.3 \pm 0.1 \times 10^{-13}$ erg cm^{-2} s^{-1} Å^{-1} (*U*), and $1.2 \pm 0.1 \times 10^{-12}$ erg cm^{-2} s^{-1} Å^{-1} (*V*), also summarized in Table 3.

Flux calibration for Swift data is not essential, because the lack of any flares only adds monitoring time for better statistics on the flare rates (as in Section 4.2). Note that between the XMM-Newton and Swift instruments, the EPIC-pn X-ray sensitivity is higher than the XRT,[20] while the UVOT *UVW2* sensitivity is higher than that of the OM.[21]

The energies in the EPIC-pn bandpass were calculated by converting the data from cps to erg cm^{-2} s^{-1} using the online WebPIMMS tool[22] (Mukai 1993), integrating over the duration of the flare, and multiplying by $4\pi d^2$. Specifically, the data were converted from XMM/PN Med Count Rate 5' region to FLUX, with a default input energy range and 0.4–10 keV energy output range, a $N_{\rm H}$ of 2.29×10^{18} cm^{-2} (Wood et al. 2005), and temperatures ranging from 10^7–3×10^7 K ($k_BT = 0.86$–2.59 keV). The adopted quiescent X-ray bandpass flux is thus $2.6 \pm 0.3 \times 10^{-11}$ erg cm^{-2} s^{-1}. The peak X-ray fluxes of flares at a distance of AU Mic's habitable zone were calculated by normalizing to a distance of 0.3 au (based on Figure 7 of Kopparapu et al. 2013). X-ray time derivatives were also calculated using the 30 s bin EPIC-pn light curve. As noise was high at many times, we calculated X-ray derivative peak timings for flares by first convolving the light curve with a 15-point box function, taking the derivative of this new curve, and then applying a Scipy (Virtanen et al. 2020) `UnivariateSpline` fit to smooth sharp variations.

For comparison, we use the average X-ray luminosity from Mitra-Kraev et al. (2005) derived from fitting the EPIC-pn spectrum ranging from 0.2–12 keV with a three-temperature collisional ionization equilibrium model. Their modeling returned a value of $\bar{L}_x = 2.99 \times 10^{29}$ erg s^{-1}, and they estimate that this luminosity scales linearly with the XMM EPIC-pn X-ray light-curve count rate. The nonaveraged luminosity is then $L_x = \bar{L}_x/\bar{c}_x \times c_x$, where c_x is the count rate and $\bar{c}_x$ is the average count rate of the entire observation. This gives a quiescent luminosity of $2.7 \pm 0.3 \times 10^{29}$ erg s^{-1}. This is about 6% different than our estimated value from WebPIMMS and is within the uncertainty. Using this luminosity for XMM EPIC-pn X-ray Flare 23 (see Section 3), we calculate an energy 6.5% lower than the WebPIMMS estimation. We note that these energies are still preliminary as actual X-ray energies will need to account for changing temperatures throughout the flare, and future work will focus on the spectral analysis necessary for this.

3. The Flare Sample

All light curves produced from the observations in Section 2 are shown in Figure 2. Of interest, we determine the quiescent flux in various bandpasses to be 1.8 ± 0.5 cps ($4.9 \pm 1.4 \times 10^{-12}$ erg cm^{-2} s^{-1}; XMM OM *UVW2*), 15.3 ± 1.6 cps ($2.6 \pm 0.3 \times 10^{-11}$ erg cm^{-2} s^{-1}; XMM EPIC-pn X-ray), and $9.1 \pm 0.7 \times 10^{-11}$ erg cm^{-2} s^{-1} (LCOGT U). For context outside of this campaign, Iwakiri et al. (2020) measured a bright AU Mic X-ray flare flux of $2.9^{+0.7}_{-1.2} \times 10^{-9}$ erg cm^{-2} s^{-1} during 2020 April, and Kohara et al. (2021) measured an X-ray flare flux of $9.0^{+1.7}_{-1.6} \times 10^{-9}$ erg cm^{-2} s^{-1} during 2021 December using the MAXI/GSC nova alert system (2–20 keV band).

3.1. Flare Detection Method

We determined flare occurrence in each light curve as follows. The start and stop times of each flare were determined by eye from the light curves. The quiet times around each flare were are used to define a standard deviation and estimate the quiescent emission throughout the flare duration using a Scipy `UnivariateSpline` interpolation, which was often a linear fit. Note that nearby flares are removed before the fit is made, when necessary. Flare bounds are then refined based on an

[20] https://xmm-tools.cosmos.esa.int/external/xmm_user_support/documentation/uhb/xmmcomp.html
[21] https://swift.gsfc.nasa.gov/about_swift/uvot_desc.html
[22] https://heasarc.gsfc.nasa.gov/cgi-bin/Tools/w3pimms/w3pimms.pl

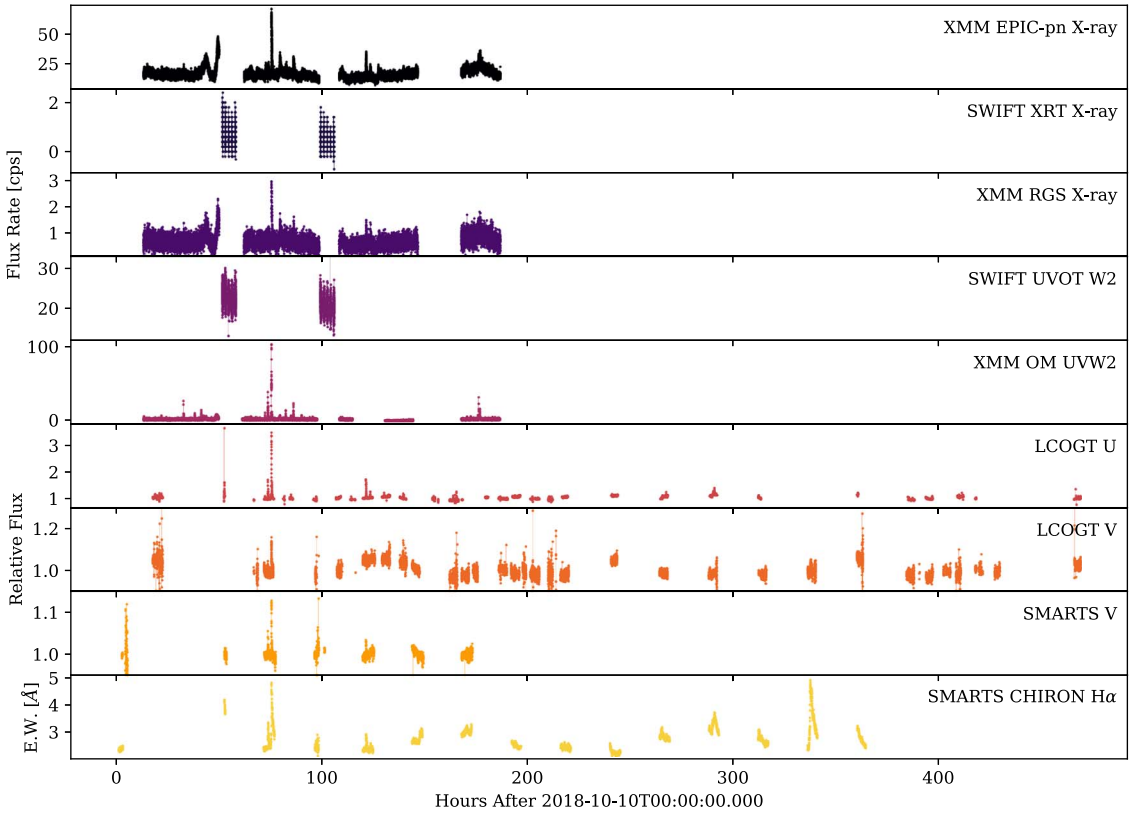

Figure 2. Light-curve summary of AU Mic during the flare campaign of 2018 October. Data from space-based observatories (X-ray and *UVW2*) are in units of counts per second, while ground-based data (*U* and *V*) are in relative flux units. Hα equivalent width (E.W.) data are in units of angstroms.

initial measure of when the flux is above 2σ of the quiescent. In total, we find 73 flares, with 34 XMM OM *UVW2*, 38 XMM EPIC-pn X-ray, 15 XMM RGS X-ray, 25 LCOGT *U*-band, two LCOGT *V*-band, four CTIO/SMARTS 0.9 m *V*-band, and 17 CHIRON Hα events. The properties of each flare are listed in Appendix B, and the flares are shown in Figures 3–9. Temporally coincident flares in different bandpasses are labeled with a common flare ID.

A few notes are warranted. Complex flare events with several short-duration subpeaks are identified as a single flare. Several of the lower-amplitude complex flares are also counted as one when, over short durations, the flux momentarily decreased below 2σ above the quiescent level (see XMM OM *UVW2* Flares 19 and 31 in Figure 4). Also, the large X-ray swell (Flare 11, which appears from 37 to 56 hr after the start of 2018 October 10 in Figure 3) is not clearly correlated with any other single simultaneous response, so it is given its own ID.

Flares with significant gaps in observation are left out of the sample. Exceptions were made for XMM OM *UVW2* Flares 23, 24, and 47 (see Figure 4) and LCOGT *U*-band Flares 72 and 73 (see Figure 6). Flare 24 is missing times early in the impulsive phase. It is unclear if there is an initial peak here, as the timing of the measured one lies within expectations. Flare 47 is missing times before the peak of an accompanying noisy, complex X-ray flare (see Figure 2 for comparison with the XMM EPIC-pn light curve). Thus, a linear extrapolation is added for each. For Flare 23, both linear and exponential decays were modeled for the missing times. The linear extrapolation is used for consistency, with the small difference factored into the error. There is no surrounding quiescent area for Flares 72 and 73, and the decay of Flare 73 is incomplete. To compensate for this, a quiescent level of 0.95 with a standard deviation of 0.02 is chosen based on the area's lowest point and the standard deviation of a quiet area at a similar relative flux level. These two flare IDs are the only ones out of chronological order, as the reduction is significantly different.

Any potential flares that could not pass through our pipeline (see Section 4.1) are considered too small for analysis and left out. All flares have at least a few data points above 2σ.

CHIRON Hα flares are identified by eye based upon sudden variations against the gradually varying background flux, which may represent non-flare-related changes (e.g., rotational modulations) in the stellar active regions (Maehara et al. 2020). Rather than spline fitting, we choose the equivalent width quiescent value to be the minimum of the immediate surrounding area (see Figure 7). Further analysis of Hα variations will be discussed in a future paper (Y. Notsu et al. 2023, in preparation).

4. Analysis and Results

4.1. Calculated Quantities

From the quiescent-subtracted light curves (see Section 3.1), the rise times, peak amplitudes, total durations, $t_{1/2}$ values (FWHM durations), impulsiveness indices, and equivalent durations are calculated. Note that we follow Kowalski et al. (2013) and define the impulsiveness index as $\mathcal{I} = I_{f,\mathrm{peak}}/t_{1/2}$, where $I_f(t)$ is the intensity contrast, $\mathrm{counts}_{\mathrm{target}}/\mathrm{counts}_q - 1$, and $t_{1/2}$ is in minutes. Equivalent durations are converted to fluences (energies) following Section 2.3. These quantities are listed between Table 4 and Appendix B.

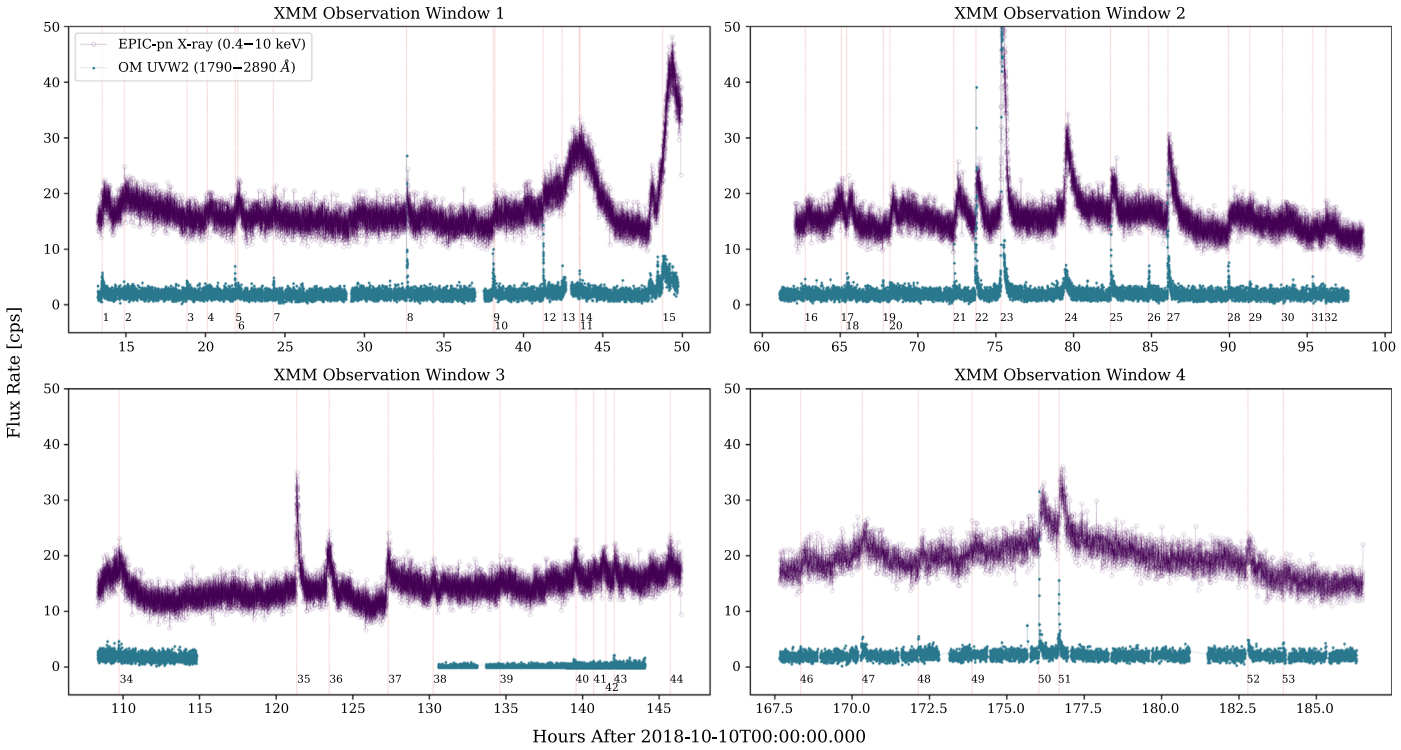

Figure 3. XMM-Newton light curves with 10 s binning. Vertical red lines correspond to a flare peak, with the Flare ID labeled at the bottom.

For energy calculations, we use a Monte Carlo simulation that varies the flare count rate by $\pm 1\sigma$ for every data point. We use 1000 iterations to produce consistent results between different runs. Reported values and errors are the mean and standard deviation of these trials. Reported errors for the XMM EPIC-pn X-ray are based on the difference between temperature values chosen in WebPIMMS (see Section 2.3), as these dominate over the statistical rate uncertainty.

4.2. Flare-rate Analysis

The U-band energies are organized into a cumulative flare frequency distribution (FFD) by calculating the number of flares with equivalent duration greater than E, $N = \int_E^\infty n(E)dE$ and dividing by the total monitoring time (74.15 hr). This FFD is shown in Figure 10. To our knowledge, this is the first systematic flare-rate analysis of AU Mic in the U band and there are few similarly detailed studies for other M0–M1 stars.

From the 25 LCOGT U-band flares, we calculate an average energy of $\langle \log E_U \rangle = 31.74$ erg and an average energy-loss rate of $\log \mathcal{L}_U = 28.13$ erg s^{-1}. The only other early-type M-dwarf flare star system with similar quantities determined is the eclipsing binary YY Gem (Lacy et al. 1976). Compared to YY Gem, AU Mic has around a 18 times smaller average flare energy and a 4 times smaller energy-loss rate due to flaring. We extrapolate flaring rates for AU Mic and YY Gem to estimate the occurrence of extreme flares. For 10^{34} erg flares, the expected number of flares greater than this energy ("flares $> E_U$") is 0.078 and 0.242 flares $> E_U$ per day for AU Mic and YY Gem, respectively. For 10^{35} erg flares, we expect 0.015 and 0.096 flares $> E_U$ per day for AU Mic and YY Gem. The FFD is fit to a power law of form $\log \nu = \alpha + \beta \log E_U$ (see Figure 10), and the resulting values are $\alpha = 23.42 \pm 4.78$ and $\beta = -0.72 \pm 0.15$. This value of β is consistent with other M dwarfs from Lacy et al. (1976), who reports values ranging from -0.4 to -1.1. We compare the FFD of AU Mic to that of a late-type M-dwarf star, Proxima Centauri (Walker 1981) which has a much lower average flare energy, as expected from the other later-type M dwarfs in Lacy et al. (1976). The energy-loss rate of AU Mic is compared to a wider range of M dwarfs in Figure 11, which compiles results from the much older 10 Gyr Galactic bulge population of flare stars reported in Osten et al. (2012). We can further estimate the expected mean energy-loss rate using α and β, along with estimated minimum and maximum flare energies, $E_{\rm min}$ and $E_{\rm max}$, to calculate $\mathcal{L}'$ following Lacy et al. (1976). $\mathcal{L}'$ accounts for numerous flares much below the observational detection limit. However, given the calculated β value and that most of the total flaring energy is contributed by the larger flares, lower $E_{\rm min}$ values will not change the final value of $\mathcal{L}'$ significantly. Assuming $E_{\rm min} = 10^{30}$ erg and $E_{\rm max} = 10^{35}$ erg, we find $\log \mathcal{L}' = 28.18$ erg s^{-1}. This value is very similar to the value of $\log \mathcal{L}_U$ in Figure 11, as expected for early-type M stars (Lacy et al. 1976).

A preliminary X-ray FFD using XMM EPIC-pn flares is shown for comparison in Figure 10. The slopes of the X-ray and U-band FFDs are remarkably similar, but the X-ray flares are shifted to larger energies. In fitting the slope, several X-ray flares in the lower-energy regime and one in the high-energy regime have been excluded. The slope is -0.66 if all flares are used, for reference. Paudel et al. (2021) finds an FFD slope of -0.65 ± 0.19 for NICER flares on EV Lac, which is consistent with our preliminary values of β regardless of whether all flares or only flares from the middle-energy regime are used for the FFD fitting. However, other studies have found a generally wide range of X-ray FFD slopes for M dwarfs. Audard et al. (2000) finds slopes ranging from -0.5 to -1.2 and averaging around -0.8; for reference, their value for EV Lac was -0.76 ± 0.33. Kashyap et al. (2002) finds higher slopes around -1.6 for FK Aqr and V1054 Oph. In a larger study,

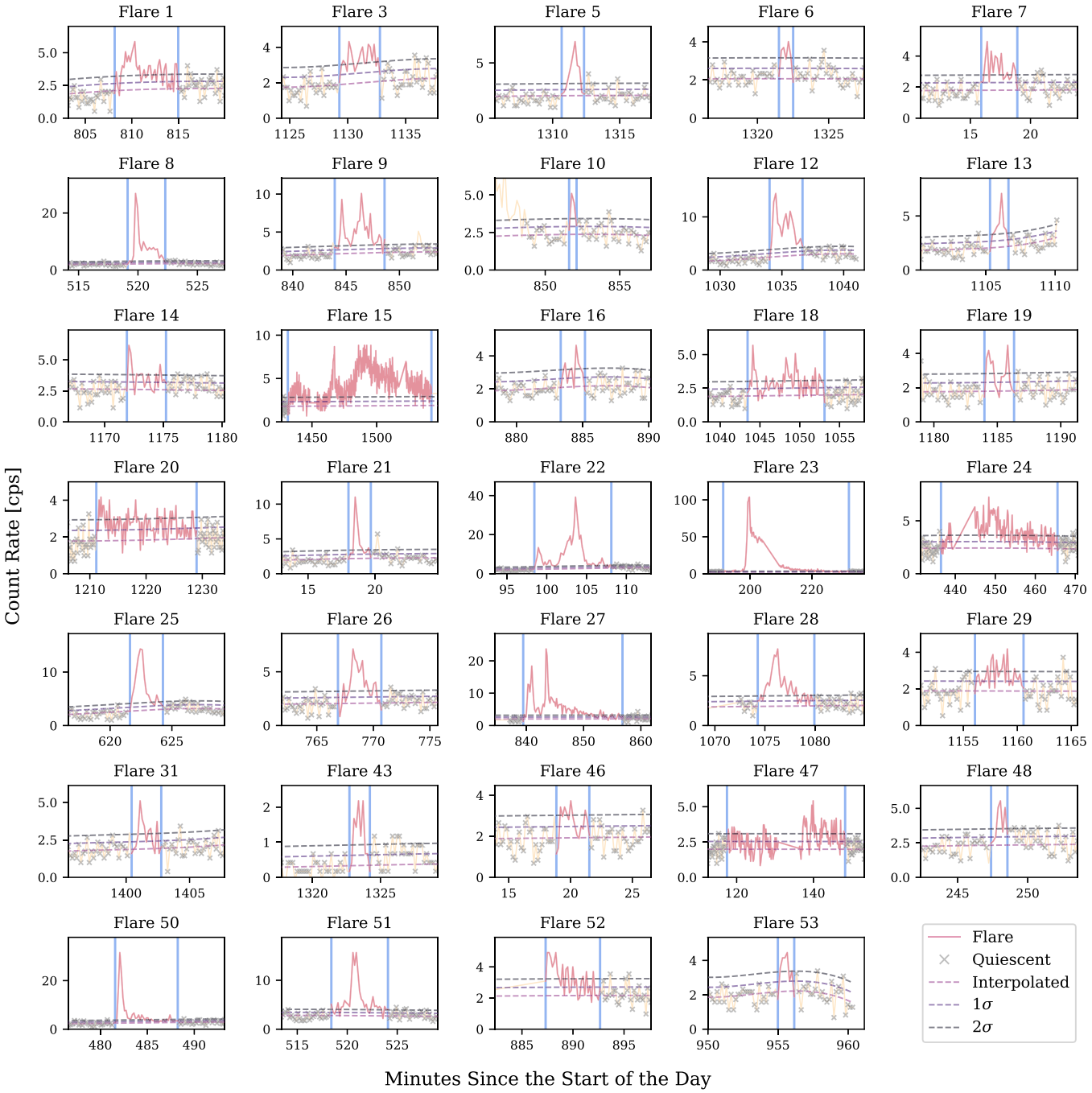

Figure 4. Individual flares in the XMM-Newton OM *UVW2* light curve with 10 s binning. The solid yellow line outlines the light curve, the solid red line shows flaring times, and gray crosses show times used to calculate the local quiescent level. The dashed lines show the estimated quiescent level, as well as the 1σ and 2σ local uncertainty levels. The vertical solid blue lines mark the chosen beginning and end times of each flare. The ID for each flare is listed above its plot.

Caramazza et al. (2007) finds a cumulative slope of -1.2 ± 0.2 for 165 low-mass (0.1–0.3 $M_{\odot}$) stars from the Orion Nebula Cluster (ONC). Similarly, Stelzer et al. (2007) finds slopes of -1.4 ± 0.5 and 1.9 ± 0.2 for stars in Taurus and the ONC, respectively. For comparison, stars with masses above 1 $M_{\odot}$ in the ONC and Cygnus OB2 have slopes around -1.1 ± 0.1 (Albacete Colombo et al. 2007). Compared to these results, the slope derived from AU Mic is not as steep as many other M dwarfs.

Based on the energy budget from Osten & Wolk (2015), we expect the $E_{\rm SXR}/E_U$ ratio to be about 2.72. For the six flares with both X-ray and *U*-band responses (see Appendix B), this ratio is 1.5 on average. However, the ratio between the FFD power laws at a given cumulative flare rate is 2.68, which is consistent with the previous budget. This implies that, while the energy budget varies from flare to flare, the average emission during a given time period (at a given cumulative rate) may lead to the previously established energy budget obtained from noncontemporaneous data or FFD comparisons. This may be due in part to detection thresholds and the resulting flare durations between the *U* band and X-rays, but warrants further investigation. Specifically, we intend to explore the relations among coronal thermal energy and SXR and extreme ultraviolet (XEUV) energies from temperature

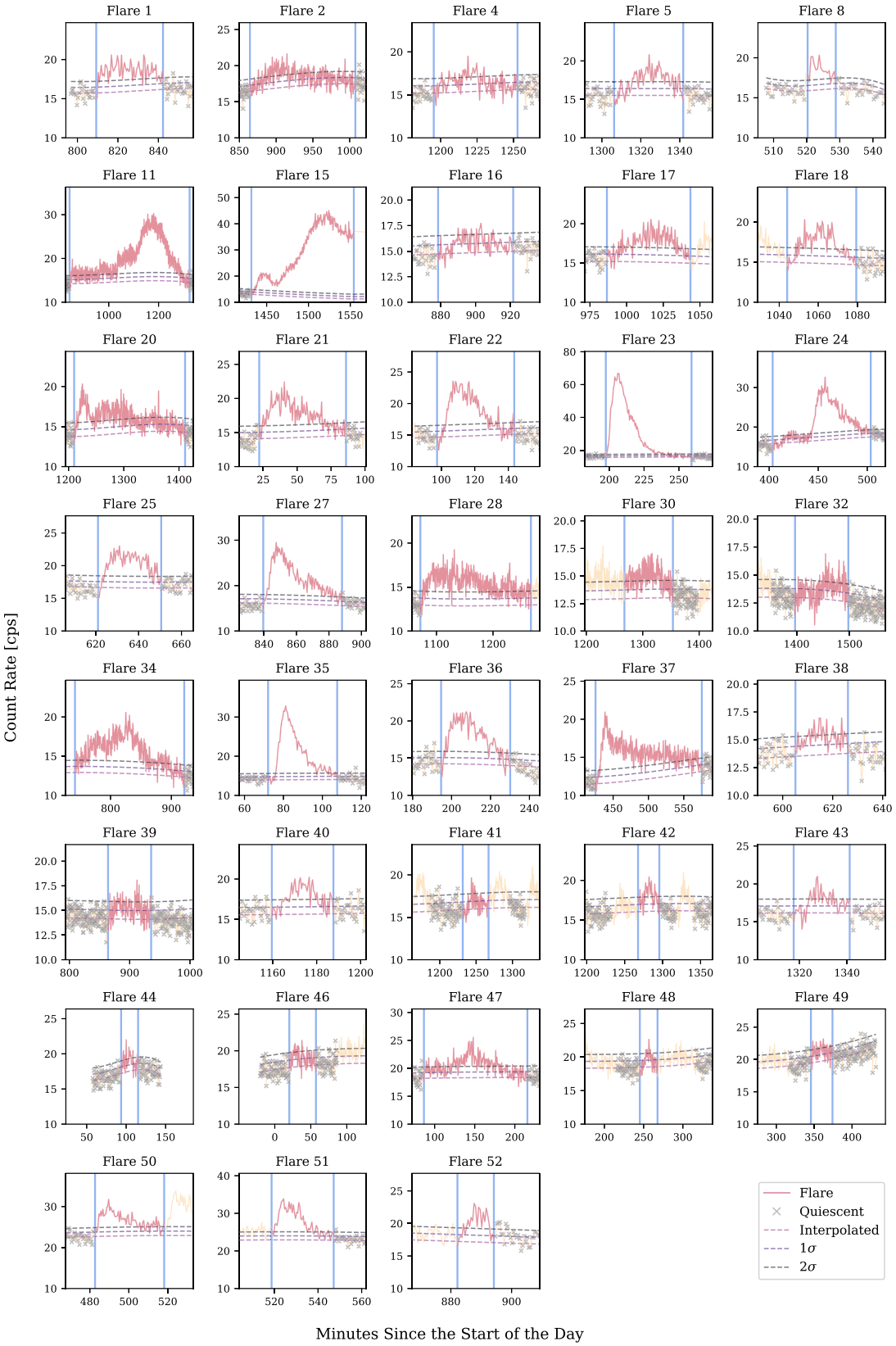

Figure 5. Individual flares in the XMM-Newton EPIC-pn X-ray light curve with 30 s binning for clarity. Symbols are in the same format as Figure 4. See Figure 3 for the 10 s binned data that were used for the analysis.

analysis of RGS spectra following Audard et al. (2000) and Pillitteri et al. (2022) in future work.

In summary, the *U*-band flaring rate and FFD slope of AU Mic is consistent with other M dwarfs. However, the empirical energy relationships between the X-ray and *U* band suggest that simultaneous observations of each flare give a different picture than energy conversions obtained from noncontemporaneous FFDs at different wavelength regimes.

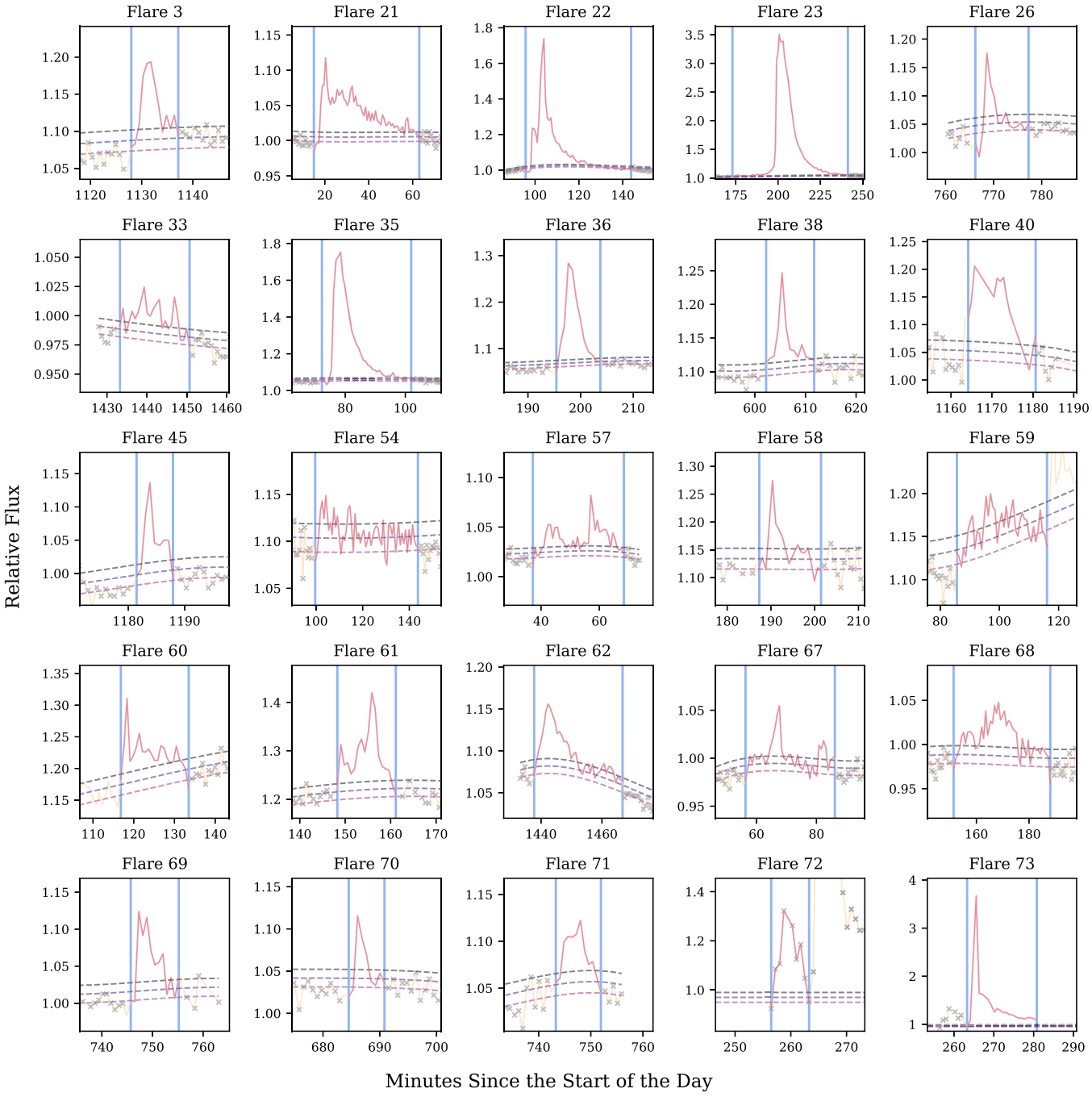

Figure 6. Individual flares in the LCOGT *U*-band light curve. Symbols are in the same format as Figure 4.

4.3. Light Curve and Flare Cross-Correlations

We perform cross-correlations for XMM observation windows 2 and 4 (refer to Figure 3) by following a modified version of the cross-correlation method in Mitra-Kraev et al. (2005). First, a time grid with 10 s spacing is defined on the XMM OM *UVW2* light curve along times where observations overlap with the XMM EPIC-pn X-ray. Count rates are interpolated along this common time grid. Then, the XMM EPIC-pn X-ray light curve is shifted ± 3000 s off from the original starting point, in steps of 10 s. For each shift, a sample Pearson correlation coefficient ($r_{\rm Lag}$) is calculated between the overlapping times of the light curves. The time shift at $r_{\rm Lag}^{\rm max}$ represents the time when the light curves are most correlated, and the lag at 90% of this value represents the 1σ uncertainty. Window 2 gives $r_{\rm max} = 0.70$ at a time lag of -250^{+150}_{-200} s, where the X-ray lags behind the XMM OM *UVW2* response. Window 4 gives $r_{\rm max} = 0.32$ at -200^{+80}_{-370} s. As the entirety of the 1σ region lies below 0 s for windows 2 and 4, flares peak earlier in the *UVW2* band than in X-rays on average. This is consistent with the findings of Mitra-Kraev et al. (2005) and showcases that this relation holds in the presence of the X-ray's large-scale variations in window 4. For completeness, window 1 reports $r_{\rm max} = 0.575$ at a lag of -780^{+780}_{-1270} s, but these are skewed due to the large, complex X-ray flares. Window 3 is left out due to missing *UVW2* data.

We perform the same cross-correlation for each individual flare with both XMM-Newton OM *UVW2* and EPIC-pn data.

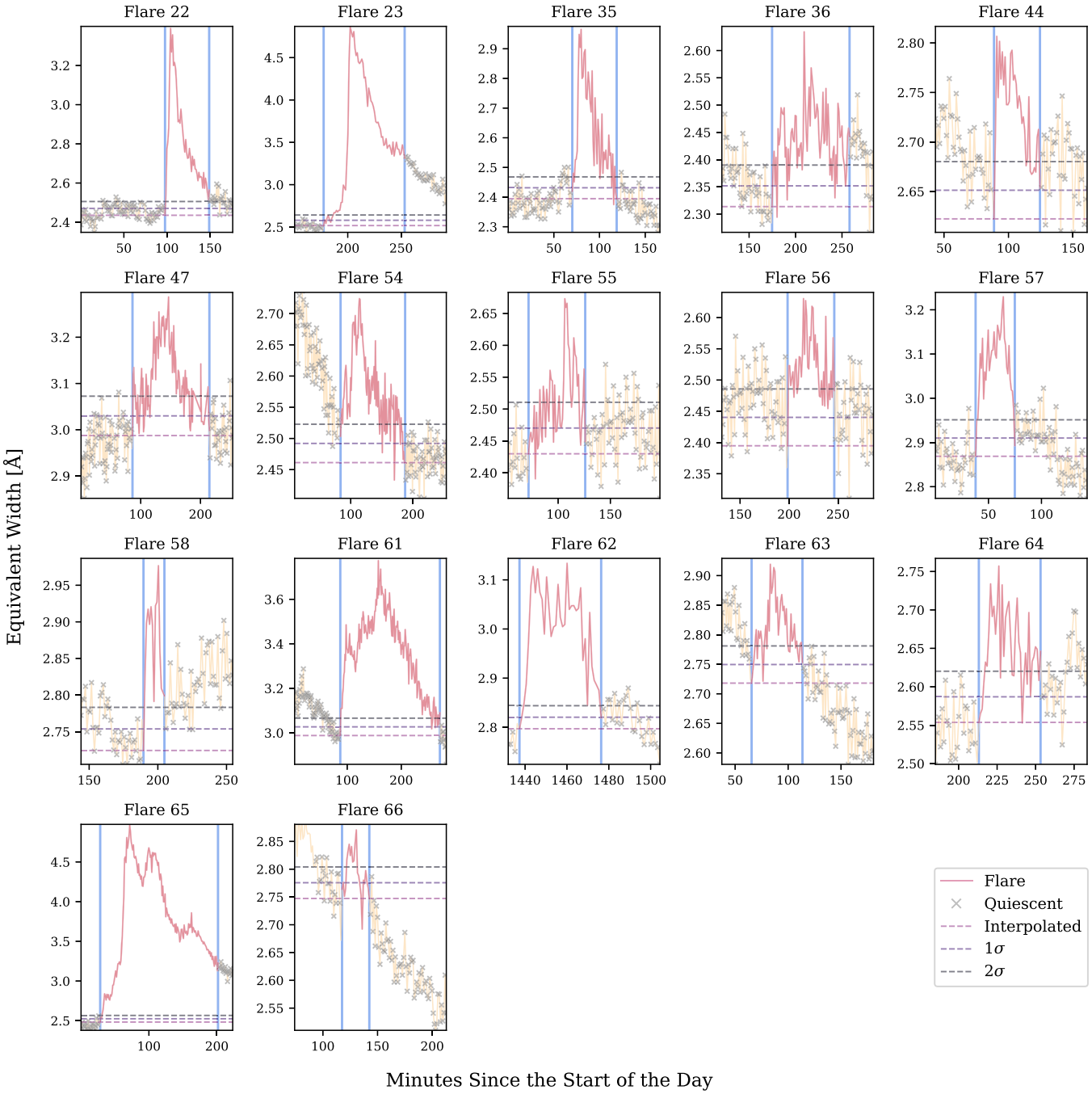

Figure 7. Individual flares for the CHIRON Hα equivalent widths. Diagrams are in the same format as Figure 4.

The $\pm$3000 s time shift used for the observation windows sometimes preferentially selects the largest nearby flare (e.g., Figure 12). Therefore, we explore a range of time shifts around each flare. Shifts of 1 ks are preferred in almost all cases, as $r_{\rm Lag}$ tends to decease with increasing range and large flares in surrounding areas can dominate widescale calculations. However, some time ranges are widened as the peak differences are greater than 1 ks away or specific shapes in the light curves affect the outcome. The coefficients for all flares are positively correlated, with most having medium ($r > 0.3$), if not high ($r > 0.5$), associations, with the exception of the small Flares 5 and 16. The X-ray lags behind the *UVW2* in all cases, with an average of -392 s.

Coefficients, lags, and time shift adjustments are listed in Table 4. Values are also compared with the original study of Mitra-Kraev et al. (2005) in Figure 13. Of note, this analysis implies that X-ray flaring emission lags behind the *UVW2* when both responses are observed, as expected from the chromospheric evaporation model and the TNE.

4.4. Thermal Empirical Neupert Effect Criteria

The time lags in Figure 13 are qualitatively consistent with the ENE. We leverage the high-time-resolution properties of our data set to examine the stellar ENE in more detail.

Though there are multiple metrics for quantifying the ENE, we choose the timing between the peaks of the XMM OM

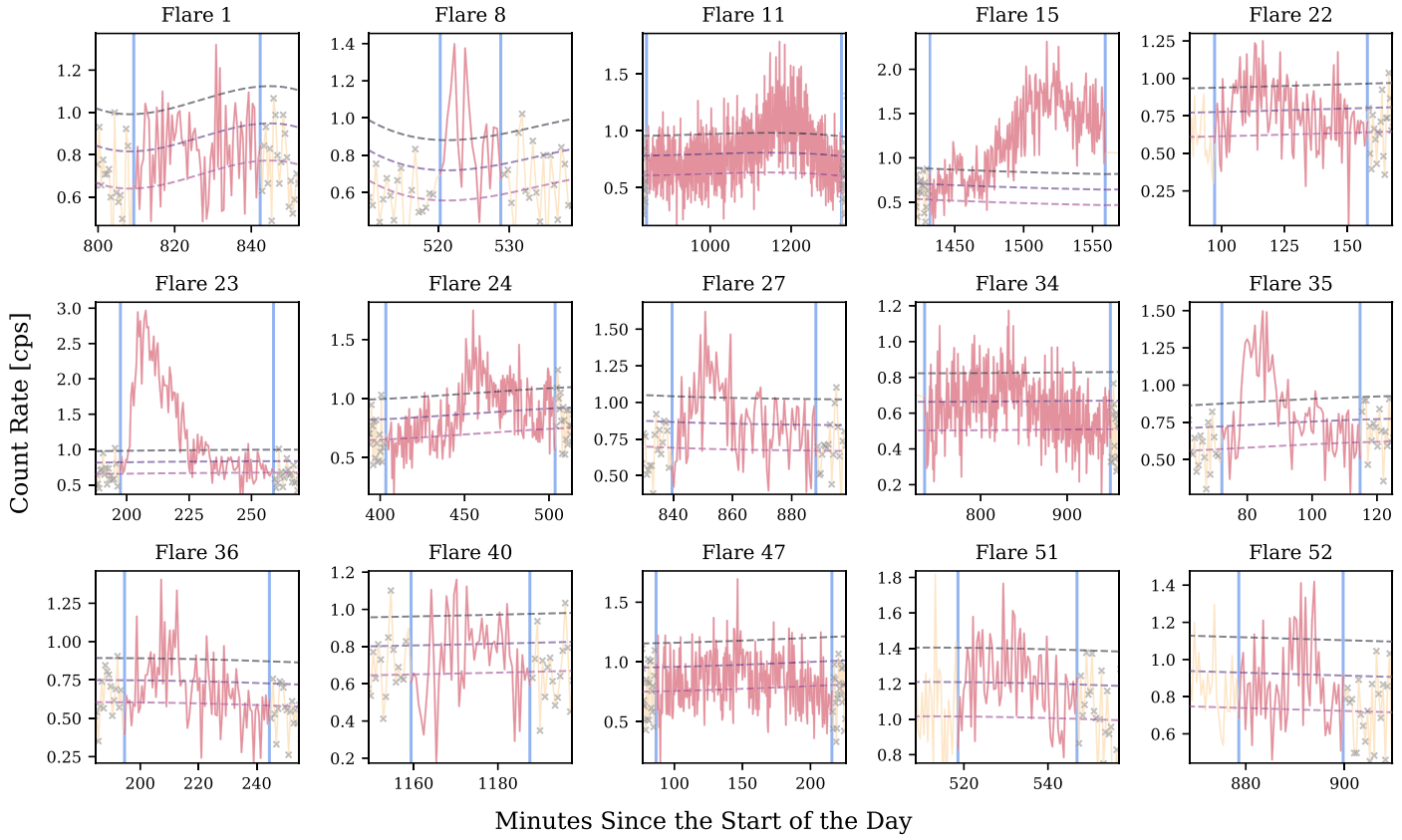

Figure 8. Individual flares in the XMM-Newton RGS X-ray light curve. Timings for these flares are adopted from their EPIC-pn counterparts. Symbols and colors are in the same format as Figure 4.

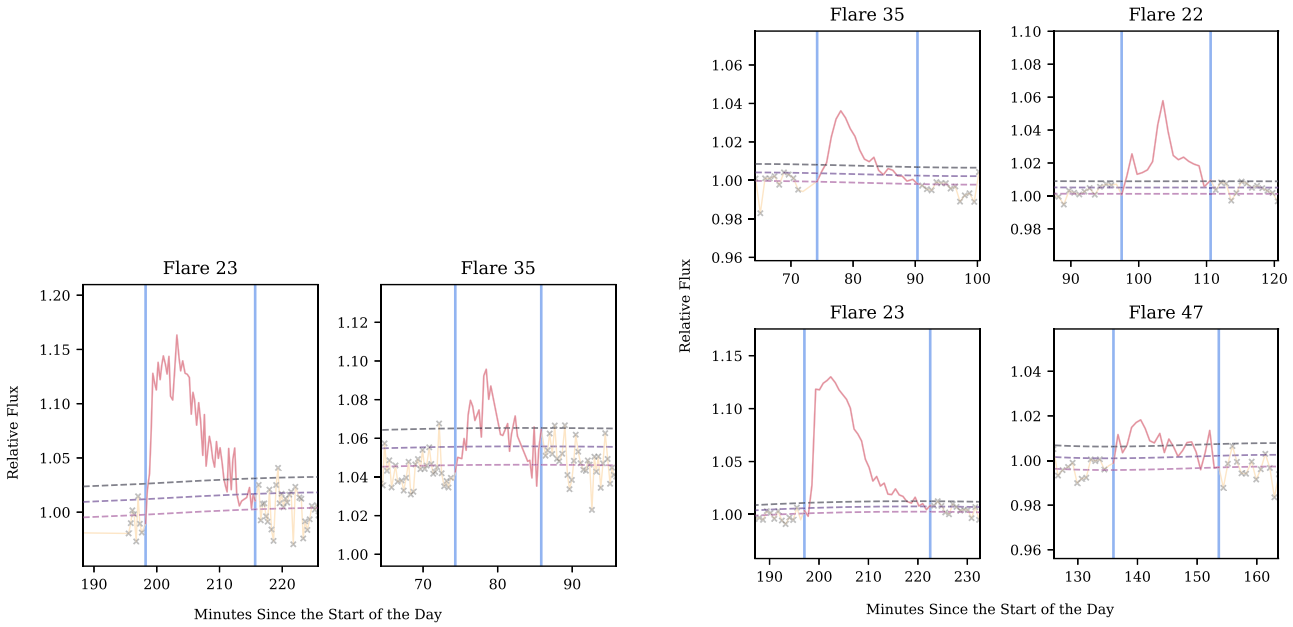

Figure 9. Individual flares in the LCOGT *V*-band (left) and CTIO/SMARTS 0.9 m *V*-band (right) light curves. Diagrams are in the same format as Figure 4.

UVW2 (as a proxy for HXR) and XMM EPIC-pn X-ray (here, SXR) time derivative, $\Delta t_{\rm peaks}^{\rm der}$ (Neupert 1968; Dennis & Zarro 1993). Other methods are then tested against this. We favor this timing metric over others (e.g., *UVW2* end and SXR peak) as it does not rely on flare start or end definitions. We combine this with the two-part Neupert criteria of Veronig et al. (2002), which included the timing difference normalized by the HXR (here, *UVW2*) duration, $\Delta t_{\rm norm}$, to mitigate bias toward intense flares or against long-duration flares. The original conditions of this metric are ($|\Delta t_{\rm peaks}^{\rm der}| < 1$ min) or ($|\Delta t_{\rm norm}| < 0.5$ units). However, based on the uncertainties due to differences in the *UVW2* and SXR time

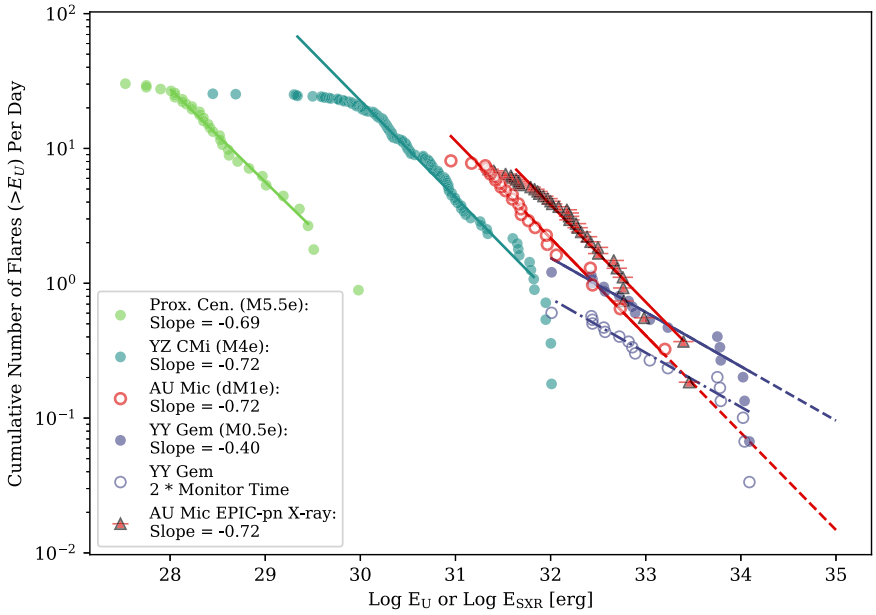

Figure 10. AU Mic's LCOGT *U*-band and XMM EPIC-pn X-ray cumulative FFD compared to other *U*-band FFDs from active dMe's reported in the literature (Section 4.2). We did not record any flares in the extreme-high-energy regime where the slope steepens sharply, and only one in the lower regime where the slope stays roughly constant. We note the vertical shift if YY Gem's monitoring time is doubled, accounting for its status as a binary system (Lacy et al. 1976).

Table 4
Calculated Quantities and Neupert Classification Criteria

ID	$t_{1/2}^{(1)}$ (minute)	$\mathcal{I}^{(1)}$	L_{UVW2}^{peak} $10^{29}\frac{\text{erg}}{\text{s}}$	L_{X}^{peak} $10^{29}\frac{\text{erg}}{\text{s}}$	$\Delta t_{\text{peaks}}^{\text{der}}$ (minute)	Δt_{norm}	SNES	D	$p_{\text{K-S}}$	r_c	$r_{\text{Lag}}^{\text{max}}$ (2)	Lag (s)	Classification(3)
1	5.98	0.28	1.13	1.30	0.21	0.03	0.21	0.5	0.00	0.73	0.48	-250^{+180}_{-210}	N
5	0.69	3.46	1.50	1.39	−3.28	−1.97	−0.09	0.7	0.00	0.58	0.26	-310^{+70}_{-390}	Q
8	0.35	32.66	7.57	1.62	−0.49	−0.15	0.20	0.8	0.04	0.64	0.42	-90^{+0}_{-140}	N
15	99.37	0.04	2.14	7.09	−9.93	−0.09	0.14	0.2	0.00	0.98	0.72	-1080^{+620}_{-820}	N/Q
16	1.20	0.98	0.77	0.95	−1.21	−0.66	0.08	0.7	0.00	0.33	0.17	-330^{+10}_{-230}	N/Q
18	8.00	0.24	1.16	1.61	−6.94	−0.72	0.19	0.5	0.12	0.85	0.45	-540^{+10}_{-80}	Q
20	17.22	0.08	0.73	1.57	−6.07	−0.34	0.24	0.5	0.94	0.83	0.55	-160^{+10}_{-460}	N/Q
21	0.30	13.68	2.71	2.25	−8.04	−4.82	0.64	0.8	0.00	0.52	0.37	-730^{+10}_{-270}	Q
22	0.63	21.37	11.18	2.23	0.23	0.02	0.51	0.2	0.82	0.94	0.49	-490^{+220}_{-30}	N
23	2.21	20.13	31.09	10.78	−1.30	−0.03	0.18	0.1	0.96	0.99	0.82	-250^{+130}_{-150}	N
24	25.51	0.08	1.47	3.42	1.51	0.05	0.21	0.3	0.69	0.97	0.73	-380^{+70}_{-190}	N/Q
25	0.76	5.32	3.52	1.91	−2.94	−1.10	0.53	0.8	0.00	0.73	0.42	-420^{+190}_{-330}	Q
27	3.54	2.97	6.63	2.85	−0.10	−0.01	0.24	0.2	0.44	0.98	0.64	-250^{+30}_{-110}	N
28	1.40	2.11	1.76	1.62	0.57	0.10	0.29	0.8	0.00	0.62	0.31	-970^{+370}_{-60}	N
43	0.87	6.25	0.57	1.18	−0.23	−0.15	0.70	0.5	0.39	0.65	0.38	-230^{+190}_{-100}	N
46	2.32	0.40	0.55	1.16	−2.48	−0.93	0.53	0.7	0.02	0.32	0.38	-440^{+0}_{-0}	Q
47	30.35	0.06	1.05	1.68	−0.25	−0.01	0.11	0.9	0.15	0.33	0.51	-170^{+0}_{-0}	N
48	0.72	1.91	0.98	1.17	−1.45	−1.24	0.00	0.9	0.00	0.32	0.35	-370^{+10}_{-150}	N/Q
50	0.41	28.31	8.90	2.01	−2.59	−0.39	0.41	0.6	0.00	0.77	0.39	-450^{+40}_{-10}	N/Q
51	0.78	5.97	3.95	2.54	−0.09	−0.02	0.43	0.4	0.12	0.85	0.47	-220^{+70}_{-10}	N
52	4.72	0.27	0.85	1.35	2.32	0.44	0.09	0.8	0.77	0.64	0.50	-100^{+110}_{-20}	N/Q

Note. Terms: $t_{1/2}$ is the FWHM timing, $\mathcal{I}$ is the impulsiveness, L^{peak} is the luminosity at the peak of the flare, SNES is the maximum cumulative Neupert effect score, D is the maximum difference in the Kolmogorov–Smirnov (K-S) test, $p_{\text{K-S}}$ is the p-value of the K-S test, r_c is the sample Pearson coefficient between the cumulative *UVW2* response and X-ray response, and $r_{\text{Lag}}^{\text{max}}$ is the maximum sample Pearson coefficient calculated during the cross-correlation of the light curves around a flare.(1) XMM OM *UVW2* values, specifically.(2) Time shift ranges are changed to 500 s for Flares 46 and 52, 1500 for Flare 16, 2000 for Flares 5, 21, and 23, and 3000 for Flares 15, 25, and 28.(3) N: Neupert flare (pass both timing criteria), Q: quasi-Neupert (pass neither). N/Q pass only one timing criteria. These should generally be considered Neupert, but continuing studies will further refine placement.

grids, as well as using a 30 s binning for the SXR derivative, we increase the window slightly to ($|\Delta t_{\text{peaks}}^{\text{der}}| < 1.5$ min) or ($|\Delta t_{\text{norm}}| < 0.6$ units). Results are shown in Figure 14, compared to the *UVW2* impulsiveness and peak luminosity ratio. Notably, the most impulsive flares also show the highest peak luminosity ratios and pass the timing criteria. Results are also tabulated in Table 4. The figures for and classification of each flare are shown in Appendix C.

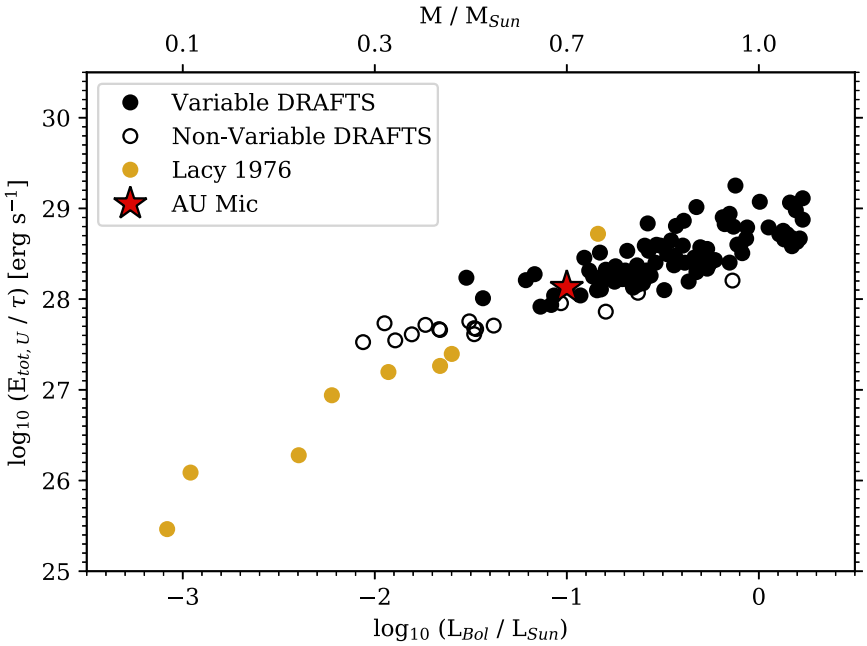

Figure 11. We recreate Figure 8 of Osten et al. (2012), showing the *U*-band average energy loss due to flares compared to bolometric luminosity, with AU Mic. "DRAFTS" is the Deep Rapid Archival Flare Transient Search, aimed at the older (∼10 Gyr) flaring stellar population within the Galactic bulge. AU Mic is consistent with the slope extended from the other single M dwarfs and the apparent turnover with old solar-type stars from the Galactic bulge.

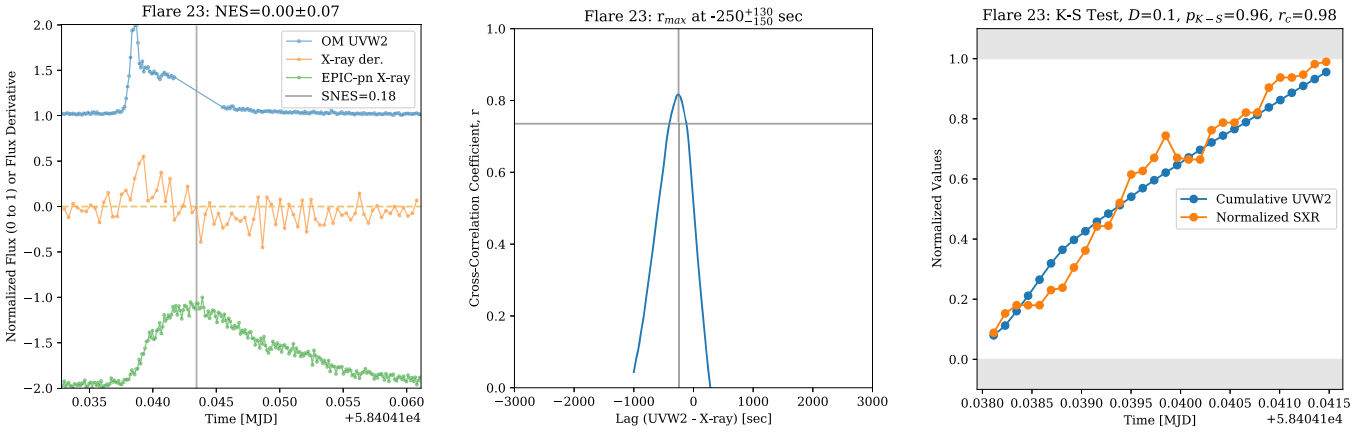

(a) (b) (c)

Figure 12. Summarizing figures for the methods used in Section 4.4. (a) The light curves for the *UVW2* and X-ray response, as well as the X-ray time derivative, are shown for Flare 23. The vertical gray line shows the time at highest SNES. (b) The cross-correlation coefficients for different lag times. The vertical gray line indicates the lag time at $r_{\max}$. The horizontal gray line intersects the 90% percentile, which gives the lag time uncertainty. (c) The cumulative distributions used for the K-S test. Gray bars show the regions where points were discounted to create a normalized distribution for the X-ray response.

We calculate the Neupert effect score (NES) of McTiernan et al. (1999). Namely, for each data point along the *UVW2* flare, we check if the signs of the *UVW2* flare-only flux and the X-ray time derivative are the same. If they are, +1 is added to the NES, and −1 otherwise. The score is then normalized by the total number of data points. The Monte Carlo simulation from Section 4.1 is used to report average values and standard deviations.

The NES is intended to give a straightforward and quantifiable indication that a flare follows the Neupert effect. Unfortunately, this method returns near-zero values for all flares, with highly variable standard deviations. This is likely due to the noise of the SXR derivative, which fluctuates between positive and negative between most points. We attempt to improve this score by using a three-point running median smoothing before calculating the derivative, but changes are minimal. If the noise floor is taken into account rather than relying only on the sign of the data points, the NES is often close to 1, as the relatively slow decay of the SXR puts the SXR derivative within the uncertainty range. This score is heavily improved with intense smoothing, such as the box function convolution used to estimate the derivative peak (see Section 2.3), but this is not applied in the final analysis as the resulting curves away from the peaks can be unrepresentative of the exact derivative.

We define a second Neupert effect score (SNES), which is the maximum value of the time-cumulated NES. This is done in an effort to minimize the effects of long decay phases and to focus on the differences around the peak values of the *UVW2* and the X-ray derivative. While these scores generally show

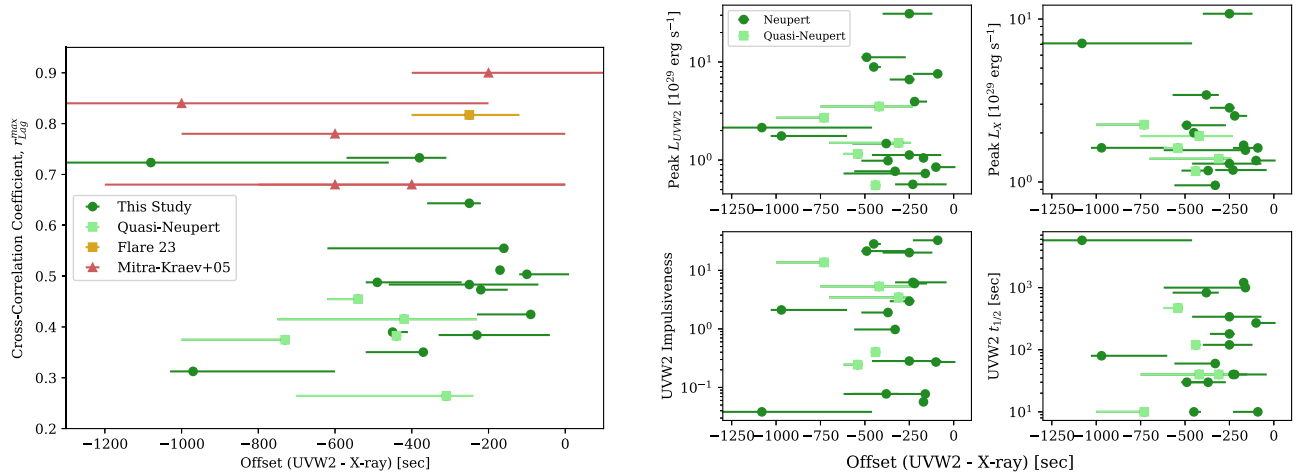

Figure 13. Left: X-ray response lags for the 21 XMM-Newton flares with both components. On average, these lag uncertainties are improved by a factor of 5 over the previous study of Mitra-Kraev et al. (2005) with lower time resolution. We see an intrinsic spread in lags from 0 to −1000 s and an average of −392 s. Flare 23 and quasi-Neupert flares are indicated. Right: the lag is compared to peak luminosities, impulsiveness, and $t_{1/2}$ from Table 4. No significant correlations are found.

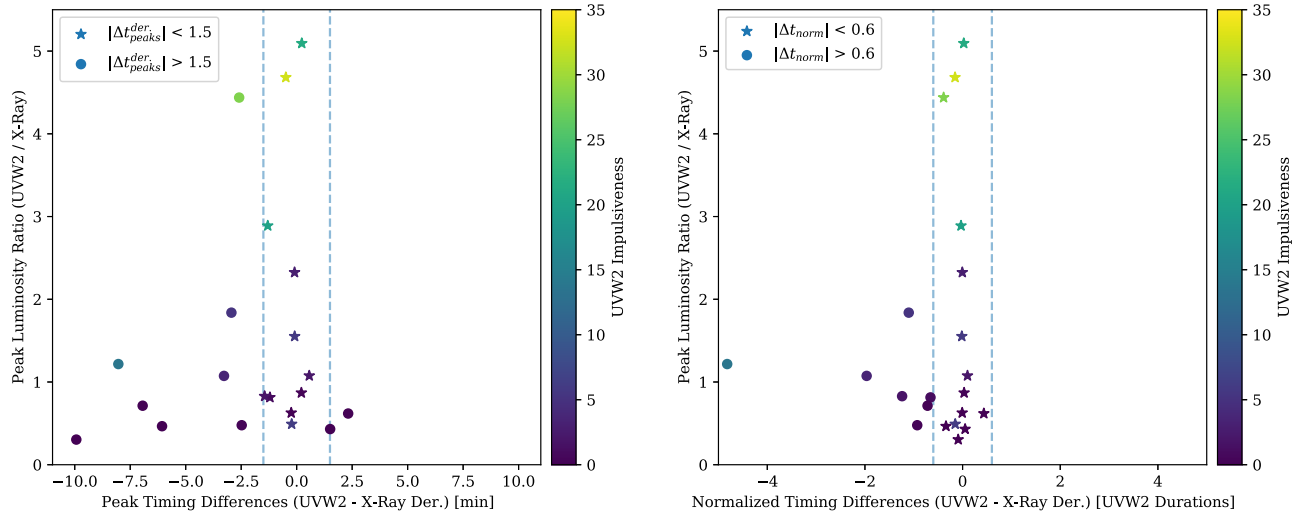

Figure 14. The Neupert effect timing differences plotted against the peak luminosity ratios for the 21 XMM-Newton flares that have both *UVW2* and X-ray components, color-coded by impulsiveness. We see a suggestive trend that flares with higher impulsiveness tend to have higher *UVW2*/X-ray peak luminosity ratios and exhibit the Neupert effect as well. Left: $\Delta t^{\rm der}_{\rm peaks}$ is shown, with vertical dashed lines showing the ±1.5 minutes mark, which 11 flares lie between. Right: $\Delta t_{\rm norm}$ ($\Delta t^{\rm der}_{\rm peaks}$ normalized by *UVW2* duration) is shown, with dashed lines showing the ±0.6 units mark; 14 flares pass this metric.

higher and varied values, they do not show a correlation with the Neupert timing criteria and are rather dependent on flare shape. For example, the SNES of the largest flare is smaller than expected due to a long rise phase, shown in Figure 12.

Another facet of the Neupert effect is a similarity in the shape between the *UVW2* cumulative and the SXR response of the flare. This similarity implies a common origin between responses, as the total energy deposited by the electrons would contribute to X-ray emission generation (similar to the microwave emission in Neupert 1968). A sample Pearson correlation coefficient (r_c; see Section 4.3) is calculated to test the similarity in the simultaneous rise of these responses. The values of this coefficient are extremely high (>0.9) for some Neupert flares and generally high for all. We also perform a Kolmogorov–Smirnov (K-S) test, which gives a test statistic, D, the farthest vertical distance between two cumulative distribution functions (CDFs), along with a p-score, $p_{\rm K-S}$. To simulate CDFs, the *UVW2* cumulative is first normalized between 0–1. Then, a SXR light-curve normalization is created by using a three-point running median to remove outliers, dividing by an average of the last five data points, and applying a 0–1 cutoff.

There are a few flares which show higher $p_{\rm K-S}$ only in certain phases. For Flare 22, testing only the rise phase reports a high $p_{\rm K-S}$, while the peak and decay do not. For Flare 23, the slow rise phase preceding the sharp increase in emission is removed to improve the score. Flare 15, however, reports a low $p_{\rm K-S}$ despite having an extremely high r_c, as the simulated X-ray CDF values are larger than the *UVW2* CDF, especially during the first peak. Overall, while there are a few high $p_{\rm K-S}$ values, there is not a clear trend that separates groups of flares with respect to the Neupert effect timing criteria. Examples are shown in Figure 12.

The relation between SXR peak flux and *UVW2* energy is expected to be $F_{\rm P,SXR} = k \cdot E_{UVW2}$ (see Lee et al. 1995 and Veronig et al. 2002), where $F_{\rm P,SXR}$ is the peak SXR flux and E_{UVW2} is the total *UVW2* flare energy. Note $F_{\rm P,SXR}$ and E_{UVW2} are connected linearly if k is a constant, implying a singular heating mechanism that produces a reliable relationship between responses (see Veronig et al. 2002). Using all

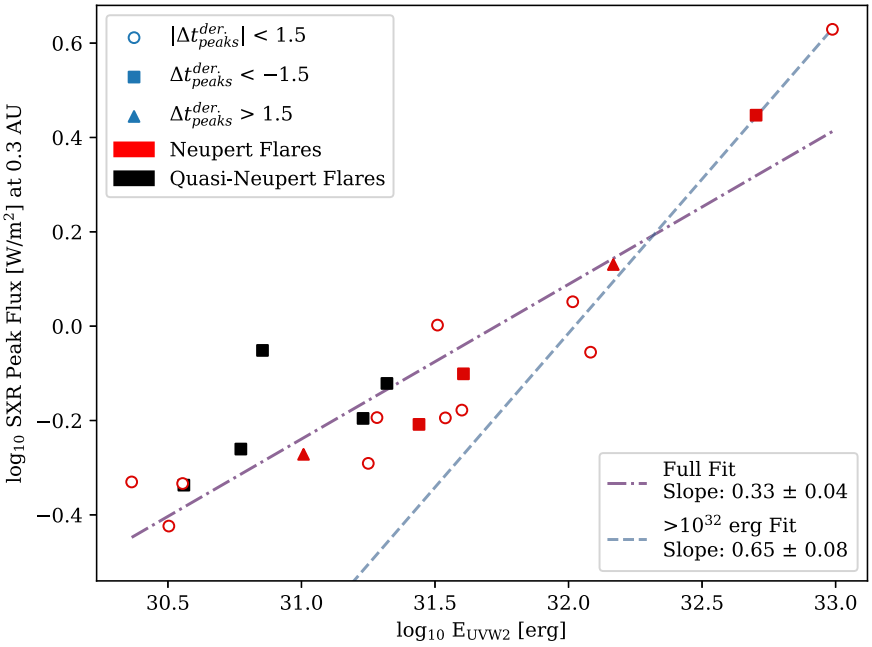

Figure 15. SXR peak flux vs. *UVW2* energy for the 21 XMM-Newton flares with both components. Square markers indicate that a flare has a value of $\Delta t^{\rm der}_{\rm peaks} < -1.5$ minutes (lag between *UVW2* and X-ray derivative peaks), triangle markers indicate $\Delta t^{\rm der}_{\rm peaks} > 1.5$, and open circles indicate that $\Delta t^{\rm der}_{\rm peaks}$ falls between these. Bright red coloring indicates that the flare shows the Neupert effect, while black points are classified as quasi-Neupert. We calculate slopes for the entire set of flares, as well as only for the largest ones ($E_{UVW2} > 10^{32}$ erg), in log–log space. We find that the expected slope of $b = 1$ for a linear relationship (Veronig et al. 2002) is neither met nor close in either case.

Table 5
Multiwavelength Classification Statistics

Classification	Label	Count	Percent Total	Percent Adjusted
Neupert	N	9	20%	43%
Neupert (passes one criterion)	N/Q	7	15%	33%
Quasi-Neupert	Q	5	11%	24%
Non-Neupert Type I	NN-I	12	26%	…
Non-Neupert Type II	NN-II	13	28%	…
Undetermined	Un	5	…	…

Note. Classifications for the 51 flares analyzed in the XMM-Newton *UVW2* and X-ray data. As timing choices can lead to significant changes in the Neupert and quasi-Neupert categories, flares that passed only one Neupert timing criterion are labeled with N/Q for posterity. $n_{\rm Un}$ are undetermined due to missing *UVW2* times. "Percent Total" uses the 46 flares with data available for both observations, while "Percent Adjusted" only uses the 21 flares with responses in both.

available flares, we calculate $k = 3.9 \pm 0.2 \times 10^{-33}$ W m^{-2} erg^{-1}, where the SXR flux is scaled to AU Mic's habitable zone (see Section 4). Values are plotted in Figure 15. Linear regression slopes in log–log space (b) are calculated for all flares and large ($E_{UVW2} > 10^{32}$ erg) flares only, as larger flares show a clear regime change. Neither group approaches the expected linear value of 1, but the slope from the larger flares is greater by a factor of 2. This is discussed further in Section 5.

In summary, we use two timing criteria to determine if flares are consistent with the thermal ENE. The first is the time difference between the *UVW2* response peak and the X-ray time derivative peak. The second is the time difference normalized by the *UVW2* flare duration. This normalized criterion is meant to mitigate the bias toward larger flares, which more readily show the Neupert effect. Of the 46 flares with both *UVW2* and SXR times available, 35% pass at least one timing criterion. We tested the NES against the timing results, but find that all scores are near-zero without significant X-ray time derivative smoothing. We also measured the similarity in shapes between the *UVW2* cumulative and SXR responses. We find expected agreements with some of the largest flares, but ambiguous results otherwise. Finally, we looked at the SXR flux and *UVW2* energy relationship expected if all flares were Neupert. We find that larger flares follow the expected trend much more than smaller flares, but neither are as close as anticipated.

4.5. Classification of Stellar Flares According to the Thermal Empirical Neupert Effect

The high time resolution of this data set has allowed us to explore several analysis metrics in stellar flares for the first time. We use the timing between the *UVW2* response peak and the X-ray derivative peak to categorize flares into four categories under the thermal ENE. Representative flares in each category are shown in Figure 16 (all flares are shown in Appendix C), and the results for the 51 XMM-Newton flares are summarized in Table 5.

The first category is "Neupert" (N), in which the *UVW2* flux and SXR time derivative peaks nearly coincide and both timing criteria are passed. This behavior is most similar to the traditional ENE in solar flare HXR/radio and high-temperature SXR emission. About 20% (nine flares) of the sample belongs to this group. The second category is "quasi-Neupert" (Q). These flares exhibit a response in both *UVW2* and SXR emission, but the light-curve peaks are well separated in time. About half as many events fall into this group. We also categorize flares that pass a single timing criterion only as being "N/Q"; most of these events only pass the normalized criterion. However, this designation is mainly used to identify

marginal cases, and we intend to revise classification in future work as complementary data sets are brought into the analysis. For this study, "N/Q" flares should be considered Neupert.

Of particular interest are the 25 events that exhibit a response in only one spectral region between the X-ray and *UVW2*. These may be due to weak responses that are within the noise, but their prevalence may also suggest alternative explanations (see Section 5). We classify these as non-Neupert flares. The 12 "non-Neupert Type I" flares are those where there is a SXR response but no *UVW*2 response. In the 13 "non-Neupert Type II" events, there is a *UVW*2 response but no detected SXR emission. Note that there are also five "Undetermined" (Un) XMM-Newton flares, where no *UVW*2 observations were taken.

At high time cadence, we find a large variety of multi-wavelength behavior of thermal emissions among the flares of AU Mic. In future papers, we plan to incorporate the nonthermal radio data from the campaign to develop a comprehensive ENE relationship among the flares from this star. Radiative-hydrodynamic modeling will also be pursued to explain each of the four types of empirical behaviors in terms of the TNE (chromospheric evaporation and condensation) and possible physical origins.

5. Discussion

According to the standard electron beam model of solar and stellar flares, nonthermal electrons rapidly heat the mid chromosphere, which causes mass and heat advection into the corona (see references in Section 1). The impulsive energy deposition of the chromosphere produces the NUV and optical continuum and emission lines, while the SXR radiation is emitted as the coronal loops fill with hot plasma to several tens of megakelvin. The loops then cool down over tens of minutes and shine brightly in subsequently lower-temperature SXR and extreme-UV (EUV) radiation signatures (Aschwanden & Alexander 2001). All the while, this process takes place over tens of minutes to hours through sequential heating and cooling of many loops and chromospheric footpoints (Warren 2006), with the heating rates early on being much larger and the reconnected loops much smaller than in the gradual phase.

We interpret the four categories of flares (see Section 4.5) in terms of this fundamental process, drawing from several, similar observations that have been reported in the literature.

Neupert flares follow the timing of the chromospheric evaporation model as expected. Of the 46 flares with both XMM-Newton *UVW*2 and SXR times available, 35% (nine "N" and seven "N/Q" flares in Table 5) pass at least one timing criterion, where the timing between the *UVW*2 response peak and the X-ray time derivative peak are within either 1.5 minutes or 0.6 *UVW*2 durations. In the 21 flares with both responses ("N", "N/Q," and "Q" flares in Table 5), 76% pass at least one of these timing criteria. In addition, we find that the X-ray response significantly lags behind the *UVW2*, which is expected under this model. We calculate the NES and SNES of the flares, but find the method to be inconclusive without heavy light-curve smoothing. These metrics may be more useful for brighter stars or solar studies and should be kept in consideration in future follow-up analyses. We find that the shapes of the cumulative *UVW*2 response and the SXR flux are similar, indicating a common origin.

It should be emphasized that "N/Q" flares are considered to be consistent with the Neupert effect. Timing differences across the SXRs occur due to the flare temperature evolution (Güdel et al. 1996; McTiernan et al. 1999), which depends on both the conductive and radiative plasma cooling timescales. The ratio between the two changes over time, with radiation dominating the decay (i.e., lower-temperature) phase (see Figure 9 of Osten et al. 2016). SXR emission from hotter plasma peaks earlier than from cooler plasma, and high-energy, hotter flares tend to have smaller timing delays (see Section 4.2 and Figure 5 of Güdel et al. 1996). Generally, high-temperature SXR derivatives peak around the same time as hard X-rays, while low-temperature SXR derivatives show little resemblance to the HXRs (see Figures 7–9 of McTiernan et al. 1999). Flares that would be labeled "N/Q" in our classification scheme from Güdel et al. (1996, 2002) may be fully consistent with another generalized Neupert effect that considers the energy balance between radiative cooling and impulsive heating, as constrained by nonthermal gyrosynchrotron emission. Thus, the choice of X-ray band and plasma temperature can bias the classification of flares and reveal noncorrelations, especially after the peak *UVW*2 phase. Note that the normalized timing criterion attempts to mitigate this bias toward intense flares, but it is not expected to cover all possibilities.

The timing differences of the quasi-Neupert flares may also be caused by significant contributions from additional heating mechanisms. A strong candidate for this is thermal conduction (see Longcope 2014 and references within for a comprehensive overview), where reconnection energy is transferred through heat transfer in the plasma along the flaring loop top-down to the chromosphere (see also Ashfield et al. 2022). Contributions from this could explain delayed X-ray time derivative peaks, and relatively small contributions from this may explain near-late timings like that of Flare 23. Likewise, cooling rates are also of interest. As noted before, McTiernan et al. (1999) finds flares from high-temperature plasma ($T > 16.5$ MK) are more likely to show the ENE than low-temperature plasma. The XMM EPIC-pn instrument measures flare plasma at 10–30 MK, encompassing both regimes. Thus, contributions from both regimes may skew Neupert effect results as the high-temperature plasma cools. This cooling may contribute to the poor K-S test correlations, even in Neupert flares. Alternatively, Li et al. (1993) finds long-durations flares can display a SXR peak before the HXR end, which contrasts some formulations of the ENE, due to evaporation-driven density enhancements failing to overcome hot plasma cooling. Veronig et al. (2002) further suggests that the power-law break in the SXR peak to NUV fluence (see Figure 15) is due to these flares that are dominated by thermal conduction transport into the chromosphere. Quasi-Neupert flares introduce a wide array of possibilities for flaring energy transfer, and future X-ray spectroscopic and temperature analysis, along with stellar flare modeling, will help determine individual flare origins.

Non-Neupert Type I flares are the most likely candidate for an alternative heating method, like thermal conduction. Following Petschek (1964), shock heating may occur after magnetic reconnection without a nonthermal electron beam. The heat energy would then be transferred down into the chromosphere through thermal conduction, driving chromospheric evaporation and producing SXR emission (Forbes et al. 1989). Consistent models have been designed for these types of flares (see Yokoyama & Shibata 1998, 2001), and future work will determine if non-Neupert Type I flares fall under this category or require additional physics.

Osten et al. (2005) gives possible explanations for non-Neupert Type II flares, which have *UVW2* responses yet lack X-ray emission. They suggest low ambient electron densities within the loop, heating at lower (or higher) temperatures than measured by the instrument, high amounts of magnetic trapping, or particles accelerated to MeV energies that penetrate into the lower chromosphere or photosphere and show continuum emission without significant chromospheric evaporation. Flares 3 and 26 have both *UVW2* and *U*-band responses, similar to the event featured in Osten et al. (2005). For the former, there is an arguably faint X-ray response and the *UVW2* response is small, which lends credibility to the low-temperature heating scenario. For the latter, the *UVW2* and *U*-band responses are reasonably sized, though short-lived. This likely rules out low-temperature heating by comparison to Flare 3. Efficient magnetic trapping may also be unlikely, as a longer decay would be expected. We predict that Flare 3 will have a low radio response while Flare 26 will have a bright response. We plan to analyze these time intervals in detail in future work to test these hypotheses and constrain the presence of accelerated electrons in the flares.

There are a few non-Neupert peculiarities that should be mentioned. Events like Flares 6 and 10 in the *UVW2* are likely secondary (sympathetic) flares of a preceding larger one despite being temporally separated. In these cases, their corresponding responses may be hidden within the larger preceding one or too small to observe. Likewise, there are arguably tiny responses to other bands, like in Flares 34 and 40, which did not pass flare selection. These situations all contribute to a potentially diverse flare-production environment and are important to keep in mind for future flare modeling. Whether Hα equivalent width flaring variations occur during non-Neupert flares is also of interest for models. Unfortunately, there are no accompanying CHIRON observations for any of the non-Neupert flares in this study.

The percentage of Neupert flares among the XMM-Newton flare pairs (76%) is similar to Dennis & Zarro (1993), which found 80% agreement in 66 solar flare pairs. This percentage is also higher than the 44% of solar flares from the large (1114 flare pairs) statistical study of Veronig et al. (2002). Note these studies discounted complex flares, flares with multiple possible pairings, and flares where the two responses did not start near each other to various degrees. Therefore, there are no comparable non-Neupert statistics available. Despite the high percentage of Neupert flares, the SXR flux to *UVW2* energy relationship is lower than expected (Figure 15). Veronig et al. (2002) showed a log–log slope near 1.0 ($b = 0.96 \pm 0.07$) for large flares and $b = 0.83 \pm 0.03$ including mid-sized flares. Namekata et al. (2017) similarly found a slope of 0.8 between white-light energy and GOES X-ray flux for solar flares above GOES class M2. Stelzer et al. (2022) expanded on that work with a scaled superflare from AD Leo and found a close, but steeper, slope of $b = 1.150 \pm 0.005$. While our results indicate that the chromospheric evaporation model plays a significant role in M-dwarf stellar flares, the large deviation from the ideal slope of 1 in Figure 15 implies other heating mechanisms besides nonthermal electron beam heating are necessary to understand many stellar flares. The existence and prevalence of non-Neupert flares further indicates that flare energy budgets do not follow one slightly variable relation.

Since ion production in Earth's thermosphere and ionosphere is sensitive to EUV radiation (Mitra 1974), extrapolations from X-ray flare observations to the EUV regime are considered useful in gauging exoplanet habitability (as in Chadney et al. 2017). Qian et al. (2011) finds that solar flare models showing the Neupert effect have a larger EUV enhancement during the impulsive phase. This leads to a greater ion production early on, but weaker electron and neutral density enhancements overall due to the short-lived impulsiveness. Broadly based on the findings of Qian et al. (2011), Neupert and quasi-Neupert flares in M dwarfs may also have comparable effects on an exoplanet's ionosphere.

Due to the similar energy ranges of the SXR (0.2–12 keV) and EUV (10–124 eV) regimes, it is expected that the presence of one response implies the other, as they both stem from ablated plasma (see Section 1). However, coupling their time evolution too tightly is known to cause low accuracy in solar modeling (Nishimoto et al. 2021), as the EUV emission peaks after the SXR. Some solar EUV flares also have a late phase which is not easily estimated by X-ray comparisons, where a second peak is observed hours after the primary event (Woods et al. 2011; Chen et al. 2020).

With this in mind, Neupert, quasi-Neupert, and non-Neupert Type I (X-ray-only) flares may help determine minimum EUV radiation effects, but they are unlikely to estimate maximum limits without proper multiwavelength EUV observations. However, non-Neupert Type II (*UVW2*-only) flares are unlikely to correspond to EUV emissions, as significant plasma heating is not expected. Thus, it may be inadvisable to do any EUV extrapolations based on only NUV observations.

Another possible complication is the large X-ray swell on 2018 October 10 (Flare 11). Notably, most of the enhancements during the swell match up with *UVW2* flares (e.g., Flare 9 at the start, Flare 14 at the peak); however, there is also at least one clear increase with no *UVW2* response about an hour before Flare 12 (see Figure 3). The maximum enhancement also has a slower decay than other X-ray flares of comparable or greater size, like Flares 23 or 27. Given this, the X-ray swell seems to be composed of coupled flaring events of different Neupert types, and it is currently unknown if any quiescent fluctuations play a part in sustaining the emission enhancement. Spectral analysis of the different regimes of Flare 11 may be able to shed light on these issues, but similar events in M dwarfs, if prevalent, may complicate autodetection or separation of individual X-ray events, Neupert classification studies, and extrapolations between wavelengths.

6. Summary and Conclusions

The purpose of this campaign is to build upon past studies and explore the physical parameters of M-dwarf flares using observations with long-duration temporal coverage and high time resolution of a single flaring star. In this paper, we comprehensively analyze a new, multiwavelength data set of AU Mic spanning the X-ray to the optical over 7 days, with *U*-band, *V*-band, and Hα data extending to $\sim$500 hr. The data used here include X-ray and *UVW2* bands from XMM-Newton and Swift, the Hα line and *V* band from CTIO/SMARTS 0.9 m, and the *V* and *U* bands from LCOGT (summarized in Table 2). This data set allowed us to analyze the thermal ENE in a large sample of stellar flares. Quantitative results are summarized as follows:

1. We find 73 unique flares, with 51 in the XMM-Newton OM *UVW2* and EPIC-pn X-ray data, 21 of which overlap in time (see further classification in Table 5).

2. Of the 21 overlapping flares, 16 show the Neupert effect, where the timing between the *UVW2* emission peak and X-ray time derivative peak are within 1.5 minutes or 0.6 *UVW2* durations. Five flares then show significant timing differences between responses (quasi-Neupert). Of the others, 12 flares show only X-ray responses (non-Neupert Type I), while 13 show only *UVW2* (non-Neupert Type II; see Table 5). From this, 65% of flares from AU Mic do not follow the thermal ENE.
3. We find that the NES of McTiernan et al. (1999) returns null results for our data without significant smoothing of the X-ray light curve. Defining a SNES, which takes the highest cumulative score along the flare, improves the results. However, these remain inconsistent between Neupert and quasi-Neupert flares.
4. The sample Pearson coefficients between the cumulative *UVW2* response and the X-ray response are generally high, indicating similar curve shapes. These are extremely high (>0.9) for a few Neupert flares. K-S tests between these can also give favorable results, but careful formatting of the curves is sometimes required.
5. The SXR peak flux to *UVW2* energy relation shows two distinct regimes, whereas a linear relation ($F_{P,SXR} = b \cdot E_{UVW2}$, $b = 1$ in log–log space) is expected under the Neupert effect. We calculate $b = 0.33 \pm 0.04$ using all flares with both responses and $b = 0.65 \pm 0.08$ for flares with $E_{UVW2} > 10^{32}$ erg (see Figure 15). Figure 11 of Veronig et al. (2002) also shows this division for solar flares, though both regimes have slopes closer to 1.0.
6. We find that the X-ray response lags behind the *UVW2* for all overlapping flares in this sample, with an average lag of −392 s. Note that the Neupert timing relation does not follow this trend.
7. We calculate a *U*-band FFD slope of $\beta = -0.72 \pm 0.15$, which is similar to other M dwarfs in the literature. We also calculate a preliminary X-ray FFD, which has a similar slope with higher flare energies. We find that among flares with X-ray and *U*-band responses, the empirical E_{SXR}/E_U ratio averages to 1.5. However, the ratio between a set cumulative number of flares per day is 2.68, similar to the canonical energy partition (2.72) of Osten & Wolk (2015).

The relationships between XMM-Newton OM *UVW2* and EPIC-pn X-ray flares and the variety between Neupert, quasi-Neupert, and non-Neupert types I and II shows that, while the chromospheric evaporation model plays a large part in stellar flares, it cannot explain all M-dwarf flare observations. Other heating mechanisms like thermal conduction are needed to explain the timing differences of quasi-Neupert flares and the existence of non-Neupert Type I flares, which do not show the *UVW2* response expected from nonthermal beam heating. In non-Neupert Type II flares, we find profiles that suggest both low-temperature heating and either low ambient densities or highly accelerated particles as origins, but further work using radio data is needed to draw conclusions. Last, the *U*-band and X-ray FFDs imply that the canonical energy partition may apply to an average of flares rather than individual ones, so caution should be used when extrapolating flare energies from only one wavelength regime. The X-ray energies will be refined with the analysis of the RGS spectra, and the number flares is still low and should be supplemented through future campaigns.

In future work, we will add in the radio data from the JVLA and the Australia Telescope Compact Array (ATCA) to perform the same type of analysis on the nonthermal ENE, which does not rely on a proxy for the radio/HXR response. This will allow us to better constrain the processes of the flares found in this study. X-ray spectral analysis will also assess flare temperature evolution to further study the TNE through chromospheric evaporation and condensation modeling.

Acknowledgments

We acknowledge and thank Dr. Wei-Chun Jao for assistance with scheduling CHIRON observations and for guidance on CTIO 0.9 m data reduction, Dr. Glenn H. Schneider for helpful discussions about young stars and AU Mic, and Dr. Joel C. Allred for helpful discussions about flare heating models that contributed to the observing proposal. I.I.T. thanks Dr. Meredith A. MacGregor and Dr. Allison Youngblood for discussion on stellar flare analysis. We also thank an anonymous referee for comments that helped to clarify results and improve the manuscript.

This work was supported by NASA ADAP award program No. 80NSSC21K0632, NASA XMM-Newton Guest Observer AO-17 Award No. 80NSSC19K0665, and the Space Telescope Science Institute's Director's Discretionary Research Fund 52079.

I.I.T. acknowledges support from the NSF Graduate Research Fellowship Program (GRFP). J.E.N. was supported by the Independent Research/Development program for program officers at the National Science Foundation. Any findings and conclusions are those of the author(s) and do not necessarily reflect the views of the National Science Foundation.

Y.N. was supported by the Japan Society for the Promotion of Science (JSPS) KAKENHI grant No. 21J00106, JSPS Overseas Research Fellowship Program, and JSPS Postdoctoral Research Fellowship Program.

We also acknowledge the International Space Science Institute and the supported International Teams 464: The Role Of Solar And Stellar Energetic Particles On (Exo) Planetary Habitability (ETERNAL, http://www.issibern.ch/teams/exoeternal/) and 510: Solar Extreme Events: Setting Up a Paradigm (SEESUP, https://www.issibern.ch/teams/solextremevent/).

This work is based on observations obtained with XMM-Newton, an ESA science mission with instruments and contributions directly funded by ESA Member States and NASA.

This work makes use of observations from the Las Cumbres Observatory global telescope network.

This research has used data from the SMARTS 1.5 m and 0.9 m telescopes, which are operated as part of the SMARTS Consortium.

This research has made use of the Spanish Virtual Observatory (http://svo.cab.inta-csic.es) project funded by MCIN/AEI/10.13039/501100011033/ through grant No. PID2020-112949GB-I00.

Appendix A
Calibration of the Quiescent Flux of AU Mic in *U*, *V*, and *UVW2*

A.1. OM/UVW2

Following the SAS calibration tables,[23] count rates from XMM OM *UVW2* are multiplied by 5.71×10^{-15} to convert to the flux at Earth (erg cm^{-2} s^{-1} Å^{-1}). This conversion was

[23] https://www.cosmos.esa.int/web/xmm-newton/sas-watchout-uvflux

determined for white dwarf standard stars, which is accurate to 10%. We confirm that this calibration is reasonable for AU Mic by integrating the HST/FOS spectrum of AU Mic over the *UVW2* effective area curve (Equation (2)), giving a quiescent flux of $1.14-1.18\times10^{-14}$ erg cm^{-2} s^{-1} Å^{-1}, which is consistent with the adopted value of 1.03×10^{-14} erg cm^{-2} s^{-1} Å^{-1} that is calculated from the SAS count-rate conversion. The mean wavelength of *UVW2* is ≈2150 Å and the FWHM is 475 Å, giving a quiescent XMM OM *UVW2* luminosity of 5.5×10^{28} erg s^{-1}. For reference, the Swift UVOT *W2* quiescent flux that we calculate from the quiescent AU Mic spectrum is 2.1×10^{-14} erg cm^{-2} s^{-1} Å^{-1} . Compared to the XMM OM *UVW2*, Swift *W2* has a factor of 8 larger peak effective area, a shorter mean wavelength, but a more pronounced red tail ("leak") that results in larger bandpass-weighted fluxes for very red stars during quiescence.

A.2. U *Band*

The apparent *U*-band magnitude of AU Mic is estimated in several ways. First, we use the (Johnson) $U-B$ color of 1.11 that was reported in Leggett (1992) from a compilation of measurements in The et al. (1984) and Celis (1986). This color is consistent with the colors that have been reported more recently (Cutispoto & Leto 1997; Cutispoto et al. 2003a, 2003b). Given a *B*-band magnitude of 10.26 from Leggett (1992) and Reid et al. (2004), and the Johnson *U*-band zero point of 4.3×10^{-9} erg cm^{-2} s^{-1} Å^{-1} from Willmer (2018), an estimated quiescent *U*-band magnitude is thus 11.37, which corresponds to a flux of 1.22×10^{-13} erg cm^{-2} s^{-1} Å^{-1}. Second, we compare the quiescent count rate of AU Mic to the comparison A9V star HD 197673, obtaining a count-rate ratio of 0.126 in quiescence. We estimate the Johnson *U*-band magnitude of this star to be 9.0 using representative colors[24] from Ducati et al. (2001) and the transformations from its measured Tycho-2 B_T and V_T magnitudes.[25] This gives a quiescent *U*-band magnitude of 11.22 and a flux of 1.4×10^{-13} erg cm^{-2} s^{-1} Å^{-1} for AU Mic. Third, we integrate over the HST/FOS spectrum of AU Mic with the LCO *U*-band transmission curve, which is nearly identical to the standard Bessel *U* filter from Bessell & Murphy (2012), obtaining a quiescent flux of 1.35×10^{-13} erg cm^{-2} s^{-1} Å^{-1} above the atmosphere and 1.41×10^{-13} erg cm^{-2} s^{-1} Å^{-1} at a representative air mass of sec $z=1.35$. We thus adopt a value of $1.3\pm0.1\times10^{-13}$ erg cm^{-2} s^{-1} Å^{-1} as the quiescent *U*-band flux of AU Mic. Using the distance of 9.72 pc from Gaia DR2 (Gaia Collaboration et al. 2016, 2018), this flux corresponds to a quiescent luminosity of $L_U\sim10^{30}$ erg s^{-1} for a filter FWHM of 700 Å.

A.3. V *Band*

There is a significant variation of single-epoch, *V*-band magnitudes ranging from 8.6 to 8.8 for AU Mic in the literature, which is likely in part due to the intrinsic rotational flux modulation (Cutispoto et al. 2003a, 2003b, 2001; Hebb et al. 2007; Ibañez Bustos et al. 2019); see also the peak-to-trough white-light variation in Transiting Exoplanet Survey Satellite data (Wisniewski et al. 2019). There is also a range of $V-I_C$ colors from 2.00 to 2.09 in the literature (Cutispoto et al. 2001; Winters et al. 2015; Leggett 1992); some of this variation may be due to color changes due to rotational modulation, as well (Cutispoto et al. 2001; Hebb et al. 2007). Most recently, Winters et al. (2015) find that $V=8.65$, which is consistent with the All Sky Automatic Survey value of 8.63 ± 0.04 (Pojmanski & Maciejewski 2005; Kiraga 2012; and see Discussion and Figures 3 and 4 of Ibañez Bustos et al. 2019). Reid et al. (2004)[26] quote *BVR* magnitudes of AU Mic that are systematically fainter: their value of $V=8.81$ comes from Leggett (1992), who compiled Johnson photometry from Celis (1986). A fainter magnitude is also quoted in the Hipparcos catalog, with $V_J=8.8$ (Perryman et al. 1997; Anderson & Francis 2012), and variation of H_p from 8.71 to 8.82 is notable over the 70 observations in Hipparcos (ESA 1997a, 1997b). A value of $V=8.65$ (Winters et al. 2015) is consistent with the Gaia DR2 (Gaia Collaboration et al. 2016, 2018) magnitude that is transformed[27] to *V*. We thus take a conservative range of *V*-band magnitudes for the systematic uncertainty in the quiescent flux of AU Mic. Using the zero points from Willmer (2018), we calculate the quiescent flux at Earth in the *V* band of AU Mic to be $1.1–1.33\times10^{-12}$ erg cm^{-2} s^{-1} Å^{-1} for a magnitude range of 8.6 to 8.8. Integrating the HST/FOS spectrum of AU Mic over the SMARTS/CTIO *V*-band transmission curve gives 1.22×10^{-12} erg cm^{-2} s^{-1} Å^{-1} in the middle of these estimates. We thus adopt $1.2\pm0.1\times10^{-12}$ erg cm^{-2} s^{-1} Å^{-1} as the quiescent flux[28] of AU Mic in the Bessel *V* band, giving $L_V=1.2\times10^{31}$ erg s^{-1} through a filter with a FWHM of 850 Å.

A comparison of the LCO *V*-band, SMARTS *V*-band, and the standard Bessell & Murphy (2012) *V*-band transmission curves is shown in Figure 1. The LCO *V* band is slightly bluer than the SMARTS *V* band and the standard Bessel *V* band. We integrate the AU Mic HST/FOS spectrum and find that the filter-weighted[29] flux density (Sirianni et al. 2005; see also Bessell & Murphy 2012) in the LCO *V* band is lowest by 10%, while the other two synthesized *V*-band fluxes are within 1% of each other. We test this against the dM1e template spectrum from Bochanski et al. (2007) as well. Note that the (intractable) sensitivity differences between the CCDs and telescope optics are not accounted for in this comparison.

Appendix B
Flare Quantities

We provide durations, rise times, peak rates, and total energies, along with start, end, and peak times for each flare in Table 6.

[24] Compiled on the website at https://www.stsci.edu/~inr/intrins.html.

[25] http://vizier.cfa.harvard.edu/ftp/cats/I/239/version_cd/docs/vol1/sect1_03.pdf

[26] http://www.stsci.edu/~inr/phot/allphotpi.sing.2mass

[27] https://gea.esac.esa.int/archive/documentation/GDR2/Data_processing/chap_cu5pho/sec_cu5pho_calibr/ssec_cu5pho_PhotTransf.html

[28] This is consistent with the range of the fluxes quoted in the Simbad photometry viewer tool: http://vizier.unistra.fr/vizier/sed/.

[29] We assume that all filter transmission curves are provided as appropriate for photon-counting CCDs; many filter curve files in the Spanish Virtual Observatory database are listed as "energy counting" for historical reasons only and are intended to be corrected as appropriate in future updates (C. Rodrigo 2019, private communication).

Table 6
Common Flare Properties

ID	Obs.	Band	$t_{\rm Total}$ (minute)	$t_{\rm Rise}$ (minute)	Peak Rate [a]	Energy (erg)	Start Time (UTC)	End Time (UTC)	Peak Time (UTC)
1	OM	*UVW2*	6.83	2.17	3.67	$(1.8 \pm 0.1) \times 10^{31}$	2018-10-10T13:28:09.760	2018-10-10T13:34:59.760	2018-10-10T13:30:19.760
	EPIC-pn	X-ray	33.00	10.33	6.68	$(10.0 \pm 2.2) \times 10^{31}$	2018-10-10T13:29:17.030	2018-10-10T14:02:17.030	2018-10-10T13:39:37.030
	EPIC-pn	X-ray Der.	…	…	…	…	…	2018-10-10T13:34:57.030	2018-10-10T13:30:07.030
	RGS	X-ray	33.00	21.50	0.59	…	2018-10-10T13:29:18.868	2018-10-10T14:02:18.868	2018-10-10T13:50:48.868
2	EPIC-pn	X-ray	143.83	30.50	8.05	$(2.1 \pm 0.5) \times 10^{32}$	2018-10-10T14:24:07.030	2018-10-10T16:47:57.030	2018-10-10T14:54:37.030
	EPIC-pn	X-ray Der.	…	…	…	…	…	2018-10-10T14:59:57.030	2018-10-10T14:43:37.030
3	OM	*UVW2*	3.50	0.83	2.38	$(8.9 \pm 0.4) \times 10^{30}$	2018-10-10T18:49:16.656	2018-10-10T18:52:46.656	2018-10-10T18:50:06.656
	LCOGT	*U*	5.37	3.82	0.11	$(2.1 \pm 0.1) \times 10^{31}$	2018-10-10T18:47:58.000	2018-10-10T18:53:20.000	2018-10-10T18:51:47.000
4	EPIC-pn	X-ray	57.50	11.50	4.97	$(7.3 \pm 1.6) \times 10^{31}$	2018-10-10T19:55:17.030	2018-10-10T20:52:47.030	2018-10-10T20:06:47.030
	EPIC-pn	X-ray Der.	…	…	…	…	…	2018-10-10T20:23:57.030	2018-10-10T19:57:17.030
5	OM	*UVW2*	1.67	1.00	4.89	$(5.9 \pm 0.3) \times 10^{30}$	2018-10-10T21:50:40.525	2018-10-10T21:52:20.525	2018-10-10T21:51:40.525
	EPIC-pn	X-ray	35.83	18.17	7.17	$(7.6 \pm 1.7) \times 10^{31}$	2018-10-10T21:46:07.030	2018-10-10T22:21:57.030	2018-10-10T22:04:17.030
	EPIC-pn	X-ray Der.	…	…	…	…	…	2018-10-10T22:04:47.030	2018-10-10T21:54:57.030
6	OM	*UVW2*	1.00	0.67	1.94	$(2.3 \pm 0.3) \times 10^{30}$	2018-10-10T22:01:30.525	2018-10-10T22:02:30.525	2018-10-10T22:02:10.525
7	OM	*UVW2*	3.00	0.50	3.13	$(7.6 \pm 0.4) \times 10^{30}$	2018-10-11T00:15:54.389	2018-10-11T00:18:54.389	2018-10-11T00:16:24.389
8	OM	*UVW2*	3.17	0.67	24.70	$(3.5 \pm 0.0) \times 10^{31}$	2018-10-11T08:39:07.720	2018-10-11T08:42:17.720	2018-10-11T08:39:47.720
	EPIC-pn	X-ray	9.17	3.67	8.35	$(2.5 \pm 0.6) \times 10^{31}$	2018-10-11T08:39:57.030	2018-10-11T08:49:07.030	2018-10-11T08:43:37.030
	EPIC-pn	X-ray Der.	…	…	…	…	…	2018-10-11T08:51:17.030	2018-10-11T08:40:17.030
	RGS	X-ray	8.50	2.00	0.84	…	2018-10-11T08:40:18.868	2018-10-11T08:48:48.868	2018-10-11T08:42:18.868
9	OM	*UVW2*	4.67	2.50	7.85	$(2.3 \pm 0.0) \times 10^{31}$	2018-10-11T14:03:56.240	2018-10-11T14:08:36.240	2018-10-11T14:06:26.240
10	OM	*UVW2*	0.50	0.17	2.72	$(1.8 \pm 0.2) \times 10^{30}$	2018-10-11T14:11:36.240	2018-10-11T14:12:06.240	2018-10-11T14:11:46.240
11	EPIC-pn	X-ray	482.33	331.50	18.70	$(2.8 \pm 0.6) \times 10^{33}$	2018-10-11T14:02:27.030	2018-10-11T22:04:47.030	2018-10-11T19:33:57.030
	EPIC-pn	X-ray Der.	…	…	…	…	…	2018-10-11T19:11:57.030	2018-10-11T17:16:27.030
	RGS	X-ray	481.50	328.50	1.15	…	2018-10-11T14:02:48.868	2018-10-11T22:04:18.868	2018-10-11T19:31:18.868
12	OM	*UVW2*	2.67	0.50	11.90	$(2.7 \pm 0.0) \times 10^{31}$	2018-10-11T17:14:00.205	2018-10-11T17:16:40.205	2018-10-11T17:14:30.205
13	OM	*UVW2*	1.33	0.83	4.95	$(4.8 \pm 0.3) \times 10^{30}$	2018-10-11T18:25:17.162	2018-10-11T18:26:37.162	2018-10-11T18:26:07.162
14	OM	*UVW2*	3.33	0.17	3.55	$(6.1 \pm 0.5) \times 10^{30}$	2018-10-11T19:31:53.637	2018-10-11T19:35:13.637	2018-10-11T19:32:03.637
15	OM	*UVW2*	110.93	54.63	6.99	$(5.0 \pm 0.4) \times 10^{32}$	2018-10-11T23:51:23.346	2018-10-12T01:42:19.177	2018-10-12T00:46:01.280
	EPIC-pn	X-ray	123.17	90.17	36.57	$(2.5 \pm 0.5) \times 10^{33}$	2018-10-11T23:51:27.030	2018-10-12T01:54:37.030	2018-10-12T01:21:37.030
	EPIC-pn	X-ray Der.	…	…	…	…	…	2018-10-12T01:52:27.030	2018-10-12T00:55:57.030
	RGS	X-ray	127.39	85.00	1.83	…	2018-10-11T23:51:48.868	2018-10-12T01:59:12.093	2018-10-12T01:16:48.868
16	OM	*UVW2*	1.83	1.17	2.51	$(3.2 \pm 0.3) \times 10^{30}$	2018-10-12T14:43:20.711	2018-10-12T14:45:10.711	2018-10-12T14:44:30.711
	EPIC-pn	X-ray	43.00	24.67	4.92	$(4.4 \pm 1.0) \times 10^{31}$	2018-10-12T14:38:33.020	2018-10-12T15:21:33.020	2018-10-12T15:03:13.020
	EPIC-pn	X-ray Der.	…	…	…	…	…	2018-10-12T15:07:03.020	2018-10-12T14:45:43.020
17	EPIC-pn	X-ray	57.33	38.00	7.80	$(1.6 \pm 0.3) \times 10^{32}$	2018-10-12T16:26:33.020	2018-10-12T17:23:53.020	2018-10-12T17:04:33.020
	EPIC-pn	X-ray Der.	…	…	…	…	…	2018-10-12T16:55:03.020	2018-10-12T16:31:53.020
18	OM	*UVW2*	9.67	0.67	3.77	$(1.7 \pm 0.1) \times 10^{31}$	2018-10-12T17:23:26.626	2018-10-12T17:33:06.626	2018-10-12T17:24:06.626
	EPIC-pn	X-ray	35.83	9.17	8.32	$(9.3 \pm 2.0) \times 10^{31}$	2018-10-12T17:24:03.020	2018-10-12T17:59:53.020	2018-10-12T17:33:13.020
	EPIC-pn	X-ray Der.	…	…	…	…	…	2018-10-12T17:38:23.020	2018-10-12T17:31:03.020
19	OM	*UVW2*	2.33	1.83	2.67	$(4.3 \pm 0.4) \times 10^{30}$	2018-10-12T19:43:59.035	2018-10-12T19:46:19.035	2018-10-12T19:45:49.035
20	OM	*UVW2*	17.83	0.83	2.38	$(2.8 \pm 0.1) \times 10^{31}$	2018-10-12T20:11:09.035	2018-10-12T20:28:59.035	2018-10-12T20:11:59.035
	EPIC-pn	X-ray	201.33	15.33	8.09	$(4.6 \pm 1.0) \times 10^{32}$	2018-10-12T20:09:43.020	2018-10-12T23:31:03.020	2018-10-12T20:25:03.020
	EPIC-pn	X-ray Der.	…	…	…	…	…	2018-10-12T20:23:53.020	2018-10-12T20:18:03.020
21	OM	*UVW2*	1.67	0.50	8.82	$(7.1 \pm 0.3) \times 10^{30}$	2018-10-13T00:18:00.903	2018-10-13T00:19:40.903	2018-10-13T00:18:30.903
	EPIC-pn	X-ray	64.67	13.50	11.60	$(2.4 \pm 0.5) \times 10^{32}$	2018-10-13T00:21:43.020	2018-10-13T01:26:23.020	2018-10-13T00:35:13.020
	EPIC-pn	X-ray Der.	…	…	…	…	…	2018-10-13T00:35:53.020	2018-10-13T00:26:33.020
	LCOGT	*U*	47.98	5.33	0.12	$(1.1 \pm 0.0) \times 10^{32}$	2018-10-13T00:15:01.000	2018-10-13T01:03:00.000	2018-10-13T00:20:21.000

Table 6
(Continued)

ID	Obs.	Band	$t_{\rm Total}$ (minute)	$t_{\rm Rise}$ (minute)	Peak Rate [a]	Energy (erg)	Start Time (UTC)	End Time (UTC)	Peak Time (UTC)
22	OM	*UVW2*	9.67	5.17	36.47	$(1.2 \pm 0.0) \times 10^{32}$	2018-10-13T01:38:26.759	2018-10-13T01:48:06.759	2018-10-13T01:43:36.759
	EPIC-pn	X-ray	46.67	19.33	11.50	$(1.9 \pm 0.4) \times 10^{32}$	2018-10-13T01:37:13.020	2018-10-13T02:23:53.020	2018-10-13T01:56:33.020
	EPIC-pn	X-ray Der.	⋯	⋯	⋯	⋯	⋯	2018-10-13T02:09:33.020	2018-10-13T01:43:23.020
	RGS	X-ray	60.80	19.20	0.63	⋯	2018-10-13T01:37:13.491	2018-10-13T02:38:01.491	2018-10-13T01:56:25.491
	LCOGT	*U*	48.12	8.33	0.71	$(2.6 \pm 0.0) \times 10^{32}$	2018-10-13T01:35:41.000	2018-10-13T02:23:48.000	2018-10-13T01:44:01.000
	2KCCD	*V*	13.12	6.09	0.06	$(2.0 \pm 0.1) \times 10^{32}$	2018-10-13T01:37:29.285	2018-10-13T01:50:36.263	2018-10-13T01:43:34.439
	CHIRON	Hα	51.29	6.45	0.95	⋯	2018-10-13T01:37:45.300	2018-10-13T02:29:02.800	2018-10-13T01:44:12.100
23	OM	*UVW2*	40.78	8.50	101.39	$(9.7 \pm 0.3) \times 10^{32}$	2018-10-13T03:11:14.735	2018-10-13T03:52:01.749	2018-10-13T03:19:44.735
	EPIC-pn	X-ray	61.67	9.83	55.61	$(9.6 \pm 2.1) \times 10^{32}$	2018-10-13T03:17:23.020	2018-10-13T04:19:03.020	2018-10-13T03:27:13.020
	EPIC-pn	X-ray Der.	⋯	⋯	⋯	⋯	⋯	2018-10-13T04:04:43.020	2018-10-13T03:21:03.020
	RGS	X-ray	61.33	10.13	2.31	⋯	2018-10-13T03:17:29.491	2018-10-13T04:18:49.491	2018-10-13T03:27:37.491
	LCOGT	*U*	68.28	27.67	2.42	$(1.6 \pm 0.0) \times 10^{33}$	2018-10-13T02:53:02.000	2018-10-13T04:01:19.000	2018-10-13T03:20:42.000
	LCOGT	*V*	17.46	4.98	0.16	$(9.5 \pm 0.1) \times 10^{32}$	2018-10-13T03:18:13.367	2018-10-13T03:35:40.717	2018-10-13T03:23:12.377
	2KCCD	*V*	25.44	5.33	0.13	$(9.8 \pm 0.1) \times 10^{32}$	2018-10-13T03:17:03.017	2018-10-13T03:42:29.470	2018-10-13T03:22:22.524
	CHIRON	Hα	75.86	24.89	2.34	⋯	2018-10-13T02:57:26.600	2018-10-13T04:13:18.500	2018-10-13T03:22:19.800
24	OM	*UVW2*	29.13	11.96	4.81	$(1.5 \pm 0.3) \times 10^{32}$	2018-10-13T07:16:25.715	2018-10-13T07:45:33.505	2018-10-13T07:28:23.505
	EPIC-pn	X-ray	100.67	53.67	17.65	$(5.0 \pm 1.1) \times 10^{32}$	2018-10-13T06:43:13.020	2018-10-13T08:23:53.020	2018-10-13T07:36:53.020
	EPIC-pn	X-ray Der.	⋯	⋯	⋯	⋯	⋯	2018-10-13T08:09:33.020	2018-10-13T07:26:53.020
	RGS	X-ray	100.27	51.73	1.05	⋯	2018-10-13T06:43:21.491	2018-10-13T08:23:37.491	2018-10-13T07:35:05.491
25	OM	*UVW2*	2.67	0.83	11.47	$(2.1 \pm 0.0) \times 10^{31}$	2018-10-13T10:21:36.573	2018-10-13T10:24:16.573	2018-10-13T10:22:26.573
	EPIC-pn	X-ray	30.00	23.83	9.87	$(1.2 \pm 0.3) \times 10^{32}$	2018-10-13T10:20:43.020	2018-10-13T10:50:43.020	2018-10-13T10:44:33.020
	EPIC-pn	X-ray Der.	⋯	⋯	⋯	⋯	⋯	2018-10-13T10:40:43.020	2018-10-13T10:25:23.020
26	OM	*UVW2*	3.83	1.33	5.05	$(1.2 \pm 0.0) \times 10^{31}$	2018-10-13T12:46:52.338	2018-10-13T12:50:42.338	2018-10-13T12:48:12.338
	LCOGT	*U*	11.06	2.38	0.13	$(1.5 \pm 0.1) \times 10^{31}$	2018-10-13T12:46:12.237	2018-10-13T12:57:16.096	2018-10-13T12:48:35.081
27	OM	*UVW2*	17.33	4.00	21.62	$(1.0 \pm 0.0) \times 10^{32}$	2018-10-13T13:59:27.286	2018-10-13T14:16:47.286	2018-10-13T14:03:27.286
	EPIC-pn	X-ray	48.83	9.17	14.71	$(3.1 \pm 0.7) \times 10^{32}$	2018-10-13T13:59:33.020	2018-10-13T14:48:23.020	2018-10-13T14:08:43.020
	EPIC-pn	X-ray Der.	⋯	⋯	⋯	⋯	⋯	2018-10-13T14:23:53.020	2018-10-13T14:03:33.020
	RGS	X-ray	48.53	11.20	0.94	⋯	2018-10-13T13:59:37.491	2018-10-13T14:48:09.491	2018-10-13T14:10:49.491
28	OM	*UVW2*	5.67	2.00	5.74	$(1.9 \pm 0.1) \times 10^{31}$	2018-10-13T17:54:17.130	2018-10-13T17:59:57.130	2018-10-13T17:56:17.130
	EPIC-pn	X-ray	195.67	28.17	8.36	$(5.7 \pm 1.3) \times 10^{32}$	2018-10-13T17:51:23.020	2018-10-13T21:07:03.020	2018-10-13T18:19:33.020
	EPIC-pn	X-ray Der.	⋯	⋯	⋯	⋯	⋯	2018-10-13T18:28:43.020	2018-10-13T17:55:43.020
29	OM	*UVW2*	4.50	3.00	2.29	$(7.3 \pm 0.5) \times 10^{30}$	2018-10-13T19:16:04.636	2018-10-13T19:20:34.636	2018-10-13T19:19:04.636
30	EPIC-pn	X-ray	86.33	17.17	5.70	$(1.9 \pm 0.4) \times 10^{32}$	2018-10-13T21:07:13.020	2018-10-13T22:33:33.020	2018-10-13T21:24:23.020
	EPIC-pn	X-ray Der.	⋯	⋯	⋯	⋯	⋯	2018-10-13T21:50:23.020	2018-10-13T21:39:03.020
31	OM	*UVW2*	2.33	0.67	3.22	$(3.6 \pm 0.3) \times 10^{30}$	2018-10-13T23:20:26.268	2018-10-13T23:22:46.268	2018-10-13T23:21:06.268
32	EPIC-pn	X-ray	100.67	54.50	6.04	$(1.0 \pm 0.2) \times 10^{32}$	2018-10-13T23:16:53.020	2018-10-14T00:57:33.020	2018-10-14T00:11:23.020
	EPIC-pn	X-ray Der.	⋯	⋯	⋯	⋯	⋯	2018-10-14T00:14:23.020	2018-10-14T00:10:03.020
33	LCOGT	*U*	17.45	6.08	0.05	$(2.2 \pm 0.1) \times 10^{31}$	2018-10-13T23:53:16.000	2018-10-14T00:10:43.000	2018-10-13T23:59:21.000
34	EPIC-pn	X-ray	180.17	83.83	10.34	$(5.9 \pm 1.3) \times 10^{32}$	2018-10-14T12:21:16.970	2018-10-14T15:21:26.970	2018-10-14T13:45:06.970
	EPIC-pn	X-ray Der.	⋯	⋯	⋯	⋯	⋯	2018-10-14T13:55:06.970	2018-10-14T12:23:16.970
	RGS	X-ray	214.80	97.20	0.67	⋯	2018-10-14T12:15:11.942	2018-10-14T15:49:59.942	2018-10-14T13:52:23.942
35	EPIC-pn	X-ray	35.83	8.83	21.00	$(2.6 \pm 0.6) \times 10^{32}$	2018-10-15T01:12:06.970	2018-10-15T01:47:56.970	2018-10-15T01:20:56.970
	EPIC-pn	X-ray Der.	⋯	⋯	⋯	⋯	⋯	2018-10-15T01:26:16.970	2018-10-15T01:16:56.970
	RGS	X-ray	42.60	12.60	0.91	⋯	2018-10-15T01:12:11.942	2018-10-15T01:54:47.942	2018-10-15T01:24:47.942
	LCOGT	*U*	29.73	6.22	0.67	$(2.8 \pm 0.0) \times 10^{32}$	2018-10-15T01:12:14.000	2018-10-15T01:41:58.000	2018-10-15T01:18:27.000
	LCOGT	*V*	11.53	4.15	0.05	$(1.4 \pm 0.1) \times 10^{32}$	2018-10-15T01:14:19.067	2018-10-15T01:25:50.656	2018-10-15T01:18:28.089
	2KCCD	*V*	16.14	3.80	0.04	$(1.6 \pm 0.1) \times 10^{32}$	2018-10-15T01:14:12.956	2018-10-15T01:30:21.269	2018-10-15T01:18:01.184

Table 6
(Continued)

ID	Obs.	Band	$t_{\rm Total}$ (minute)	$t_{\rm Rise}$ (minute)	Peak Rate [a]	Energy (erg)	Start Time (UTC)	End Time (UTC)	Peak Time (UTC)
	CHIRON	Hα	48.60	9.67	0.57	⋯	2018-10-15T01:10:11.100	2018-10-15T01:58:47.300	2018-10-15T01:19:51.400
36	EPIC-pn	X-ray	35.83	13.17	10.17	$(1.5 \pm 0.3) \times 10^{32}$	2018-10-15T03:14:26.970	2018-10-15T03:50:16.970	2018-10-15T03:27:36.970
	EPIC-pn	X-ray Der.	⋯	⋯	⋯	⋯	⋯	2018-10-15T03:21:26.970	2018-10-15T03:17:36.970
	RGS	X-ray	49.80	12.60	0.80	⋯	2018-10-15T03:14:35.942	2018-10-15T04:04:23.942	2018-10-15T03:27:11.942
	LCOGT	*U*	8.35	2.27	0.21	$(4.0 \pm 0.1) \times 10^{31}$	2018-10-15T03:15:24.000	2018-10-15T03:23:45.000	2018-10-15T03:17:40.000
	CHIRON	Hα	83.40	34.56	0.32	⋯	2018-10-15T02:54:43.400	2018-10-15T04:18:07.500	2018-10-15T03:29:17.100
37	EPIC-pn	X-ray	151.00	13.83	12.58	$(5.8 \pm 1.3) \times 10^{32}$	2018-10-15T07:04:56.970	2018-10-15T09:35:56.970	2018-10-15T07:18:46.970
	EPIC-pn	X-ray Der.	⋯	⋯	⋯	⋯	⋯	2018-10-15T07:47:56.970	2018-10-15T07:13:06.970
38	EPIC-pn	X-ray	21.33	10.33	5.90	$(3.8 \pm 0.8) \times 10^{31}$	2018-10-15T10:04:56.970	2018-10-15T10:26:16.970	2018-10-15T10:15:16.970
	EPIC-pn	X-ray Der.	⋯	⋯	⋯	⋯	⋯	2018-10-15T10:19:06.970	2018-10-15T10:08:26.970
	LCOGT	*U*	9.50	3.14	0.14	$(2.3 \pm 0.1) \times 10^{31}$	2018-10-15T10:02:13.657	2018-10-15T10:11:43.485	2018-10-15T10:05:22.281
39	EPIC-pn	X-ray	71.83	12.17	5.76	$(8.4 \pm 1.8) \times 10^{31}$	2018-10-15T14:24:06.970	2018-10-15T15:35:56.970	2018-10-15T14:36:16.970
	EPIC-pn	X-ray Der.	⋯	⋯	⋯	⋯	⋯	2018-10-15T15:07:06.970	2018-10-15T14:35:46.970
40	EPIC-pn	X-ray	28.67	14.33	7.27	$(6.8 \pm 1.5) \times 10^{31}$	2018-10-15T19:19:16.970	2018-10-15T19:47:56.970	2018-10-15T19:33:36.970
	EPIC-pn	X-ray Der.	⋯	⋯	⋯	⋯	⋯	2018-10-15T19:33:26.970	2018-10-15T19:26:26.970
	RGS	X-ray	28.20	10.80	0.51	⋯	2018-10-15T19:19:23.942	2018-10-15T19:47:35.942	2018-10-15T19:30:11.942
	LCOGT	*U*	16.49	1.56	0.16	$(9.0 \pm 0.7) \times 10^{31}$	2018-10-15T19:24:12.845	2018-10-15T19:40:42.003	2018-10-15T19:25:46.278
41	EPIC-pn	X-ray	35.83	12.17	4.07	$(2.6 \pm 0.6) \times 10^{31}$	2018-10-15T20:31:16.970	2018-10-15T21:07:06.970	2018-10-15T20:43:26.970
	EPIC-pn	X-ray Der.	⋯	⋯	⋯	⋯	⋯	2018-10-15T20:45:26.970	2018-10-15T20:39:36.970
42	EPIC-pn	X-ray	28.67	22.67	5.61	$(6.2 \pm 1.3) \times 10^{31}$	2018-10-15T21:07:16.970	2018-10-15T21:35:56.970	2018-10-15T21:29:56.970
	EPIC-pn	X-ray Der.	⋯	⋯	⋯	⋯	⋯	2018-10-15T21:21:26.970	2018-10-15T21:16:26.970
43	OM	*UVW2*	1.50	0.67	1.84	$(2.3 \pm 0.2) \times 10^{30}$	2018-10-15T22:02:43.412	2018-10-15T22:04:13.412	2018-10-15T22:03:23.412
	EPIC-pn	X-ray	23.67	9.83	6.10	$(3.9 \pm 0.8) \times 10^{31}$	2018-10-15T21:57:36.970	2018-10-15T22:21:16.970	2018-10-15T22:07:26.970
	EPIC-pn	X-ray Der.	⋯	⋯	⋯	⋯	⋯	2018-10-15T22:11:56.970	2018-10-15T22:03:36.970
44	EPIC-pn	X-ray	21.50	10.17	6.33	$(3.4 \pm 0.7) \times 10^{31}$	2018-10-16T01:33:36.970	2018-10-16T01:55:06.970	2018-10-16T01:43:46.970
	EPIC-pn	X-ray Der.	⋯	⋯	⋯	⋯	⋯	2018-10-16T01:47:56.970	2018-10-16T01:34:36.970
	CHIRON	Hα	35.63	2.15	0.18	⋯	2018-10-16T01:28:47.600	2018-10-16T02:04:25.400	2018-10-16T01:30:56.700
45	LCOGT	*U*	6.45	2.36	0.15	$(2.6 \pm 0.1) \times 10^{31}$	2018-10-16T19:41:28.237	2018-10-16T19:47:55.014	2018-10-16T19:43:49.791
46	OM	*UVW2*	2.67	1.17	1.80	$(3.6 \pm 0.4) \times 10^{30}$	2018-10-17T00:18:51.362	2018-10-17T00:21:31.362	2018-10-17T00:20:01.362
	EPIC-pn	X-ray	37.33	31.17	6.01	$(4.6 \pm 1.0) \times 10^{31}$	2018-10-17T00:20:09.980	2018-10-17T00:57:29.980	2018-10-17T00:51:19.980
	EPIC-pn	X-ray Der.	⋯	⋯	⋯	⋯	⋯	2018-10-17T00:43:09.980	2018-10-17T00:22:29.980
47	OM	*UVW2*	30.78	22.45	3.43	$(4.0 \pm 2.6) \times 10^{31}$	2018-10-17T01:57:28.367	2018-10-17T02:28:15.276	2018-10-17T02:19:55.276
	EPIC-pn	X-ray	129.50	44.00	8.67	$(3.2 \pm 0.7) \times 10^{32}$	2018-10-17T01:26:29.980	2018-10-17T03:35:59.980	2018-10-17T02:10:29.980
	EPIC-pn	X-ray Der.	⋯	⋯	⋯	⋯	⋯	2018-10-17T02:38:19.980	2018-10-17T02:20:09.980
	RGS	X-ray	129.15	59.85	0.92	⋯	2018-10-17T01:26:34.575	2018-10-17T03:35:43.575	2018-10-17T02:26:25.575
	2KCCD	*V*	17.66	4.56	0.02	$(1.4 \pm 0.1) \times 10^{32}$	2018-10-17T02:15:58.506	2018-10-17T02:33:37.951	2018-10-17T02:20:32.345
	CHIRON	Hα	128.67	60.41	0.30	⋯	2018-10-17T01:26:11.500	2018-10-17T03:34:51.800	2018-10-17T02:26:36.400
48	OM	*UVW2*	1.17	0.67	3.21	$(3.6 \pm 0.3) \times 10^{30}$	2018-10-17T04:07:23.271	2018-10-17T04:08:33.271	2018-10-17T04:08:03.271
	EPIC-pn	X-ray	23.00	12.67	6.06	$(2.2 \pm 0.5) \times 10^{31}$	2018-10-17T04:04:49.980	2018-10-17T04:27:49.980	2018-10-17T04:17:29.980
	EPIC-pn	X-ray Der.	⋯	⋯	⋯	⋯	⋯	2018-10-17T04:19:09.980	2018-10-17T04:09:29.980
49	EPIC-pn	X-ray	28.67	6.83	6.73	$(4.7 \pm 1.0) \times 10^{31}$	2018-10-17T05:45:39.980	2018-10-17T06:14:19.980	2018-10-17T05:52:29.980
	EPIC-pn	X-ray Der.	⋯	⋯	⋯	⋯	⋯	2018-10-17T05:59:59.980	2018-10-17T05:52:39.980
50	OM	*UVW2*	6.67	0.50	29.03	$(4.0 \pm 0.1) \times 10^{31}$	2018-10-17T08:01:34.494	2018-10-17T08:08:14.494	2018-10-17T08:02:04.494
	EPIC-pn	X-ray	35.83	8.00	10.35	$(1.6 \pm 0.3) \times 10^{32}$	2018-10-17T08:02:29.980	2018-10-17T08:38:19.980	2018-10-17T08:10:29.980
	EPIC-pn	X-ray Der.	⋯	⋯	⋯	⋯	⋯	2018-10-17T08:16:39.980	2018-10-17T08:04:39.980
51	OM	*UVW2*	5.67	2.50	12.88	$(3.2 \pm 0.1) \times 10^{31}$	2018-10-17T08:38:24.494	2018-10-17T08:44:04.494	2018-10-17T08:40:54.494

Table 6
(Continued)

ID	Obs.	Band	$t_{\rm Total}$ (minute)	$t_{\rm Rise}$ (minute)	Peak Rate [a]	Energy (erg)	Start Time (UTC)	End Time (UTC)	Peak Time (UTC)
	EPIC-pn	X-ray	28.67	9.00	13.13	$(1.6 \pm 0.3) \times 10^{32}$	2018-10-17T08:38:29.980	2018-10-17T09:07:09.980	2018-10-17T08:47:29.980
	EPIC-pn	X-ray Der.	⋯	⋯	⋯	⋯	⋯	2018-10-17T08:45:29.980	2018-10-17T08:40:59.980
	RGS	X-ray	28.35	10.80	0.75	⋯	2018-10-17T08:38:34.575	2018-10-17T09:06:55.575	2018-10-17T08:49:22.575
52	OM	*UVW2*	5.33	0.17	2.76	$(1.0 \pm 0.1) \times 10^{31}$	2018-10-17T14:47:19.184	2018-10-17T14:52:39.184	2018-10-17T14:47:29.184
	EPIC-pn	X-ray	12.00	5.33	6.99	$(4.0 \pm 0.9) \times 10^{31}$	2018-10-17T14:42:09.980	2018-10-17T14:54:09.980	2018-10-17T14:47:29.980
	EPIC-pn	X-ray Der.	⋯	⋯	⋯	⋯	⋯	2018-10-17T14:52:39.980	2018-10-17T14:45:09.980
	RGS	X-ray	21.15	15.30	0.69	⋯	2018-10-17T14:38:34.575	2018-10-17T14:59:43.575	2018-10-17T14:53:52.575
53	OM	*UVW2*	1.17	0.67	2.25	$(2.9 \pm 0.3) \times 10^{30}$	2018-10-17T15:54:59.184	2018-10-17T15:56:09.184	2018-10-17T15:55:39.184
54	LCOGT	*U*	44.10	4.55	0.06	$(4.9 \pm 0.3) \times 10^{31}$	2018-10-18T01:39:37.000	2018-10-18T02:23:43.000	2018-10-18T01:44:10.000
	CHIRON	Hα	103.89	30.33	0.26	⋯	2018-10-18T01:23:38.400	2018-10-18T03:07:32.100	2018-10-18T01:53:58.300
55	CHIRON	Hα	54.25	34.73	0.24	⋯	2018-10-19T01:11:40.600	2018-10-19T02:05:55.900	2018-10-19T01:46:24.500
56	CHIRON	Hα	47.69	16.28	0.24	⋯	2018-10-19T03:18:31.000	2018-10-19T04:06:12.600	2018-10-19T03:34:47.600
57	LCOGT	*U*	31.22	19.87	0.06	$(3.3 \pm 0.1) \times 10^{31}$	2018-10-21T00:37:12.000	2018-10-21T01:08:25.000	2018-10-21T00:57:04.000
	CHIRON	Hα	36.93	26.09	0.36	⋯	2018-10-21T00:37:55.600	2018-10-21T01:14:51.700	2018-10-21T01:04:01.000
58	LCOGT	*U*	14.12	3.02	0.14	$(3.0 \pm 0.2) \times 10^{31}$	2018-10-21T03:07:20.000	2018-10-21T03:21:27.000	2018-10-21T03:10:21.000
	CHIRON	Hα	15.23	10.86	0.25	⋯	2018-10-21T03:09:32.800	2018-10-21T03:24:46.500	2018-10-21T03:20:24.500
59	LCOGT	*U*	30.42	11.35	0.06	$(4.0 \pm 0.3) \times 10^{31}$	2018-10-22T01:25:40.000	2018-10-22T01:56:05.000	2018-10-22T01:37:01.000
60	LCOGT	*U*	16.67	1.52	0.13	$(4.6 \pm 0.2) \times 10^{31}$	2018-10-22T01:56:50.000	2018-10-22T02:13:30.000	2018-10-22T01:58:21.000
61	LCOGT	*U*	12.87	7.58	0.18	$(5.8 \pm 0.2) \times 10^{31}$	2018-10-22T02:28:16.000	2018-10-22T02:41:08.000	2018-10-22T02:35:51.000
	CHIRON	Hα	184.25	70.38	0.79	⋯	2018-10-22T01:27:13.600	2018-10-22T04:31:28.800	2018-10-22T02:37:36.400
62	LCOGT	*U*	29.03	4.55	0.08	$(4.9 \pm 0.2) \times 10^{31}$	2018-10-22T23:57:44.000	2018-10-23T00:26:46.000	2018-10-23T00:02:17.000
	CHIRON	Hα	39.04	22.74	0.34	⋯	2018-10-22T23:57:18.500	2018-10-23T00:36:21.200	2018-10-23T00:20:03.200
63	CHIRON	Hα	48.04	17.73	0.20	⋯	2018-10-23T01:05:30.800	2018-10-23T01:53:33.400	2018-10-23T01:23:14.400
64	CHIRON	Hα	40.08	13.00	0.20	⋯	2018-10-23T03:33:08.300	2018-10-23T04:13:13.300	2018-10-23T03:46:08.500
65	CHIRON	Hα	173.43	43.46	2.48	⋯	2018-10-24T00:28:16.900	2018-10-24T03:21:42.900	2018-10-24T01:11:44.500
66	CHIRON	Hα	24.96	13.06	0.12	⋯	2018-10-25T01:57:31.000	2018-10-25T02:22:28.400	2018-10-25T02:10:34.900
67	LCOGT	*U*	29.82	11.33	0.07	$(3.0 \pm 0.1) \times 10^{31}$	2018-10-26T00:56:19.000	2018-10-26T01:26:08.000	2018-10-26T01:07:39.000
68	LCOGT	*U*	36.73	17.05	0.07	$(6.9 \pm 0.2) \times 10^{31}$	2018-10-26T02:31:21.000	2018-10-26T03:08:05.000	2018-10-26T02:48:24.000
69	LCOGT	*U*	9.49	1.58	0.12	$(2.6 \pm 0.1) \times 10^{31}$	2018-10-26T12:25:42.500	2018-10-26T12:35:11.717	2018-10-26T12:27:17.331
70	LCOGT	*U*	6.30	1.57	0.08	$(9.0 \pm 0.8) \times 10^{30}$	2018-10-29T11:24:31.511	2018-10-29T11:30:49.366	2018-10-29T11:26:05.555
71	LCOGT	*U*	8.65	4.72	0.07	$(2.1 \pm 0.1) \times 10^{31}$	2018-10-29T12:23:17.353	2018-10-29T12:31:56.114	2018-10-29T12:28:00.679
72	LCOGT	*U*	6.80	2.27	0.39	$(9.2 \pm 0.2) \times 10^{31}$	2018-10-12T04:16:29.000	2018-10-12T04:23:17.000	2018-10-12T04:18:45.000
73	LCOGT	*U*	17.52	2.28	2.86	$(5.4 \pm 0.0) \times 10^{32}$	2018-10-12T04:23:17.000	2018-10-12T04:40:48.000	2018-10-12T04:25:34.000

Note.
[a] The units of peak rate are counts per second for XMM-Newton OM, EPIC-pn, and RGS data, angstroms for CHIRON Hα data, and relative counts for all other data.

(This table is available in machine-readable form.)

Appendix C
Neupert Classification Visuals

We provide images similar to Figure 16 for each XMM-Newton flare. Figure 17 shows Neupert and quasi-Neupert flares, while Figure 18 shows non-Neupert flares of both types.

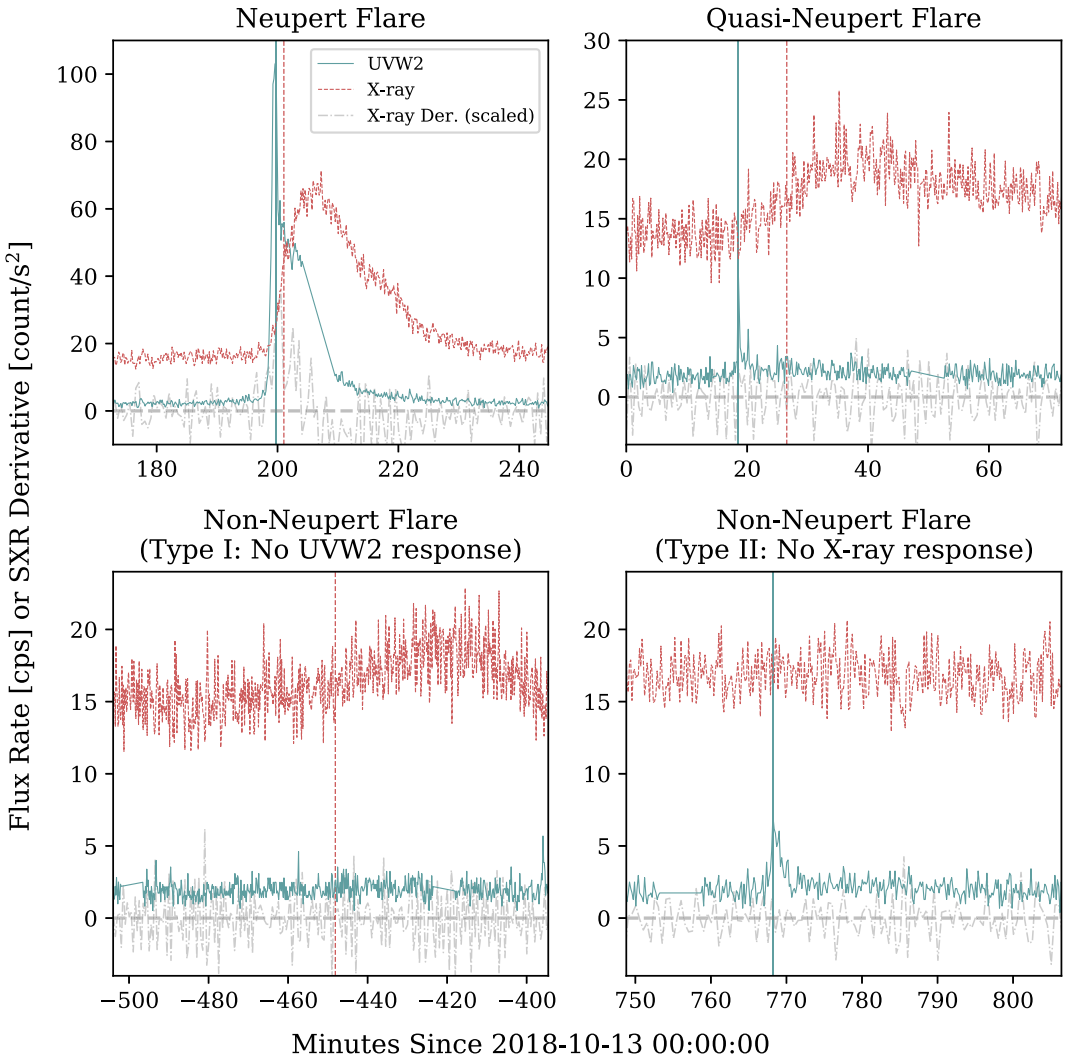

Figure 16. We propose a four-part Neupert classification system based on this XMM-Newton *UVW2* and X-ray data. The dashed vertical lines show the times of the *UVW2* and X-ray derivative peaks. Top: the left panel shows a Neupert flare, where the peak timings of the *UVW2* and X-ray time derivative nearly coincide; the right panel shows a quasi-Neupert flare, where a clear flare is present in both, but these peak timings do not match. Bottom: these lower panels show non-Neupert flares, where either the *UVW2* or X-ray response is missing (Type I and Type II on the left and right, respectively).

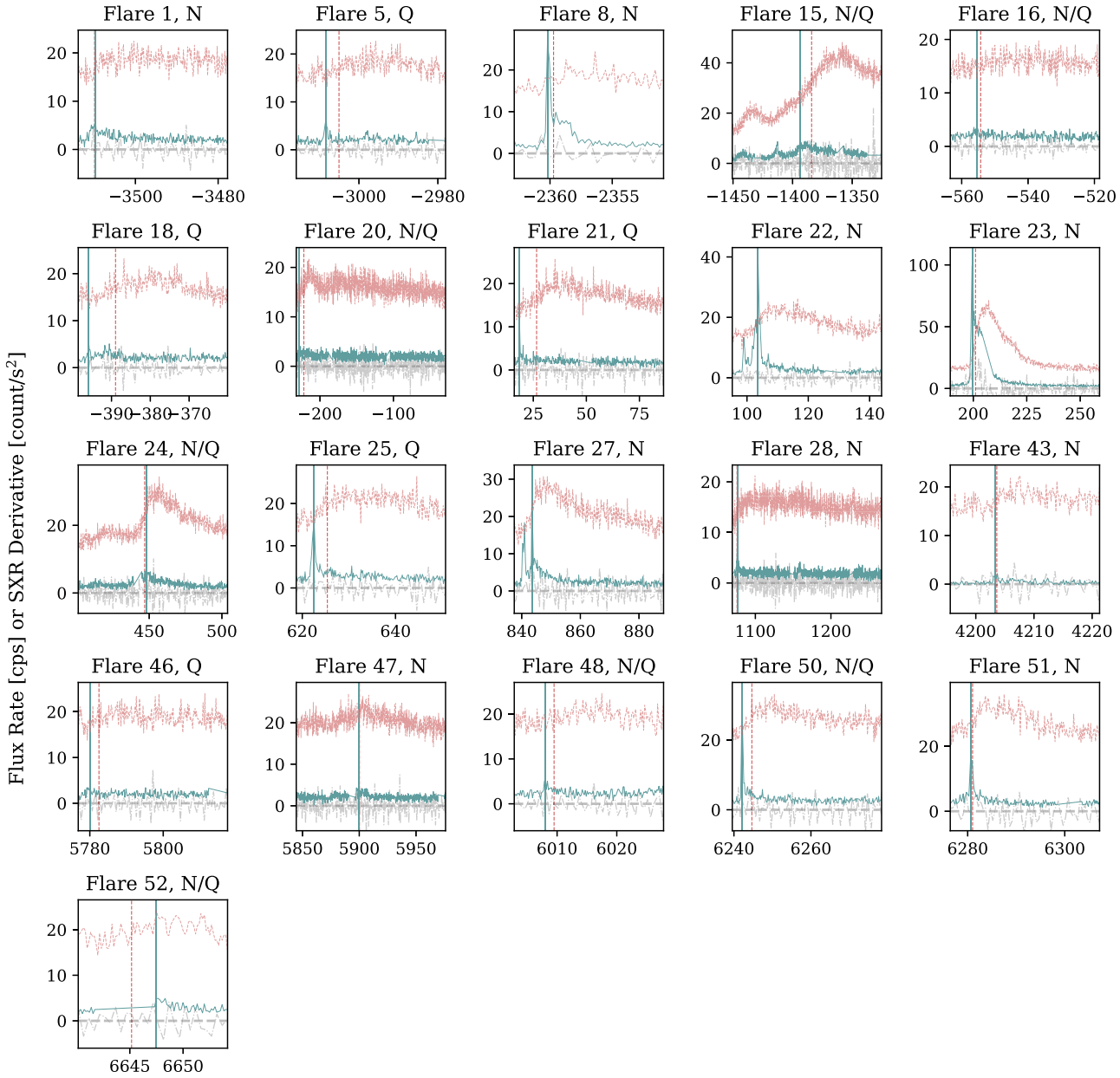

Figure 17. Neupert and quasi-Neupert flares. See Figure 16 for marker descriptions.

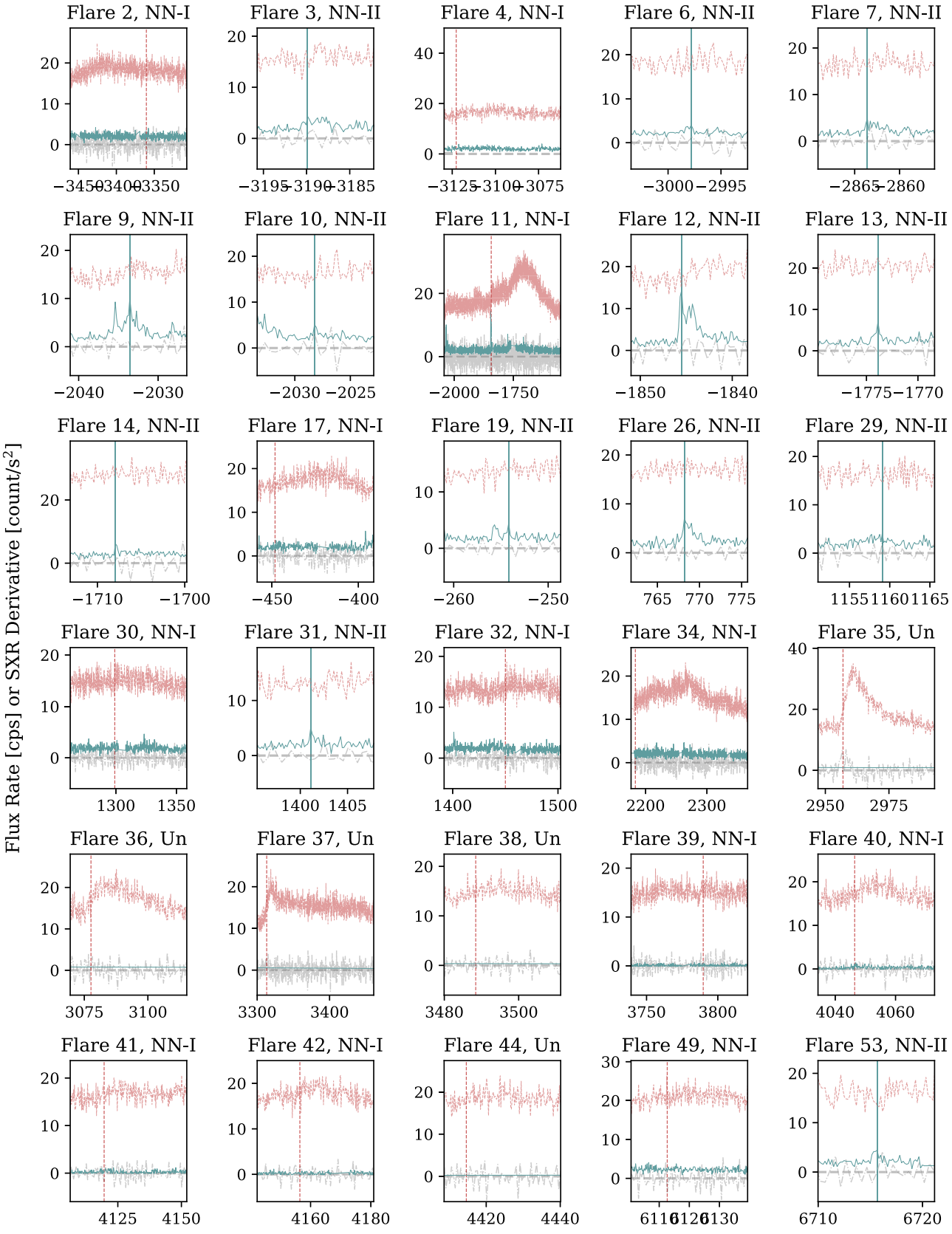

Figure 18. Non-Neupert flares. See Figure 16 for marker descriptions.

Appendix D
Observation Logs

We provide detailed observational logs for each data set, with data logs for XMM OM *UVW2* in Table 7, XMM EPIC-pn X-ray in Table 8, XMM RGS X-ray in Table 9, SMARTS *V* band in Table 10, CHIRON Hα in Table 11, Swift UVOT *W2* in Table 12, Swift XRT X-ray in Table 13, LCOGT *U* band in Table 14, and LCOGT *V* band in Table 15. Note that observation windows are separated by at least 5000 s on nonobservation, unless stated otherwise in the table notes. Total durations here may be longer than in Table 2, as they include times with inclement weather or other issues.

Table 7
Observation Log: XMM-Newton OM *UVW2*

Observation Window	Start (UTC)	End (UTC)	Duration (hr)
1	2018-10-10T13:13:59.760	2018-10-12T01:42:19.177	36.47
2	2018-10-12T13:06:33.808	2018-10-14T01:36:22.232	36.50
3.1	2018-10-14T12:21:18.787	2018-10-14T18:48:06.449	6.45
3.2	2018-10-15T10:35:09.418	2018-10-16T00:04:00.273	13.48
4	2018-10-16T23:39:21.362	2018-10-17T18:17:33.004	18.64

Table 8
Observation Log: XMM-Newton EPIC-pn X-Ray

Observation Window	Start (UTC)	End (UTC)	Duration (hr)
1	2018-10-10T13:13:57.030	2018-10-12T01:54:37.030	36.68
2	2018-10-12T14:06:43.020	2018-10-14T02:33:43.020	36.45
3	2018-10-14T12:21:16.970	2018-10-16T02:25:16.970	38.07
4	2018-10-16T23:39:19.980	2018-10-17T18:29:59.980	18.84

Table 9
Observation Log: XMM-Newton RGS X-Ray

Observation Window	Start (UTC)	End (UTC)	Duration (hr)
1	2018-10-10T13:07:48.868	2018-10-12T01:59:12.093	36.86
2	2018-10-12T13:56:25.491	2018-10-14T02:38:26.807	36.70
3	2018-10-14T12:15:11.942	2018-10-16T02:29:57.499	38.25
4	2018-10-16T23:33:10.575	2018-10-17T18:34:40.232	19.02

Table 10
Observation Log: SMARTS *V* band

Observation Window	Start (UTC)	End (UTC)	Duration (hr)
1	2018-10-10T02:40:42.667	2018-10-10T05:32:51.800	2.87
2	2018-10-12T04:32:30.364	2018-10-12T05:35:17.543	1.05
3	2018-10-12T23:55:49.511	2018-10-13T05:26:07.689	5.51
4	2018-10-14T00:17:42.012	2018-10-14T02:27:56.587	2.17
5	2018-10-14T05:06:33.806	2018-10-14T05:16:02.027	0.16
6	2018-10-14T23:42:09.962	2018-10-15T05:16:13.908	5.57
7	2018-10-15T23:43:58.108	2018-10-16T05:11:48.758	5.46
8	2018-10-16T23:48:09.166	2018-10-17T05:04:31.086	5.27

Table 11
Observation Log: CHIRON Hα

Observation Window	Start (UTC)	End (UTC)	Duration (hr)
1	2018-10-10T01:15:17.900	2018-10-10T03:14:08.600	1.98
2	2018-10-12T04:30:48.900	2018-10-12T04:53:15.000	0.37
3	2018-10-12T23:37:17.900	2018-10-13T04:52:19.200	5.25
4	2018-10-14T00:31:47.800	2018-10-14T02:24:42.300	1.88
5	2018-10-14T23:49:19.900	2018-10-15T04:43:55.100	4.91
6	2018-10-15T23:43:54.700	2018-10-16T04:39:57.400	4.93
7	2018-10-16T23:48:17.000	2018-10-17T04:38:54.200	4.84
8	2018-10-18T00:09:43.300	2018-10-18T04:37:54.900	4.47
9	2018-10-18T23:56:59.300	2018-10-19T04:48:26.100	4.86
10	2018-10-19T23:49:49.800	2018-10-20T04:51:57.500	5.04
11	2018-10-20T23:57:55.900	2018-10-21T04:49:06.400	4.85
12	2018-10-22T00:02:47.800	2018-10-22T04:43:22.200	4.68
13	2018-10-22T23:51:56.100	2018-10-23T04:43:27.300	4.86
14	2018-10-23T23:52:33.500	2018-10-24T04:33:04.800	4.68
15	2018-10-25T00:00:38.300	2018-10-25T04:01:04.000	4.01

Table 12
Observation Log: Swift UVOT *W2* Band

Observation Window	Start (UTC)	End (UTC)	Duration (hr)
1	2018-10-12T03:26:18.000	2018-10-12T03:53:48.000	0.46
2	2018-10-12T04:50:18.000	2018-10-12T05:17:48.000	0.46
3	2018-10-12T06:26:08.000	2018-10-12T06:53:48.000	0.46
4	2018-10-12T08:01:08.000	2018-10-12T08:28:48.000	0.46
5	2018-10-12T09:36:18.000	2018-10-12T10:04:48.000	0.47
6	2018-10-14T03:03:13.000	2018-10-14T03:30:53.000	0.46
7	2018-10-14T04:39:13.000	2018-10-14T05:06:53.000	0.46
8	2018-10-14T06:18:43.000	2018-10-14T06:41:53.000	0.39
9	2018-10-14T07:54:33.000	2018-10-14T08:17:53.000	0.39
10	2018-10-14T09:31:53.000	2018-10-14T09:53:53.000	0.37

Note. A minimum separation of 3000 s was used for this table.

Table 13
Observation Log: Swift XRT X-Ray

Observation Window	Start (UTC)	End (UTC)	Duration (hr)
1	2018-10-12T03:26:20.000	2018-10-12T03:53:50.000	0.46
2	2018-10-12T04:50:25.000	2018-10-12T05:17:50.000	0.46
3	2018-10-12T06:26:25.000	2018-10-12T06:53:50.000	0.46
4	2018-10-12T08:01:15.000	2018-10-12T08:28:50.000	0.46
5	2018-10-12T09:36:40.000	2018-10-12T10:04:50.000	0.47
6	2018-10-14T03:03:16.000	2018-10-14T03:30:51.000	0.46
7	2018-10-14T04:39:26.000	2018-10-14T05:06:51.000	0.46
8	2018-10-14T06:18:56.000	2018-10-14T06:41:51.000	0.38
9	2018-10-14T07:54:41.000	2018-10-14T08:17:51.000	0.39
10	2018-10-14T09:32:16.000	2018-10-14T09:53:51.000	0.36

Note. A minimum separation of 3000 s was used for this table.

Table 14
Observation Log: LCOGT *U* band

Observation Window	Start (UTC)	End (UTC)	Duration (hr)	MPC Code
1	2018-10-10T17:40:11.000	2018-10-10T22:38:52.000	4.98	K91
2	2018-10-12T04:15:42.000	2018-10-12T04:40:46.000	0.42	W85
3	2018-10-12T17:43:00.000	2018-10-12T19:00:04.072	1.28	K91–K93
4	2018-10-12T23:46:56.000	2018-10-13T04:37:19.000	4.84	W85
5	2018-10-13T09:08:14.080	2018-10-13T09:43:55.716	0.59	Q64
6	2018-10-13T12:16:01.221	2018-10-13T13:47:54.839	1.53	Q63
7	2018-10-13T18:15:37.457	2018-10-13T18:55:42.289	0.67	K93
8	2018-10-13T23:47:10.000	2018-10-14T01:24:27.000	1.62	W85
9	2018-10-14T10:45:32.953	2018-10-14T13:03:16.208	2.30	Q63
10	2018-10-14T17:45:40.723	2018-10-14T20:01:27.405	2.26	K93
11	2018-10-14T23:46:50.000	2018-10-15T04:29:29.000	4.71	W85
12	2018-10-15T09:08:59.145	2018-10-15T13:41:52.258	4.55	Q63
13	2018-10-15T17:45:49.000	2018-10-15T20:57:38.729	3.20	K91–K93
14	2018-10-15T23:58:01.000	2018-10-16T04:25:31.000	4.46	W87
15	2018-10-16T09:10:10.842	2018-10-16T10:55:44.674	1.76	Q63–Q64
16	2018-10-16T12:15:32.307	2018-10-16T12:47:22.147	0.53	Q64
17	2018-10-16T17:45:34.514	2018-10-16T22:14:18.924	4.48	K93
18	2018-10-16T23:48:21.000	2018-10-17T04:22:27.000	4.57	W85–W87
19	2018-10-17T11:15:28.508	2018-10-17T12:38:51.859	1.39	Q63
20	2018-10-17T17:46:00.000	2018-10-17T22:12:27.000	4.44	K91
21	2018-10-17T23:49:12.000	2018-10-18T04:17:09.000	4.47	W87
22	2018-10-18T09:11:23.402	2018-10-18T13:28:15.164	4.28	Q63
23	2018-10-18T17:46:56.000	2018-10-18T22:07:41.000	4.35	K91
24	2018-10-18T23:52:55.000	2018-10-19T04:14:10.000	4.35	W87
25	2018-10-19T23:50:49.000	2018-10-20T03:59:50.000	4.15	W87
26	2018-10-20T23:51:35.000	2018-10-21T04:06:07.000	4.24	W87–W85
27	2018-10-21T23:52:26.000	2018-10-22T04:01:17.000	4.15	W87
28	2018-10-22T23:53:09.000	2018-10-23T03:57:44.000	4.08	W85–W87
29	2018-10-23T23:55:30.000	2018-10-24T03:55:35.000	4.00	W87
30	2018-10-24T23:54:48.000	2018-10-25T03:44:32.000	3.83	W85–W87
31	2018-10-26T00:00:48.000	2018-10-26T03:44:05.000	3.72	W87–W85
32	2018-10-26T09:18:27.644	2018-10-26T12:47:54.906	3.49	Q64
33	2018-10-27T00:15:49.000	2018-10-27T03:42:32.000	3.45	W87
34	2018-10-27T09:19:19.920	2018-10-27T09:45:29.010	0.44	Q64
35	2018-10-29T09:21:20.089	2018-10-29T12:35:53.349	3.24	Q64

Note. Observation windows here are determined by MPC code switches. Hyphenated MPC codes represent observations where fast changes between the two occurred. MPC codes: https://lco.global/observatory/sites/mpccodes/.

Table 15
Observation Log: LCOGT *V* band

Observation Window	Start (UTC)	End (UTC)	Duration (hr)	MPC Code
1	2018-10-10T17:40:58.056	2018-10-10T22:29:40.256	4.81	L09
2	2018-10-11T20:15:26.104	2018-10-11T20:43:49.901	0.47	Z17
3	2018-10-12T17:41:26.188	2018-10-12T19:00:30.838	1.32	L09
4	2018-10-12T20:15:14.446	2018-10-12T20:43:43.565	0.47	Z17
5	2018-10-12T23:45:20.277	2018-10-13T04:14:26.415	4.49	W79–W89
6	2018-10-13T09:07:21.487	2018-10-13T10:04:22.760	0.95	Q58
7	2018-10-13T12:45:19.897	2018-10-13T13:48:02.765	1.05	Q58
8	2018-10-13T18:15:11.532	2018-10-13T18:55:26.561	0.67	L09
9	2018-10-13T20:15:18.121	2018-10-13T20:44:09.402	0.48	Z17
10	2018-10-13T23:45:32.916	2018-10-14T02:15:57.115	2.51	W79–W89
11	2018-10-14T10:45:17.467	2018-10-14T11:13:25.150	0.47	Q58
12	2018-10-14T13:15:18.881	2018-10-14T13:43:47.126	0.47	Q58
13	2018-10-14T20:16:27.059	2018-10-14T20:45:35.146	0.49	Z17
14	2018-10-14T23:46:17.290	2018-10-15T04:12:48.908	4.44	W79–W89
15	2018-10-15T04:49:55.571	2018-10-15T05:35:45.104	0.76	T04–T03
16	2018-10-15T09:08:38.998	2018-10-15T13:39:34.949	4.52	Q59–Q58
17	2018-10-15T17:45:30.897	2018-10-15T21:00:09.517	3.24	L09
18	2018-10-15T23:47:04.258	2018-10-16T03:33:45.227	3.78	W79–W89

Table 15
(Continued)

Observation Window	Start (UTC)	End (UTC)	Duration (hr)	MPC Code
19	2018-10-16T09:09:31.799	2018-10-16T12:47:22.397	3.63	Q58–Q59
20	2018-10-16T17:45:21.743	2018-10-16T21:43:55.774	3.98	L09
21	2018-10-16T23:47:49.052	2018-10-17T03:33:25.768	3.76	W79–W89
22	2018-10-17T04:48:24.104	2018-10-17T07:29:54.560	2.69	T04–T03
23	2018-10-17T11:15:17.099	2018-10-17T12:39:13.651	1.40	Q58
24	2018-10-17T17:45:28.091	2018-10-17T21:43:48.517	3.97	L09–Z17
25	2018-10-17T23:48:37.268	2018-10-18T03:46:44.435	3.97	W79–W89
26	2018-10-18T05:15:30.544	2018-10-18T07:26:09.755	2.18	T03
27	2018-10-18T09:11:13.301	2018-10-18T11:43:22.343	2.54	Q59–Q58
28	2018-10-18T12:15:19.076	2018-10-18T13:27:40.087	1.21	Q59
29	2018-10-18T17:46:21.786	2018-10-18T21:43:51.576	3.96	L09
30	2018-10-18T23:49:24.075	2018-10-20T03:33:32.772	27.74	W89–W79
31	2018-10-20T23:51:03.345	2018-10-21T03:44:24.467	3.89	W89
32	2018-10-21T23:52:11.034	2018-10-22T03:47:11.722	3.92	W89–W79
33	2018-10-22T23:52:42.075	2018-10-25T03:33:44.589	51.68	W89–W79
34	2018-10-26T00:00:18.789	2018-10-26T03:29:23.243	3.48	W89–W79
35	2018-10-26T06:00:18.472	2018-10-26T06:53:46.685	0.89	T03
36	2018-10-26T09:18:10.923	2018-10-26T12:56:00.095	3.63	Q58–Q59
37	2018-10-26T17:53:56.020	2018-10-26T21:14:11.359	3.34	L09
38	2018-10-27T00:00:19.949	2018-10-27T03:03:13.800	3.05	W89–W79
39	2018-10-27T09:19:07.294	2018-10-27T10:43:09.378	1.40	Q58
40	2018-10-27T10:45:15.196	2018-10-27T12:54:04.931	2.15	Q59–Q58
41	2018-10-27T18:45:14.346	2018-10-27T21:14:07.773	2.48	L09
42	2018-10-29T09:20:57.973	2018-10-29T12:35:00.467	3.23	Q58–Q59

Note. Observation windows here are determined by MPC code switches. Hyphenated MPC codes represent observations where fast changes between the two occurred. MPC codes: https://lco.global/observatory/sites/mpccodes/.

ORCID iDs

Isaiah I. Tristan https://orcid.org/0000-0001-5974-4758
Yuta Notsu https://orcid.org/0000-0002-0412-0849
Adam F. Kowalski https://orcid.org/0000-0001-7458-1176
Alexander Brown https://orcid.org/0000-0003-2631-3905
John P. Wisniewski https://orcid.org/0000-0001-9209-1808
Rachel A. Osten https://orcid.org/0000-0001-5643-8421
Eliot H. Vrijmoet https://orcid.org/0000-0002-1864-6120
Graeme L. White https://orcid.org/0000-0002-4914-6292
Carol A. Grady https://orcid.org/0000-0001-5440-1879
Todd J. Henry https://orcid.org/0000-0002-9061-2865
Jamie R. Lomax https://orcid.org/0000-0001-8470-0853
Leonardo A. Paredes https://orcid.org/0000-0003-1324-0495

References

Abbett, W. P., & Hawley, S. L. 1999, ApJ, 521, 906
Airapetian, V. S., Barnes, R., Cohen, O., et al. 2020, IJAsB, 19, 136
Albacete Colombo, J. F., Caramazza, M., Flaccomio, E., Micela, G., & Sciortino, S. 2007, A&A, 474, 495
Allred, J. C., Hawley, S. L., Abbett, W. P., & Carlsson, M. 2005, ApJ, 630, 573
Allred, J. C., Hawley, S. L., Abbett, W. P., & Carlsson, M. 2006, ApJ, 644, 484
Alvarado-Gómez, J. D., Cohen, O., Drake, J. J., et al. 2022, ApJ, 928, 147
Anderson, E., & Francis, C. 2012, AstL, 38, 331
Antonucci, E., Gabriel, A. H., Acton, L. W., et al. 1982, SoPh, 78, 107
Antonucci, E., Gabriel, A. H., & Dennis, B. R. 1984, ApJ, 287, 917
Aschwanden, M. J., & Alexander, D. 2001, SoPh, 204, 91
Ashfield, W. H. I., Longcope, D. W., Zhu, C., & Qiu, J. 2022, ApJ, 926, 164
Audard, M., Güdel, M., Drake, J. J., & Kashyap, V. L. 2000, ApJ, 541, 396
Augereau, J.-C., & Beust, H. 2006, A&A, 455, 987
Bessell, M., & Murphy, S. 2012, PASP, 124, 140
Boccaletti, A., Thalmann, C., Lagrange, A.-M., et al. 2015, Natur, 526, 230
Bochanski, J. J., West, A. A., Hawley, S. L., & Covey, K. R. 2007, AJ, 133, 531
Bressan, A., Marigo, P., Girardi, L., et al. 2012, MNRAS, 427, 127
Brown, T. M., Baliber, N., Bianco, F. B., et al. 2013, PASP, 125, 1031
Burrows, D. N., Hill, J. E., Nousek, J. A., et al. 2005, SSRv, 120, 165
Caramazza, M., Flaccomio, E., Micela, G., et al. 2007, A&A, 471, 645
Cargill, P. J., Mariska, J. T., & Antiochos, S. K. 1995, ApJ, 439, 1034
Celis, S. L. 1986, ApJS, 60, 879
Chadney, J. M., Koskinen, T. T., Galand, M., Unruh, Y. C., & Sanz-Forcada, J. 2017, A&A, 608, A75
Chen, C. H., Patten, B. M., Werner, M. W., et al. 2005, ApJ, 634, 1372
Chen, J., Liu, R., Liu, K., et al. 2020, ApJ, 890, 158
Cohen, O., Alvarado-Gómez, J. D., Drake, J. J., et al. 2022, ApJ, 934, 189
Collins, K. A., Kielkopf, J. F., Stassun, K. G., & Hessman, F. V. 2017, AJ, 153, 77
Cully, S. L., Fisher, G. H., Abbott, M. J., & Siegmund, O. H. W. 1994, ApJ, 435, 449
Cutispoto, G., & Leto, G. 1997, A&AS, 121, 369
Cutispoto, G., Messina, S., & Rodonò, M. 2001, A&A, 367, 910
Cutispoto, G., Messina, S., & Rodonò, M. 2003a, A&A, 400, 659
Cutispoto, G., Messina, S., & Rodono, M. 2003b, VizieR Online Data Catalog, J/A+A/400/659
Davenport, J. R. A. 2016, ApJ, 829, 23
Decadal 2020, Pathways to Discovery in Astronomy and Astrophysics for the 2020s (Washington, DC: The National Academies Press)
Dennis, B. R., & Zarro, D. M. 1993, SoPh, 146, 177
Ducati, J. R., Bevilacqua, C. M., Rembold, S. B., & Ribeiro, D. 2001, ApJ, 558, 309
ESA 1997a, VizieR Online Data Catalog, I/239
ESA 1997b, The Hipparcos and Tycho catalogues. Astrometric and photometric star catalogues derived from the ESA Hipparcos Space Astrometry Mission (ESA SP Series) 1200(Noordwijk, Netherlands: ESA Publications Division), 9290923997
Feinstein, A. D., France, K., Youngblood, A., et al. 2022, AJ, 164, 110
Fisher, G. H., Canfield, R. C., & McClymont, A. N. 1985a, ApJ, 289, 425
Fisher, G. H., Canfield, R. C., & McClymont, A. N. 1985b, ApJ, 289, 414
Forbes, T. G., Malherbe, J. M., & Priest, E. R. 1989, SoPh, 120, 285
Fordham, J. L. A., Moorhead, C. F., & Galbraith, R. F. 2000, MNRAS, 312, 83

Fuhrmeister, B., Lalitha, S., Poppenhaeger, K., et al. 2011, A&A, 534, A133
Fuhrmeister, B., Liefke, C., Schmitt, J. H. M. M., & Reiners, A. 2008, A&A, 487, 293
Gaia Collaboration, Brown, A. G. A., Vallenari, A., et al. 2018, A&A, 616, A1
Gaia Collaboration, Prusti, T., de Bruijne, J. H. J., et al. 2016, A&A, 595, A1
Gabriel, C., Denby, M., Fyfe, D. J., et al. 2004, in ASP Conf. Ser. 314, Astronomical Data Analysis Software and Systems (ADASS) XIII, ed. F. Ochsenbein, M. G. Allen, & D. Egret (San Francisco, CA: ASP), 759
Gershberg, R. E. 1972, Ap&SS, 19, 75
Gilbert, E. A., Barclay, T., Quintana, E. V., et al. 2022, AJ, 163, 147
Grady, C. A., Wisniewski, J. P., Schneider, G., et al. 2020, ApJL, 889, L21
Güdel, M., Audard, M., Skinner, S. L., & Horvath, M. I. 2002, ApJL, 580, L73
Güdel, M., Benz, A. O., Schmitt, J. H. M. M., & Skinner, S. L. 1996, ApJ, 471, 1002
Hawley, S. L., Davenport, J. R. A., Kowalski, A. F., et al. 2014, ApJ, 797, 121
Hawley, S. L., Fisher, G. H., Simon, T., et al. 1995, ApJ, 453, 464
Hebb, L., Petro, L., Ford, H. C., et al. 2007, MNRAS, 379, 63
Henry, T. J., Jao, W.-C., Subasavage, J. P., et al. 2006, AJ, 132, 2360
Henry, T. J., Jao, W.-C., Winters, J. G., et al. 2018, AJ, 155, 265
Hilton, E. J. 2011, PhD thesis, Univ. Washington, Seattle
Howard, W. S. 2022, MNRAS: Lett., 512, L60
Ibañez Bustos, R. V., Buccino, A. P., Flores, M., et al. 2019, MNRAS, 483, 1159
Iwakiri, W., Sasaki, R., Negoro, H., et al. 2020, ATel, 13635, 1
Jansen, F., Lumb, D., Altieri, B., et al. 2001, A&A, 365, L1
Kalas, P., Liu, M. C., & Matthews, B. C. 2004, Sci, 303, 1990
Kashyap, V. L., Drake, J. J., Güdel, M., & Audard, M. 2002, ApJ, 580, 1118
Kiraga, M. 2012, AcA, 62, 67
Klein, B., Zicher, N., Kavanagh, R. D., et al. 2022, MNRAS, 512, 5067
Kochukhov, O., & Reiners, A. 2020, ApJ, 902, 43
Kohara, J., Iwakiri, W., Okamoto, Y., et al. 2021, ATel, 15139, 1
Kopparapu, R. K., Ramirez, R., Kasting, J. F., et al. 2013, ApJ, 765, 131
Kowalski, A. F., Allred, J. C., Daw, A., Cauzzi, G., & Carlsson, M. 2017, ApJ, 836, 12
Kowalski, A. F., Hawley, S. L., Carlsson, M., et al. 2015, SoPh, 290, 3487
Kowalski, A. F., Hawley, S. L., Hilton, E. J., et al. 2009, AJ, 138, 633
Kowalski, A. F., Hawley, S. L., Wisniewski, J. P., et al. 2013, ApJS, 207, 15
Kowalski, A. F., Wisniewski, J. P., Hawley, S. L., et al. 2019, ApJ, 871, 167
Krist, J. E., Ardila, D. R., Golimowski, D. A., et al. 2005, AJ, 129, 1008
Lacy, C. H., Moffett, T. J., & Evans, D. S. 1976, ApJS, 30, 85
Lee, T. T., Petrosian, V., & McTiernan, J. M. 1995, ApJ, 448, 915
Leggett, S. K. 1992, ApJS, 82, 351
Leto, G., Pagano, I., Linsky, J. L., Rodonò, M., & Umana, G. 2000, A&A, 359, 1035
Li, P., Emslie, A. G., & Mariska, J. T. 1993, ApJ, 417, 313
Linsky, J. 2019, Host Stars and their Effects on Exoplanet Atmospheres, Vol. 955 (Cham: Springer)
Livshits, M. A., Badalian, O. G., Kosovichev, A. G., & Katsova, M. M. 1981, SoPh, 73, 269
Longcope, D. W. 2014, ApJ, 795, 10
Loyd, R. O. P., France, K., Youngblood, A., et al. 2018, ApJ, 867, 71
MacGregor, A. M., Osten, R. A., & Hughes, A. M. 2020, ApJ, 891, 80
MacGregor, M. A., Weinberger, A. J., Loyd, R. O. P., et al. 2021, ApJL, 911, L25
MacGregor, M. A., Weinberger, A. J., Wilner, D. J., Kowalski, A. F., & Cranmer, S. R. 2018, ApJL, 855, L2
Maehara, H., Notsu, Y., Namekata, K., et al. 2020, PASJ, 73, 44
Mamajek, E. E., & Bell, C. P. M. 2014, MNRAS, 445, 2169
Martioli, E., Hébrard, G., Correia, A. C. M., Laskar, J., & Lecavelier des Etangs, A. 2021, A&A, 649, A177
McClymont, A. N., & Canfield, R. C. 1984, A&A, 136, L1
McTiernan, J. M., Fisher, G. H., & Li, P. 1999, ApJ, 514, 472
Mendoza, G. T., Davenport, J. R. A., Agol, E., Jackman, J. A. G., & Hawley, S. L. 2022, AJ, 164, 17
Mitra, A. P. 1974, Ionospheric Effects of Solar Flares, Vol. 46 (Cham: Springer)
Mitra-Kraev, U., Harra, L. K., Güdel, M., et al. 2005, A&A, 431, 679
Moffett, T. J. 1974, ApJS, 29, 1
Mukai, K. 1993, Legacy, 3, 21
Namekata, K., Maehara, H., Sasaki, R., et al. 2020, PASJ, 72, 68
Namekata, K., Sakaue, T., Watanabe, K., et al. 2017, ApJ, 851, 91
Nasa High Energy Astrophysics Science Archive Research Center (Heasarc) 2014, HEAsoft: Unified Release of FTOOLS and XANADU, NASA, Astrophysics Source Code Library, ascl:1408.004
Neupert, W. M. 1968, ApJL, 153, L59
Nishimoto, S., Watanabe, K., Kawai, T., Imada, S., & Kawate, T. 2021, EP&S, 73, 79
Notsu, S., van Dishoeck, E. F., Walsh, C., Bosman, A. D., & Nomura, H. 2021, A&A, 650, A180
Notsu, Y., Maehara, H., Honda, S., et al. 2019, ApJ, 876, 58
Osten, R., Livio, M., Lubow, S., et al. 2013, ApJL, 765, L44
Osten, R. A., Drake, S., Tueller, J., et al. 2007, ApJ, 654, 1052
Osten, R. A., Hawley, S. L., Allred, J., et al. 2006, ApJ, 647, 1349
Osten, R. A., Hawley, S. L., Allred, J. C., Johns-Krull, C. M., & Roark, C. 2005, ApJ, 621, 398
Osten, R. A., Kowalski, A., Drake, S. A., et al. 2016, ApJ, 832, 174
Osten, R. A., Kowalski, A., Sahu, K., & Hawley, S. L. 2012, ApJ, 754, 4
Osten, R. A., & Wolk, S. J. 2015, ApJ, 809, 79
Page, M. J., Kuin, N. P. M., Breeveld, A. A., et al. 2013, MNRAS, 436, 1684
Pallavicini, R., Tagliaferri, G., & Stella, L. 1990, A&A, 228, 403
Paudel, R. R., Barclay, T., Schlieder, J. E., et al. 2021, ApJ, 922, 31
Perryman, M. A. C., Lindegren, L., Kovalevsky, J., et al. 1997, A&A, 323, L49
Petschek, H. E. 1964, AAS NASA Symposium on the Physics of Solar Flares Vol. 50 *(Goddard Space Flight Center, Greenbelt, MD, 28 October, 1963)* ed. W. N. Hess, (Washington, DC: National Aeronautics and Space Administration, Science and Technical Information Divison), 425
Pettersen, B. R., Coleman, L. A., & Evans, D. S. 1984, ApJS, 54, 375
Pillitteri, I., Argiroffi, C., Maggio, A., et al. 2022, A&A, 666, A198
Plavchan, P., Barclay, T., Gagné, J., et al. 2020, Natur, 582, 497
Pojmanski, G., & Maciejewski, G. 2005, AcA, 55, 97
Qian, L., Burns, A. G., Chamberlin, P. C., & Solomon, S. C. 2011, JGRA, 116, A10309
Qiu, J., Sturrock, Z., Longcope, D. W., Klimchuk, J. A., & Liu, W.-J. 2013, ApJ, 774, 14
Redfield, S., Linsky, J. L., Ake, T. B., et al. 2002, ApJ, 581, 626
Reid, I. N., Cruz, K. L., Allen, P., et al. 2004, AJ, 128, 463
Robinson, R. D., Carpenter, K. G., Woodgate, B. E., & Maran, S. P. 1993, ApJ, 414, 872
Robinson, R. D., Linsky, J. L., Woodgate, B. E., & Timothy, J. G. 2001, ApJ, 554, 368
Rodono, M., Cutispoto, G., Pazzani, V., et al. 1986, A&A, 165, 135
Roming, P. W. A., Kennedy, T. E., Mason, K. O., et al. 2005, SSRv, 120, 95
Schneider, G., Grady, C. A., Hines, D. C., et al. 2014, AJ, 148, 59
Shibata, K., & Magara, T. 2011, LRSP, 8, 6
Shibata, K., & Takasao, S. 2016, in Astrophysics and Space Science Library, Magnetic Reconnection: Concepts and Applications, ed. W. Gonzalez & E. Parker, 427 (Berlin: Springer), 373
Sirianni, M., Jee, M. J., Benítez, N., et al. 2005, PASP, 117, 1049
Smith, D. S., Scalo, J., & Wheeler, J. C. 2004, OLEB, 34, 513
Stelzer, B., Caramazza, M., Raetz, S., Argiroffi, C., & Coffaro, M. 2022, A&A, 667, L9
Stelzer, B., Flaccomio, E., Briggs, K., et al. 2007, A&A, 468, 463
Strüder, L., Briel, U., Dennerl, K., et al. 2001, A&A, 365, L18
Subasavage, J. P., Bailyn, C. D., Smith, R. C., et al. 2010, Proc. SPIE, 7737, 77371C
Talavera, A. 2011, XMM-Newton Optical and UV monitor (OM) Calibration Status, ESA, (https://xmmweb.esac.esa.int/docs/documents/CAL-TN-0019.pdf)
The, P. S., Steenman, H. C., & Alcaino, G. 1984, A&A, 132, 385
Tokovinin, A., Fischer, D. A., Bonati, M., et al. 2013, PASP, 125, 1336
Torres, C. A. O., & Ferraz Mello, S. 1973, A&A, 27, 231
Veronig, A., Vršnak, B., Dennis, B. R., et al. 2002, A&A, 392, 699
Veronig, A. M., Brown, J. C., Dennis, B. R., et al. 2005, ApJ, 621, 482
Virtanen, P., Gommers, R., Oliphant, T. E., et al. 2020, NatMe, 17, 261
Vrijmoet, E. H., Henry, T. J., Jao, W.-C., & Dieterich, S. B. 2020, AJ, 160, 215
Walker, A. R. 1981, MNRAS, 195, 1029
Warmuth, A., Holman, G. D., Dennis, B. R., et al. 2009, ApJ, 699, 917
Warmuth, A., & Mann, G. 2016a, A&A, 588, A115
Warmuth, A., & Mann, G. 2016b, A&A, 588, A116
Warren, H. P. 2006, ApJ, 637, 522
West, A. A., Hawley, S. L., Bochanski, J. J., et al. 2008, AJ, 135, 785
White, R., Schaefer, G., Boyajian, T., et al. 2019, AAS Meeting Abstracts, 233, 259.41
Willmer, C. N. A. 2018, ApJS, 236, 47
Winters, J. G., Henry, T. J., Lurie, J. C., et al. 2015, AJ, 149, 5
Wisniewski, J. P., Kowalski, A. F., Davenport, J. R. A., et al. 2019, ApJL, 883, L8
Wood, B. E., Redfield, S., Linsky, J. L., Muller, H.-R., & Zank, G. P. 2005, ApJS, 159, 118
Woods, T. N., Hock, R., Eparvier, F., et al. 2011, ApJ, 739, 59
Yokoyama, T., & Shibata, K. 1998, ApJ, 494, L113
Yokoyama, T., & Shibata, K. 2001, ApJ, 549, 1160